平成２３年度研究成果発表リスト

1. 論文発表

■先端表面敏感計測技術の開発と先進材料応用

国際誌

[1] M. Xu, D. Fujita, K. Sagisaka, E. Watanabe, N. Hanagata, "Production of extended single-layer graphene", ACS NANO, Vol.5, Number 2, Page 1522 ～ 1528,(2011)

[2] K. Onishi,F. Daisuke, "Novel Tip Shape Reconstruction Method for Restoration of AFM Topography Images Using Nano-structures with Given Shapes", ANALYTICAL SCIENCES, Vol.27, Number 2, Page 157 ～ 161,(2011)

[3] N. Ishida, T. Iwasaki,D. Fujita, "Observation of photo-decomposition process of spherical organic polymers on rutile TiO_2(110) surfaces", NANOTECHNOLOGY, Vol.22, Number 15, Page 155705-1 ～ 155705-3,(2011)

[4] I, Katayama, S. Koga,K. Shudo, J. Takeda, T. Shimada, A. Kubo, S. Hishita, D. Fujita, M. Kitajima, "Ultrafast Dynamics of Surface-enhanced Raman Scattering due to Au Nanostructures", NANO LETTERS, Vol.11, Number 7, Page 2648 ～ 2654 (2011)

[5] M. Xu, D. Fujita, H. Chen, N. Hanagata, "Formation of monolayer and few-layer hexagonal boron nitride nanosheets via surface segregation", NANOSCALE, Vol.3, Number 7, Page 2854 ～ 2858,(2011)

[6] D. Fujita, "Nanoscale synthesis and characterization of graphene-based objects", SCIENCE AND TECHNOLOGY OF ADVANCED MATERIALS, Vol.12, Page 044611-1 ～ 044611-10,(2011)

[7] H. Guo, D. Fujita, "In situ Observation of Surface Reconstruction of Si(001) with Stress/Strain Field Scanning Probe Microscopy", JAPANESE JOURNAL OF APPLIED PHYSICS, Vol.50, Number 8, Page 08LB04-1 ～ 08LB04-4,(2011)

[8] GUOHongxuan/GUO Hongxuan, 藤田大介 /FUJITA Daisuke, "Developments of scanning probe microscopy with stress/strain fields", REVIEW OF SCIENTIFIC INSTRUMENTS, Vol.82, Number 12, Page 123706-1 ～ 123706-6,(2011)

[9] KURAHASHI Mitsunori, AndrewPratt, YAMAUCHI Yasushi, “Spin polarization of the Si(111)-7x7 surface: A study with a spin-polarized metastable helium atom beam”, Surface Science Vol.605 Page 612 (2011).

[10] Mikihiko Nishitani,Yukihiro Morita, Masaharu Terauchi,Yasuhiro Yamauchi, Kyohei Yoshino, Masahiro Sakai, Yusuke Takata, Yasushi Yamauchi, “Surface characterization of MgO:Al,N films with meta-stable de-excitation spectroscopy and x-ray photoelectron spectroscopy”, Journal of the SID Vol. 19 Page 8 (2011).

[11] A. Pratt, M. Kurahashi, Y. Yamauchi, “Spin-polarized metastable He study of surface magnetic order in Ho thin films”, JOURNAL OF APPLIED PHYSICS Vol. 109 Page 07C111 (2011).

[12] T. Suzuki, H. Kuwahara, Y. Yamauchi, “Effect of ion beam irradiation on magnetism of Fe(100) outermost surfaces studied by spin-polarized ion scattering spectroscopy”, Surface Science Vol.605 Page 1197 (2011).

[13] X. Sun, M. Kurahashi, A. Pratt, Y. Yamauchi, “First-principles study of atomic hydrogen adsorption on Fe3O4(100)”, Surface Science Vol. 605 Page 1067 (2011).

[14] X. Sun, Y. Yamauchi, “The geometric and electronic structure of Xe-adsorbed Fe(0 0 1) surface by first-principles calculations”, Chemical Physics Letters Vol. 512 Page 99 (2011).

[15] A Pratt, M Kurahashi, X Sun, Y Yamauchi, “Adsorbate-induced spin-polarization enhancement of Fe3O4(0 0 1)”, J. Phys. D: Appl. Phys. Vol. 44 Page 0640101(2011).

[16] T. Suzuki, Y. Yamauchi, S. Hishita, “Spin-Dependent Low-Energy 4He+ Ion Scattering from Nonmagnetic Surfaces”, PRL Vol.107 Page 176101 (2011).

[17] X. Sun, Y. Yamauchi, “First-principles calculations of Xe-adsorbed Pd(111) and Cu(111) surfaces with an empirical correction of van der Waals interactions”, JOURNAL OF APPLIED PHYSICS Vol. 110 Page 103701 (2011).

[18] K. Yoshino, Y. Morita, T. Nagatomi, M. Terauchi, T. Tsujita, T. Nakayama, Y. Yamauchi, M. Nishitani, M. Kitagawa, Y. Yamauchi, Y. Takai1, “Investigation of Measurement Conditions of Metastable De-excitation Spectroscopy of MgO Thin Films Used for Plasma Display Panels”, Journal of Surface Analysis Vol.18 Page 13 (2011).

[19] A. Pratt, L. Dunne, X. Sun, M. Kurahashi, and Y. Yamauchi, “Energy-level alignment at the Alq3/Fe3O4(001) interface”, Appl. Phys. Vol. 111 Page 07C114 (2012).

[20] Mitsunori Kurahashi, Yasushi Yamauchi, “Huge steric effects in surface oxidation of Si(100)”, Huge steric effects in surface oxidation of Si(100)” PHYSICAL REVIEW B Vol. 85 Page 161302(R) (2012).

[21] A. Pratt, M. Kurahashi, X. Sun, D. Gilks, Y. Yamauchi1, “Direct observation of a positive spin polarization at the (111) surface of magnetite”, PHYSICAL REVIEW B 85, 180409(R) (2012).

[22] S Torbrügge, O Custance, S Morita and M Reichling, “Manipulation of individual water molecules on CeO2(111)”, J. Phys.: Condens. Matter 24, 084010 (10pp), (2012)

[23] Keiko ONISHI, Tamaki IWASAKI and Daisuke FUJITA, “SPM DATA CONVERSION PROGRAM BASED ON ISO STANDARD DATA TRANSFER FORMAT” The 3rd International Symposium on Stadardization of SPM , NIMS, (2012/03/01 - 2012/03/02)

[24] M. Ishii, B. Towlson, N. Poolton, S. Harako, X. Zhao, S. Komuro, and B. Hamilton, “Effects of oxidization and deoxidization on charge-propagation dynamics in rare-earth-doped titanium dioxide with room-temperature luminescence”, Journal of Applied Physics, Vol. 111, 053514, (2012).

[25] M. Ishii, S. Harako, X. Zhao, S. Komuro, and B. Hamilton, “Observation of charge transfer process for optical emission of rare-earth dopant using electric probing technique”, Journal of Luminescence, , doi:10.1016/j.lumin.2011.12.041 (2011).

[26] M. Ishii, S. Harako, X. Zhao, S. Komuro, and B. Hamilton, “Charge propagation dynamics at trapping centers that induce the luminescence of rare-earth dopants in wide-gap materials”, Applied Physics Letters, Vol. 99, 101909 (2011).

■先端表層領域計測技術の開発と先進材料応用

国際誌

[27] K. Ishioka, A.K. Basak, H. Petek, Allowed and Forbidden Raman Scattering Mechanisms for Detection of Coherent LO Phonon and Plasmon-Coupled Modes in GaAs, Phys. Rev. B 84, 235202 (2011).

[28] T.Nagatomi, H.Nakamura, Y.Takai, T.Ogiwara, T.Kimura, S.Tanuma, “Effects of Carbon Contaminations on Electron-Induced Damage of SiO2 Film Surface at Different Electron Primary Energies”, JOURNAL OF SURFACE ANALYSIS, Vol.18, No.1(2011).

[29] T. Nagatomi, H. Nakamura, Y. Takai, S.Tanuma, “Approach to Quantitative Evaluation of Electron-Induced Degradation of SiO2 Film Surface with Different Amounts of Carbon

Contaminations”, e-JOURNAL OF SURFACE SCIENCE AND NANOTECHNOLOGY, Vol.9, No. 2011(2011)

[30] H.Shinotsuka, S.Tanuma, C, J. Powell, D.R. Penn, “Calculations of electron stopping powers for 41 elemental solids over the 50 eV to 30 keV range with the full Penn algorithm”, NUCLEAR INSTRUMENTS & METHODS IN PHYSICS RESEARCH SECTION B-BEAM INTERACTIONS WITH MATERIALS AND ATOMS,Vol.270（2011).

[31] YANG Xi, XU Mingsheng, QIU Weiming, CHEN XiaoqiangDENG Meng, ZHANG Jinglin, H.Iwai, E.Watanabe, CHEN Hongzheng, “Graphene uniformly decorated with gold nanodots: in situ synthesis, enhanced dispersibility and applications”, JOURNAL OF MATERIALS CHEMISTRY, Vol.21, No.22(2011).

[32] QIU Weiming, XU Mingsheng, YANG Xi, CHEN Fei, NAN Yaxiong, ZHANG Jinglin, H.Iwai, CHEN Hongzheng, “Biomolecule-assisted hydrothermal synthesis of In2S3 porous films and enhanced photocatalytic properties”, JOURNAL OF MATERIALS CHEMISTRY, Vol.21, No.35(2011)

[33] M.Kazama, J.Adachi, H.Shinotsuka, M.Yamazaki, Y.Ohori, A.Yagishita, T.Fujikawa, “Theoretical study of X-ray photoelectron diffraction for fixed-in-space CO molecules”, CHEMICAL PHYSICS, Vol.373,No.3(2011).

[34] T.Fujii, H.Oohashi, T.Tachio, Y.Ito, VLAICUAUREL MIHAI, S.Fukushima, “Speculations on anomalous chemical states of Ti ions in FeTiO3 observed by high-resolution X-ray K-beta emission spectra”, JOURNAL OF ELECTRON SPECTROSCOPY AND RELATED PHENOMENA, Vol.184,No.1(2011).

[35] K.Yoshii, Ignace Jarrigei, D.Matsumura, T.Nishihata, C. Suzuki, Y.Ito, T.Mukoyama, T.Tachio, H.Shinotsuka, S.Fukushima,” Resonant Inelastic X-ray Scattering at Ba-L3 Edge in BaTiO3”, JAPANESE JOURNAL OF APPLIED PHYSICS, Vol.50(2011).

[36] Iva Matolinova, R.Fiala, I.Khalakhan, Mykhailo VOROKHTA, Z. Sofer, H.Yoshikawa, K.Kobayashi, Matolín, V, ” Synchrotron radiation photoelectron spectroscopy study of metal-oxide thin film catalysis: Pt-CeO2 coated CNTs”, APPLIED SURFACE SCIENCE,Vol258, No.6(2011).

[37] H. Niwa, M. Kobayashi, K. Horiba, Y. Harada, M. Oshima, K. Terakura, T. Ikeda, Y. Koshigoe, J. Ozaki, S. Miyata, S. Ueda, Y. Yamashita, H. Yoshikawa , K. Kobayashi, “X-ray photoemission spectroscopy analysis of N-containing carbon-based cathode catalysts for polymer electrolyte fuel cells”, Journal of Power Sources, 196, 1006-1011 (2011).

[38] H. YAMAOKA , A. KOTANI , Y. KUBOZONO, A.M. VLAICU, H. OOHASHI, T. TOCHIO, Y. ITO, and H. YOSHIKAWA, "Charge-Transfer Satellite in Ce@C82 Probed by Resonant X-ray Emission Spectroscopy", J. Phys. Soc. Jpn., 80, 14702-1-5 (2011)

[39] K. Fugan, T. Mori, D. R. Ou, A. Suzuki, H. Yoshikawa, T. Masuda, K. Uosaki, Y. Yamashita, S. Ueda, K. Kobayashi, N. Okazaki, I. Matolinova, V. Matolin, "Activity of oxygen reduction reaction on small amount of amorphous CeOx promoted Pt cathode for fuel cell application", Electrochimica Acta, 56, 3874-3883 (2011)

[40] O. Bierwagen, J.S. Speck, T. Nagata, T. Chikyow, Y. Yamashita, H. Yoshikawa, and K. Kobayashi, "Depletion of the In2O3 (001) and (111) surface electron accumulation by an oxygen plasma surface treatment", Appl Phys. Lett., 98, 172101-1-3 (2011)

[41] T. Nagata, O. Bierwagen, M. E. White, M. Y. Tsai, Y. Yamashita, H. Yoshikawa, N. Ohashi, K. Kobayashi, T. Chikyow, and J. S. Speck, "XPS study of Sb-/In-doping and surface pinning effects on the Fermi level in SnO2 thin films", Appl Phys. Lett. 98, 232107-1-3 (2011).

[42] K. Nishio, M. Matvejeff, R. Takahashi, M. Lippmaa, M. Sumiya, H. Yoshikawa, K. Kobayashi and Y. Yamashita, "Delta-doped epitaxial La:SrTiO3 field-effect transistor", Appl Phys. Lett. 98, 242113-1-3 (2011)

[43] Y. Adachi, N. Ohashi, T. Ohgaki, T. Ohnishi, I. Sakaguchi, S. Ueda, H. Yoshikawa, K. Kobayashi, J. R. Williams, T. Ogino, H. Haneda, "Polarity of heavily doped ZnO films grown on sapphire and SiO2 glass substrates by pulsed laser deposition", Thin Solid Films 519, 5875-5881 (2011).

[44] M. Kobayashi, H. Niwa, Y. Harada , K. Horiba, M. Oshima, H. Ofuchi, K. Terakura, T. Ikeda, Y. Koshigoe, J. Ozaki, S. Miyata,S. Ueda, Y. Yamashita, H. Yoshikawa, K. Kobayashi, "Role of residual transition-metal atoms in oxygen reduction reaction in cobalt phthalocyanine-based carbon cathode catalysts for polymer electrolyte fuel cell", Journal of Power Sources, 196, 8346-8351 (2011)

[45] R. Hayakawa, M. Yoshida, K. Ide, Y. Yamashita, H. Yoshikawa, K. Kobayashi, S. Kunugi, T. Uehara, and N. Fujimura, "Structural analysis and electrical properties of pure Ge3N4 dielectric layers formed by an atmospheric-pressure nitrogen plasma", Journal of Applied Physics, 110, 064103-1-5 (2011)

[46] H. Tanaka, H. Yoshikawa, C. Tsuruta, Y. Matsui, and S. Kishida, "Enhancement of Intragrain Critical Current Density in Bi-Based Superconductor by Substitutional Structural Defects", IEEE TRANSACTIONS ON APPLIED SUPERCONDUCTIVITY, 21, 3203-3205 (2011).

国内誌

[47] 荻原俊弥， 永富隆清， K.J.Kim, 田沼繁夫 ,“半球型電子分光器を搭載したオージェ電子分光装置のジオメトリー特性に基づいた傾斜ホルダーを利用した高感度， 高深さ分解能オージェ深さ方向分析”, J. Surf. Anal., 18 巻 , 3 号 ,174 - 181 (2011).

[48] 荻原俊弥， 永富隆清， K. J. Kim, 田沼繁夫 ,“傾斜試料ホルダーを用いた極低角度電子・イオン入射による超高深さ分解能オージェ深さ方向分析”, 表面科学 , 32 巻 ,10 号 , 664 - 669(2011).

[49] 山下良之 , 長田貴弘 , 吉川英樹 , 知京豊祐 , 小林啓介 ,“デバイス動作下硬 X 線光電子分光法による最先端材料の物性解明”, 表面科学 , 32, 320-324 (2011).

著書

[50] 岩井秀夫 , 荻原俊弥 , 福島整 , 田中彰博 , 田沼繁夫 ,“用語辞典 / 分担執筆”, 分析化学用語辞典 (2011).

■超先端電子顕微鏡技術の開発と先進材料応用

国際誌

[51] Masaki Saruyama, Yeong-Gi So, Koji Kimoto, Seiji Taguchi, Yoshihiko Kanemitsu, and Toshiharu Teranishi, "Spontaneous Formation of Wurzite-CdS/Zinc Blende-CdTe Heterodimers through a Partial Anion Exchange Reaction", J. Am. Chem. Soc., 133 (44), 17598–17601(2011).

[52] Koji Kimoto and Kazuo Ishizuka, "Spatially resolved diffractometry with atomic-column resolution", Ultramicroscopy, 111, 1111-1116 (2011).

[53] Megumi Ohwada, Koji Kimoto, Kazutomo Suenaga, Yuta Sato, Yasuo Ebina and Takayoshi Sasaki, "Synthesis and Atomic Characterization of a Ti2O3 Nanosheet", Journal of Physical Chemistry Letters, 2 (14), 1820-1823 (2011).

[54] Masahiro Nagao, Takuro Nagai, Toru Hara and Koji Kimoto, "Effect of dimension on charge order domain in Ruddlesden-Popper manganites", Physica B: Condensed Matter, 406, 3192-3195 (2011).

[55] X. Z. Yu, N. Kanazawa, Y. Onose, K. Kimoto,W. Z. Zhang, S. Ishiwata, Y. Matsui and Y. Tokura, "Near room-temperature formation of a skyrmion crystal in thin-films of the helimagnet FeGe", Nature Materials, 10,106-109 (2011).

[56] T.Hara, K.Tsuchiya, K.Tsuzaki, X.Man, T.Asahata and A.Uemoto, “Application of orthogonally arranged FIB–SEM for precise microstructure analysis of materials”, Journal of Alloys and Compounds, doi:10.1016/j.jallcom.2012.02.019, In Press, Available online 16 February 2012.

[57] E.Okunishi, T.Kawai, M.Mitsuhara, S.Farjami, M.Itakura, T.Hara and M.Nishida, “HAADF-STEM studies of athermal and isothermal omega-phases in beta-Zr alloy”, Journal of Alloys and Compounds, doi: 10.1016/j.jallcom.2011.12.115. In press available online.(2012)

[58] K.Sakai, K.Mitsuda, N.Y.Yamasaki, Y.Takei, R.Yamamoto, T.Hara, K.Maehata, N.Iyomoto, K.Tanaka, ” TEM-EDS with Breakthroughs in 3D Wiring and High-Speed Processing”, J. Low Temp. Phys. 167, 759-764,(2012)

[59] K.Maehata, N.Iyomoto, T.Yasumune, M.Maeda, S.Matsumura, T.Hara, K.Mitsuda, N.Yamasaki, K.Tanaka, “Development of a TES Microcalorimeter with a Mushroom Shaped Absorber Deposited on an Insulating Layer in an Overhang Region”, J. Low Temp. Phys. 167, 226-231,(2012)

[60] M.Matsuda, K.Kuramoto, Y.Morizono, S.Tsurekawa, E.Okunishi, T.Hara and M.Nishida. “Transmission electron microscopy of antiphase boundary-like structure of B19’ martensite in Ti-Ni shape memory alloy”, ACTA MATERIALIA,59,133-140,(2011).

[61] L.Zhang, T.Ohmura, K.Sekido, K.Nakajima, T.Hara and K.Tsuzaki, “Direct observation of plastic deformation in iron-3% silicon single crystal by in situ nanoindentation in transmission electron microscopy”, SCRIPTA MATERIALIA, 64, 9, 919-922, (2011)

[62] S.Stehlik, J.Orava, T.Kohoutek, T.Wagner, M.Frumar, V.Zima, T.Hara, Y.Matsui, K.Ueda, M.Pumera, “Carbon nanotube chalcogenide glass composite”, JOURNAL OF SOLID STATE CHEMISTRY, 183, 1, 144-149, (2010)

[63] K.Sekido, T.Ohmura, L.Zhang, T.Hara, K.Tsuzaki, “The effect of interstitial carbon on the initiation of plastic deformation of steels”, MATERIALS SCIENCE AND ENGINEERING A-STRUCTURAL MATERIALS PROPERTIES MICROSTRUCTURE AND PROCESSING, 530, 396-401, (2011)

[64] T.Hayashi, T.Hara and E.Abe, Complex oxide layer at a Nickel/Steel interface bonded under a moderate vacuum condition”, ISIJ INTERNATIONAL, 51-11, 1859-1863, (2011).

[65] S. Chen, A. Osaka, T. Ikoma, H. Morita, J. Li, M. Takeguchi and N. Hanagata, “Fabrication, microstructure, and BMP-2 delivery of novel biodegradable and biocompatible silicate-collagen hybrid fibril sheets”, Journal of Materials Chemistry 21 (2011) 10942-10948.

[66] S. Kim, Y. Oshima, H. Sawada, T. Kaneyama, Y. Kondo, M. Takeguchi, Y. Nakayama, Y. Tanishiro, K. Takayanagi, “Quantitative annular dark-field STEM images of a silicon crystal using a large-angle convergent electron probe with a 300-kV cold field-emission gun”, Journal of Electron Microscopy 60 (2011) 109-116.

[67] JJ. Xing, H. Gu, YU. Heo, and M. Takeguchi, “Initial transient structure and chemistry of intergranular glassy films in ferric-oxide doped strontium titanate ceramics”, Journal of Materials Science 46 (2011) 4361-4367.

[68] A. Hashimoto, K. Mitsuishi, M. Shimojo, YF. Zhu and M. Takeguchi, “Experimental examination of the characteristics of bright-field scanning confocal electron microscopy images”, Journal of Electron Microscopy 60 (2011) 227-234.

[69] P. Wang, G. Behan, AI. Kirkland, PD. Nellist, EC. Cosgriff, AJ. D'Alfonso, J. Adrian, AJ. Morgan, LJ. Allen, A. Hashimoto, M. Takeguchi, K. Mitsuishi, M. Shimojo, “Bright-field

scanning confocal electron microscopy using a double aberration-corrected transmission electron microscope”, Ultramicroscopy 111 (2011) 877-886.

[70] M. Okuda N. Ogawa, M. Takeguchi, A. Hashimoto, M. Tagaya, S. Chen, N. Hanagata, T. Ikoma, “Minerals and Aligned Collagen Fibrils in Tilapia Fish Scales: Structural Analysis Using Dark-Field and Energy-Filtered Transmission Electron Microscopy and Electron Tomography”, Microscopy and Microanalysis 17 (2011) 788-798.

[71] YU, Heo, M. Takeguchi, JJ. Xing and Y. Nakayama, “Oxidation and reduction behavior of Ni and NiO layers sputter deposited onto yttrium-stabilized zirconia single crystals”, Thin Solid Films 520 (2011) 138-143.

[72] M. Tagaya, T. Ikoma, M. Takeguchi, N. Hanagata and J. Tanaka,” Interfacial Serum Protein Effect on Biological Apatite Growth”, Journal of Physical Chemistry C 115 (2012) 22523-22533.

[73] S. Kang, M. Takeda, M. Takeguchi, DS. Bae, “TEM Study and Magnetic Measurements of Precipitates Formed in Cu-Fe-Ni Alloys”, Journal of Nanoscience and Nanotechnology 11 (2012) 10800-10803.

[74] K. Mitsuishi, A. Hashimoto, M. Takeguchi, M. Shimojo and K. Ishizuka, “Imaging properties of bright-field and annular-dark-field scanning confocal electron microscopy: II. Point spread function analysis”, Ultramicroscopy 112 (2012) 53-60.

[75] T. Noriki, S. Kang, M. Takeguchi and M. Takeda, “Nano-Scale Precipitates Formed in Cu-Co Based Alloys and Their Magnetic Properties”, Journal of Nanoscience and Nanotechnology 12 (2012) 1688-1691.

[76] S. Kang, M. Takeda, M. Takeguchi, Z. Hiroi, G. W. Kim, DS. Bae, CG. Lee and BH. Koo, “Study on the Microstructures and the Magnetic Properties of Precipitates in a Cu-75-Fe-5-Ni-20 Alloy”, Journal of Nanoscience and Nanotechnology 12 (2012) 1337-1340.

[77] S. Bysakh, K. Mitsuishi, M. Song, K. Furuya, K. Chattopadhyay, “Formation of amorphous xenon nanoclusters and microstructure evolution in pulsed laser deposited Ti62.5Si37.5 thin films during Xe ion irradiation”,Journal of Materials Research, 26 (2011) 62-69.

[78] I.Sychugov, J.Valenta,K. Mitsuish, M. Fujii, J. Linnros, “Photoluminescence Measurements of Zero-Phonon Optical Transitions in Silicon Nanocrystals”, ,Phy Rev. B 84, (2011) 125326-1-125326-5,

[79] C. Wen, T. Nonomura, Y. Warashina, Y. Kubota, T. Nakamura, Y. Hayakawa, M. Tanaka, K. Isobe, and H. Tatsuoka, “Synthesis of single-phase polycrystalline Ca2Si powder and sintered compacts”, International Journal of Materials Research 102 (2011) 401-405.

[80] Q. Yang, M. Tanaka, S. Liang, K. Ogino, H. Fujii, A. Ishida, and H. Tatsuoka, “Simple Synthesis of ZrO2/SiOx core/shell nanofibers using ZrSi2 with gallium”, Thin Solid Films 519 (2011) 8538-8541.

[81] B. Zheng, N. Iketa, K. Sato, SATO Rodrigo, M. Song, Y. Takeda, H. Amekura, K. Oyoshi, K. Kono, D. Ila, N. Kishimoto, “Development and irradiation performance of stencil masks for heavy-ion patterned implantation”, SURFACE & COATINGS TECHNOLOGY, 206, (2011) 806-811.

[82] B. Zheng, M. Song, B. Chhay, Z. Xiao, R.L. Zimmerman, A. Sharma, N. Kishimoto, D. Ila, “Spectroscopic analysis of dipole interaction of metallic nanoparticles in dielectric multilayer dielectric thin film”, VACUUM 84 (2010) 1302-1305.

[83] H. X. Lu, T. Hoshiba, N. Kawazoe, I. Koda, M. Song, G.P. Chen, “Cultured cell-derived extracellular matrix scaffolds for tissue engineering”, 呂宏旭 , 干場隆志 , 川添直輝 , Ichie Koda, 長谷川明 , 陳国平 , Biomaterials 32 (2011) 9658-9666.

[84] J. Zhang, Y. Wang, X. Ding, Z. Zhang, Y. Zhou, X. Ren, K. Otsuka, J. Sun, and M. Song, “Stress-induced strain glass to martensite (R) transition in a Ti50Ni44.5Fe5.5 alloy”, Physical Review B 83, (2011) 174204-1-174204-8).

[85] J. Zhang, Y. Wang, X. Ding, Z. Zhang, Y. Zhou, X. Ren, D. Wang, Y. Ji, M. Song, K. Otsuka, J. Sun, “Spontaneous strain glass to martensite transition in a Ti(50)Ni(44.5)Fe(5.5) strain glas”, Physical Review B 84, (2011) 214201-1-214201-7.

国内誌

[86] 原　徹、田中啓一、前畑京介、満田和久、“透過型電子顕微鏡の組成分析への超伝導遷移端センサの応用”、応用物理、81-2、139-142、(2012).

[87] 竹口雅樹 , 橋本綾子 , 三石和貴 , 下条雅幸 , “走査型共焦点電子顕微鏡法の開発”, 顕微鏡 , 46　(2011) 61 ～ 65.

解説

[88] 木本浩司, 長井拓郎 , “ローレンツ顕微鏡法と電子エネルギー損失分光法による強相関電子系材料の微細構造の観察”, まぐね（日本磁気学会）, vol. 6, 329-332 (2011).

[89] 秩序型ダブルペロブスカイトにおける磁区と結晶学的ドメインの結合 , 浅香透 , 于秀珍 , 木本浩司 , 松井良夫 , 日本結晶学会誌 ,53,2,119-123,(2011)

著書

[90] 原　徹、“2.1. 電子線による EDS 分析”, 環境・エネルギー材料ハンドブック III 技術編、第 2 章分析技術 ,682-693,(2011)

[91] M. Shimojo, K. Mitsuishi, M. Takeguchi, M. Tanaka and K. Furuya, “Nanofabrication using electron beam-induced deposition techniques” Encyclopedia of Nanoscience and Nanotechnology vol.17 (2011) 209-230.

■強磁場固体ＮＭＲ計測技術の開発と先進材料応用

国際誌

[92] 後藤敦 , 大木忍 , 端健二郎 , 清水禎 , “Optical switching of nuclear spin-spin couplings in semiconductors”, NATURE COMMUNICATIONS , Vol.115, No.20,10284-10291,（2011）.

[93] 後藤和馬 , 武田和行 , Michael M. Lerner, 末石芳巳 , 丸山晋平 , 後藤敦 , 丹所正孝 , 大木忍 , 端健二郎 , 石田祐之 ,, “Analysis of bis(trifluoromethylsulfonyl)imide-doped paramagnetic graphite intercalation compound using 19F very fast magic angle ”, CARBON, Vol.49, No.12, 4064-4066 , (2011).

[94] Ono T, Shimoda K, Tsubota M, Kohara S, A Ichikawa, T Kojima, 丹所正孝 , 清水禎 , Kojima Y, “Ammonia Desorption Property and Structural Changes of LiAl(NH(2))(4) on Thermal Decomposition ”, JOURNAL OF PHYSICAL CHEMISTRY C , Vol. 115, No.20, 10289-10291, （2011）

[95] 後藤敦 , 大木忍 , 端健二郎 , 清水禎 , “Optical-pumping double-nuclear-magnetic-resonance system with a Gifford McMahon cryocooler”, JAPANESE JOURNAL OF APPLIED PHSICSY, Vol.50, No.12,126701-1-126701-5 (2011).

著書

[96] 後藤 敦、大木 忍、端健二郎、清水 禎, “発核スピンの光制御を用いた量子コンピュータ実現に向けて”, NIMS NOW, Vol.11 No.7 p. 10,(2011))

[97] Atsushi Goto, Shinobu Ohki, Kenjiro Hashi and Tadashi Shimizu, "Optical control of nuclear spins in solid-state NMR quantum computers", NIMS NOW International, Vol. 11. No. 7 p. 10, September,(2011)

■強力中性子線計測技術の開発と先進材料応用

国際誌

[98] M. Mihalik, J. Prokleška, J. Kamarád, K. Prokeš, O. Isnard, G. J. McIntyre, A. Dönni, S. Yoshii, H. Kitazawa, V. Sechovský, and F. R. de Boer, “NdRhSn: A ferromagnet with an antiferromagnetic precursor”, Phys. Rev. B 83, 104403-1-10 (2011).

[99] A. Donni, H. Kitazawa, T. Stässle, L. Keller, M. Matsuda, K. Kakurai, G. Ano, M. Akatsu, Y. Nemoto, T. Goto, “Crystal Field Level Diagrams at the Pr Sites (8c) and (4a) in the Clathrate Compound Pr3Pd20Si6”, Journal of the Physical Society of Japan 80, 0447151-8 (2011).

[100] A. Oyamada, T. Kaibuchi, M. Nishiyama, T. Itou, S. Maegawa, Y. Isikawa, A. Dönni, and H. Kitazawa,” Critical behavior in a Kondo-screening partially-ordered antiferromagnet CePdAl”, Journal of Physics: Conference Series 320, 012067 (2011).

[101] P. Holec J. P. Vejpravova, J. Plocek, I. Nemec, H. Kitazawa, D. Niznansky, “ACr2O4 /SiO2 (A = Zn, Cu, Cd) nanocomposites, their preparation and physical properties”, IOP Conf. Series: Materials Science and Engineering 18, 032024 (2011).

[102] G. Ano, K. Matsuo, K. Araki, Y. Tachikawa, K. Mitsumoto, M. Akatsu, Y. Nemoto, T. Goto, N. Takeda, A. Kikkawa, A. Dönni and H. Kitazawa, “Quadrupole Ordering and Rattling in Clathrate Compound Pr3Pd20Ge6“, Journal of Physics: Conference Series 273, 012002-1-4 (2011).

[103] J. P. Vejpravova, J. Prokleska, V. Vales, S. Danis, A. Mantlikova, V. Holy, P. Brazda, S. Doyle, C. Ritter, H. Kitazawa, D. Niznansky, “High-Coercivity Iron Oxide Based Nanocomposites – Particle Shape and Magnetic Structure by Synchrotron and Neutron Scattering”, IOP Conf. Series: Materials Science and Engineering 18 , 022010-1-4 (2011).

[104] H. Kuroe, T. Hamasaki, T. Sekine, M. Hase, K. Oka, T. Ito, H. Eisaki, K. Kaneko, N. Metoki, M. Matsuda, and K. Kakurai, “Hybridization of magnetic excitations between quasi-one-dimensional spin chains and spin dimers in Cu3Mo2O9 observed using inelastic neutron scattering”, Phys. Rev. B 83, 184423 1-8 (2011).

[105] H. Kuroe, R. Kino, T. Hosaka, M. Suzuki, S. Hachiuma, T. Sekine, M. Hase, K. Oka, T. Ito, H. Eisaki, M. Fujisawa, S. Okubo, and H. Ohta, “Electric polarization induced by Neel order without magnetic superlattice: experimental study in Cu3Mo2O9 and numerical one in a small spin cluster”, J. Phys. Soc. Jpn. 80, 083705 1-4 (2011).

[106] M. Hase, V. Yu. Pomjakushin, V. Sikolenko, L. Keller, H. Luetkens, A. Dönni, and H. Kitazawa, “Negative magnetization of Li2Ni2Mo3O12 having a spin system composed of distorted honeycomb lattices and linear chains”, Phys. Rev B 84, 104402 1-8 (2011).

[107] K. Oka, T. Ito, H. Eisaki, M. Hase, T. Hamasaki, H. Kuroe, and T. Sekine, “Crystal growth of Cu3-xZnxMo2O9 by continuous solid-state crystallization method,” J. Crystal Growth 334, 108-112 (2011).

[108] S. Abe, DH. Ping, M. Ohnuma, S. Ohnuma, "Selective Product of Magnetite through Addition of Small Amount of Metal Element" JJAP 50, 063002

[109] J. Saida, K. Ito, T. Sanada, S. Sato, M. Imafuku, M. Ohnuma, A. Inoue, "Atomic structure of nanoscale quasicrystal-forming Zr-noble metal binary metallic glasses", J. Alloys & Compounds 509, S27-S33 (2011).

[110] ES. Park, M. Ohnuma, DH. Kim, "Anormalous glass transition behavior in Cu-Zr-Sn alloy system", J. Alloys & Compounds 509, S52-S55 (2011).

[111] J. Saida, T. Sanada, S. Sato, M. Imafuku, M. Ohnuma, T. Ohkubo, K. Hono, E. Matsubara, "Change in local environment upon quaicrystallization of Zr-Cu glassy alloys by addition of Pd and Pt", J.Physics-condensed matter 23, 175302 (2011).

[112] S. Hasegawa, S. Takahashi, H. Iwase, S. Koizumi, N. Morishita, K. Sato, T. Narita, M. Ohnuma, Y. Maekawa, "Radiation-induced graft polymerization of functional monomer into poly(ether ether ketone) film and structure-property analysis of the grafted membrane", Polymer 52, 98-106(2011).

[113] S.A. EL-Safty, A. Shahat, W Warkocki, M. Ohnuma, "Buiilding-block-based mosaic cage silica nanotube for molecular transport and separation.", Small 7, 62-65(2011).

[114] Y. Oba, S. Koppoju, M. Ohnuma, T, Murakami, H. Hatano, K. Sasakawa, A. Kitahara, J. Suzuki, "Quantitative Analysis of Precipitates in Vanadium-microalloyed Medium Carbon Steels Using Small-angle X-ray and Neutron Scattering Methods", ISIJ International, 51, 1852-1858 (2011).

[115] Y. Su, Y. Tomota, J. Suzuki, M. Ohnuma, "Hydrogen behaviorin an Ultrafine-Grained Electrodeposited Pure Iron", ISIJ international 51, 1534-1538 (2011).

[116] M. Ohnuma, G. Herzer, P. Kozikowsky, C. Polak, V. Budinsky, S. Koppoju, "Structural anisotropy of amorphous alloys with creep-induced magnetic anisotropy", Acta Materialia 60, 1278-1286(2012).

[117] Y. Oba, S. Koppoju, M. Ohnuma, Y. Kinjo, S. Morooka, Y. Tomota, J. Suzuki, D. Yamaguchi, S. Koizumi, M. Sato, T. Shiraga, "Quantitative Analysis of inclusions in low carbons steel using small-angle X-ray and neutron scattering", ISIJ International 52, 457-463 (2012).

[118] H. Kuroe, T. Hamasaki, T. Sekine, M. Hase, K. Oka, T. Ito, H. Eisaki, K. Kaneko, N. Metoki, M. Matsuda, and K. Kakurai, Hybridization of magnetic excitations between quasi-one-dimensional spin chains and spin dimers in Cu3Mo2O9 observed using inelastic neutron scattering, Phys. Rev. B 83, 184423 1-8 (2011).

[119] H. Kuroe, R. Kino, T. Hosaka, M. Suzuki, S. Hachiuma, T. Sekine, M. Hase, K. Oka, T. Ito, H. Eisaki, M. Fujisawa, S. Okubo, and H. Ohta, Electric polarization induced by Neel order without magnetic superlattice: experimental study in Cu3Mo2O9 and numerical one in a small spin cluster, J. Phys. Soc. Jpn. 80, 083705 1-4 (2011).

[120] K. Oka, T. Ito, H. Eisaki, M. Hase, T. Hamasaki, H. Kuroe, and T. Sekine, Crystal growth of Cu3-xZnxMo2O9 by continuous solid-state crystallization method, J. Crystal Growth 334, 108-112 (2011).

[121] H. Takeya, H. Fujii, M. ElMassalami, F. Chaves, S. Ooi, T. Mochiku, Y. Takano, K. Hirata, K. Togano, “A new noncentrosymmetric superconducting phase in the Li-Rh-B system”, J. Phys. Soc. Jpn., 80, 013702 (2011).

[122] M. Nishino, C. Enachescu, S. Miyashita, P. A. Rikvold, K. Boukheddaden, F. Varret,

[123] “Macroscopic nucleation phenomena in continuum media with long-range interactions”,

[124] Sci. Rep. (Nature PG) 1, 162; DOI:10.1038/srep00162 (2011).

[125] T. Nakada, P. A. Rikvold, T. Mori, M. Nishino, and S. Miyashita, “Crossover between a Short-range and a Long-range Ising model”, Phys. Rev. B. 84, 054433-(1-9) (2011).

[126] T. Nakada, T. Mori, S. Miyashita, M. Nishino, S. Todo, W. Nicolazzi, and P. A. Rikvold, “Critical temperature and correlation length of an elastic interaction model for spin-crossover materials”, Phys. Rev. B. 85, 054408-(1-8) (2012).

[127] H. Mamiya and B. Jeyadevan, , "Formation of non-equilibrium magnetic nanoparticle structures in a large alternating magnetic field and their influence on magnetic hyperthermia treatment", IEEE Transactions on Magnetics, in press.

[128] H. Mamiya and S. Nimori, "Memory effects in Heisenberg spin glasses: Spontaneous restoration of the original spin configuration rather than preservation in a frozen state", Journal of Applied Physics Vol.111 (2012) 07E147-1-3

[129] H. Mamiya and B. Jeyadevan, , "Optimal design of nanomagnets for targeted hyperthermia", Journal of Magnetism and Magnetic Materials Vol.323 (2011) 1417-1422

[130] H. Mamiya and B. Jeyadevan, "Hyperthermic effects of dissipative structures of magnetic nanoparticles in large alternating magnetic fields", Scientific Reports Vol.1 (2011) 00157-1-7.

[131] H. Mamiya, N. Terada, H. Kitazawa, A. Hoshikawa, and T. Ishigaki,

[132] "Structural and Magnetic Properties of Dilute Spinel Ferrites: Neutron Diffractometry and Magnetometry Investigations", Journal of Magnetics Vol.16 (2011) 134-139

[133] N. Tsujii, C. A. Uvarov, P. Klavins, T. Yi, S. M. Kauzlarich, “Crystal Structure and a Giant Magnetoresistance Effect in the New Zintl Compound Eu3Ga2P4”, Inorg. Chem. 51, 2860 (2012).

[134] N. Tsujii, M. Imai, H. Kitazawa, “Superconducting properties and thermal expansion of YbGaxSi2-x”, J. Phys.: Conf. Ser. 344, 012012 (2012).

[135] J. H. Roudebush, N. Tsujii, A. Hurtando, H. Hope, Y. Grin, S. M. Kauzlarich, “Phase Range of the Type-I Clathrate Sr8AlxSi46-x and Crystal Structure of Sr8Al10Si36”, Inorg. Chem. 51, 4161 (2012)

[136] H. Yamaoka, P. Thunstrom, I. Jarrige, K. Shimada, N. Tsujii, M. Arita, H. Iwasawa, H. Hayashi, J. Jiang, T. Habuchi, D. Hirayama, H. Namatame, M. Taniguchi, U. Murao, S. Hosoya, A. Tamaki, H. Kitazawa, “High-resolution photoelectron spectroscopy study of Kondo metals: SmSn3 and Sm0.9La0.1Sn3”, Phys. Rev. B 85, 115120 (2012).

[137] H. Yamaoka, I. Jarrige, N. Tsujii, A. Kotani, J.F. Lin, F. Honda, R. Settai, Y. Onuki, N. Hiraoka, H. Ishii, K.D. Tsuei, “Pressure and Temperature Dependences of the Electronic Structure of CeIrSi3 Probed by Resonant X-ray Emission Spectroscopy”, J. Phys. Soc. Japan 80, 124701 (2011).

[138] H. Yamaoka, I. Jarrige, N. Tsujii, J.F. Lin, T. Ikeno, Y. Ishikawa, K. Nishimura, R. Higashinaka, H. Sato, N. Hiraoka, H. Ishii, and K.D. Tsuei, “Strong Coupling between 4f Valence Instability and 3d Ferromagnetism in YbxFe4Sb12 Studied by Resonant X-ray Emission Spectroscopy”, Phys. Rev. Lett. 107, 177203 (2011).

[139] A. Ohmura, K. Fujimaki, F. Ishikawa, Y. Yamada, N. Tsujii, M. Imai, “Pressure effect on critical temperature for superconductivity and lattice parameters of AlB2-type ternary silicide YbGa1.1Si0.9”, Phys. Rev. B 84, 104520 (2011).

[140] S. Kimura, T. Fujita, N. Nishihagi, H. Yamaguchi, T. Kashiwagi, M. Hagiwara, N. Terada, Y. Sawai and K. Kindo, “Multi-frequency ESR measurements of the triangular lattice antiferromagnet CuFeO2 in high magnetic fields”, Phys. Rev. B 84 104449 (2011).

[141] N. Terada, Y. Tsuchiya, H. Kitazawa, T. Osakabe, N. Metoki, N. Igawa and K. Ohoyama, “Magnetic correlations and the influence of atomic disorder in frustrated isosceles triangular lattice antiferromagnet CuMnO2”, Phys. Rev. B 84 064432 (2011).

[142] T. Nakajima, A. Sunou, S. Mitsuda, N. Terada, S. Kimura, K. Kaneko and H. Yamauchi, “Magnons and electromagnons in a spin-lattice-coupled frustrated magnet CuFeO2 as seen via inelastic neutron scattering”, Phys. Rev. B 84 184401 (2011).

[143] A. J. Princep, A. M. Mulders, E. Schierle, E. Weschke, J. Hester, W. D. Hutchison, Y. Tanaka, N. Terada, Y. Narumi and T. Nakamura,“High-order Ho multipoles in HoB2C2 observed with soft resonant x-ray diffraction”, J. Phys. Cond. Matter 24 075602 (2012).

[144] N. Terada, T. Osakabe and H. Kitazawa,“High-Pressure Suppression of Long Range Magnetic Order in the Triangular Lattice Antiferromagnet CuFeO2”, Phys. Rev. B 83 020403R (2011).

[145] S. Mitsuda, K. Yoshitomi, T. Nakajima, C. Kaneko, H. Yamazaki, M. Kosaka, N. Aso, Y. Uwatoko, Y. Noda, M. Matsuura, N. Terada, S. Wakimoto, M. Takeda, K. Kakurai,“Uniaxial-stress enhancement of spin-driven ferroelectric polarization in a multiferroic CuFe1-xGaxO2”, J. Phys. Conference Series 340 012062 (2012).

国内誌

[146] 茂筑高士 , 小澤清 , 土屋佳則 , 井川直樹 ,“サイクル耐久性に優れたリチウムイオン二次電子正極材”, 中性子産業利用推進協議会季報「四季」, 11, 3 (2011).

[147] 間宮広明 ," 磁性ナノ粒子を用いたがんの温熱治療 その詳細な発熱メカニズムをはじめて解明 ", 月刊化学 査読無 67 (2012) 77-77.

解説

[148] 長谷正司 ,“金森 -Goodenough 則”, コラム : メイドインジャパン物理用語, パリティ, 2011 年 8 月号 P39

[149] 大沼正人,“小角散乱法によるナノサイズ不均質の評価”, 表面科学 , 33, 278-283(2012)

[150] 大沼正人,“金属組織研究への小角散乱の利用”, 非破壊検査, 60, 86-92(2011)

[151] 間宮広明 , バラチャンドラン ジャヤデワン,”磁性流体 : 研究の動向と今後の展開”、磁性流体研究連絡会ニュースレター ,47,12-15,(2011)

著書

[152] H. Kitazawa and K. Hashi,“Structural and Thermodynamic Properties of Fullerene Nanowhiskers”, Fullerene Nanowhiskers (Edited by K. Miyazawa, Pan Stanford publishing), Chapter 13, (2011) 185-196.

■放射光を利用した先進計測技術の開発と先進材料応用

国際誌

[153] Vallerie Ann Innis-Samson and Kenji Sakurai, Hydrophobic switching nature of methylcellulose ultra-thin films: thickness and annealing effects, J. Phys.: Condens. Matter 23, 435010 (2011).

[154] Vallerie Ann Innis-Samson, Mari Mizusawa, and Kenji Sakurai, X-ray Reflection Tomography: A New Tool for Surface Imaging,, Anal. Chem., 83, 7600-7602 (2011).

[155] Krassimir Stoev and Kenji Sakurai, Aberration effects in quick X-Ray reflectivity of curved samples, IOP Conference Series: Materials Science & Engineering, 24, 012014 (2011).

[156] Mari Mizusawa and Kenji Sakurai, In-situ X-ray reflectivity measurement of polyvinyl acetate thin films during glass transition, IOP Conference Series: Materials Science and Engineering, 24, 012013 (2011).

2. 口頭発表

■先端表面敏感計測技術の開発と先進材料応用

国際会議（招待）

[157] 2012/03/01-02 : D. Fujita, T. Iwasaki, K. Ishige, H. Guo, X. Mingsheng : “Standardization of Data Treatment and Management of Scanning Probe Microscopy” 3rd International Symposium on Stadardization of SPM

[158] 2012/03/01-02 : D. Fujita, T. Iwasaki, K. Ishige : “GUIDELINE FOR RESTORATION PROCEDURE OF ATOMIC FORCE MICROSCOPY IMAGES DILATED BY FINITE PROBE SIZE” The 3rd International Symposium on Stadardization of SPM

[159] 2012/03/01-02 : D. Fujita, T. Iwasaki, K. Ishige : “GUIDELINE FOR OPTIMIZATION OF SCANNING CONDITIONS FOR ATOMIC FROCE MICROSCOPY TOPOGRAPHY IMAGING” The 3rd International Symposium on Stadardization of SPM

[160] 2011/12/06 : D. Fujita : “Measurements and analysis of nano materials” APMP2011 SYMPOSIUM

国内学協会会議（招待・依頼）

[161] 2012/02/27 : 藤田大介, 石田暢之, GUOHongxuan : “Introduction of Nano Interface Chracterization for Environmental and Energy Materials Research” 第3回ナノ材料科学環境拠点シンポジウム

[162] 2012/02/23 : 藤田大介 : “先端材料計測技術の開発と応用プロジェクトの目指すもの” NIMS 先端計測シンポジウム 2012

[163] 2011/12/09 : 藤田大介 : “先端材料の開発に必要な基盤計測技術” 第3回 AIST-NIMS 計測分析シンポジウム

[164] 2011/11/17 : 藤田大介 : “グラフェン超薄膜の顕微ラマンイメージング解析” Inside Raman Tokyo seminar 2011

[165] 2011/10/26 : 藤田大介 : “先端的共通技術部門の紹介” 第11回 NIMS フォーラム

[166] 2011/10/25 : 藤田大介 : “NIMS 先端材料計測プロジェクトの概要” NIMS-AIST（NRI）計測・計算シミュレーション合同 WS

国際会議（一般）

[167] 2011/12/11-15 : K. Sagisaka, M. Michael, D. Fujita, Davoid Bowler : “STM and DFT study on adsorption of phosphorus molecules on the Si(100) surface” The 6th International Symposium on Surface Science

[168] 2011/12/11-15 : M. Michael, K. Sagisaka, D. Fujita : “Investigation of the growth mode and electronic properties of Ni-clusters grown on HOPG by scanning tunneling microscopy” 6th. International Symposium on Surface Science

[169] 2011/12/11-15 : C. Leon, K. Sagisaka, D. Fujita, L. Han : “Surface States of Anatase TiO2(101): an STM and STS Study” 6th International Symposium on Surface Science

[170] 2011/12/11-15 : J. Gao, N. Ishida, D. Fujita : “Epitaxial Growth of Graphene and Boron Nitride Layers on Metal Surfaces by Surface Segregation” International Symposium on Surface Science (ISSS-6)

[171] 2011/11/08-11 : J. Gao, N. Ishida, D. Fujita : “Characterization of graphene and boron nitride layers on metal surfaces by surface segregation” The 15th International Conference on Thin Films (ICTF-15)

[172] 2011/10/23-26 : J. Gao, D. Fujita : “Synthesis and Characterization of Graphene on Metal Substrates” BIT's 1st Annual World Congress of Nano-S&T

[173] 2011/09/07-09 : J. Gao, K. Sagisaka, N. Ishida, D. Fujita : “Epitaxial Growth of Single-layer Graphene on Pt(111) and Pd(111) by Surface Segregation” International Conference on Nanoscience & Technology China 2011

国内学協会会議（一般）

[174] 2012/03/24-27 : 鷺坂恵介, MICHAELMarz, 藤田大介, デッビドボウラー :“Si(100) 表面におけるリン分子の吸着構造”日本物理学会第 67 回年次大会

[175] 2012/03/24-27 : MICHAELMarz, 鷺坂恵介, 藤田大介 :“STM による HOPG 表面におけるニッケルクラスターの成長様式と電子状態の研究”日本物理学会第 67 回年次大会

[176] 2012/03/24-27 : PEREZ LEONCarmen, 鷺坂恵介, 藤田大介, 韓礼元 :“STM を用いた TiO2 表面における光増感色素の吸着研究”日本物理学会第 67 回年次大会

[177] 2011/12/15-17 : 大西桂子, 藤田大介 :“ナノ線幅計測のための AFM 像探針形状効果補正”第 31 回表面科学学術講演会

[178] 2011/12/02 : 鷺坂恵介, 藤田大介 :“Si(111)-7x7 表面のアダトム操作と走査トンネル分光”平成 23 年度オープン研究会　走査型プローブ顕微鏡における最先端技術

[179] 2011/10/25 : 鷺坂恵介, 藤田大介 :“STM 計測および DFT 計算を用いた Si(100) 表面のリン分子吸着構造の解析”NIMS -AIST 計測・計算シミュレーション合同ワークショップ

[180] 2011/08/29 - 2011/09/02 : 石田暢之 , 藤田大介 :“ルチル型 TiO2(110) 表面に吸着したフタロシアニンの STM 観察”2011 年秋季 第 72 回 応用物理学会学術講演会

[181] 2011/05/16-18 : 大西桂子, GUOHongxuan, 藤田大介 :“走査型ヘリウムイオン顕微鏡によるグラフェン超薄膜のナノスケール計測・加工”日本顕微鏡学会学術講演会（第 67 回）

[182] 2011/05/16-18 : 三石和貴 , 大西剛 , 高田和典 , 橋本綾子 , 藤田大介 , 竹口雅樹 , 大野隆央 , 奈良純 :“(111) 配向した La0.55 Li0.33TiO3 膜中の板状欠陥の高分解能 STEM 観察”日本顕微鏡学会 67 回学術講演会

■先端表層領域計測技術の開発と先進材料応用

国際会議（招待）

[183] Vladimir Matolin, Iva Matolinova, H.Yoshikawa, K.Kobayashi, Blanka Detlefs, “HAXPES INVESTIGATION OF NANOSTRUCTURED PEM FUEL CELL CATALYSTS” HAXPES2011, Deutsches Elektronen-Synchrotron DESY,Hamburg, Bundesrepublik Deutschland , (2011.9.14-16).

国内学協会会議（招待・依頼）

[184] 田沼繁夫,“研究・開発とX線分析”, 第 35 回湘南ハイテクセミナー, 神奈川大学総合理学研究所 , 神奈川 , 日本 , (2011.12.1-2).

[185] 田沼繁夫 , 永富隆清 ,“感度係数法による表面定量分析”, マイクロビームアナリシス第 141 委員会第 146 回委員会 , 立命館大学びわこ草津キャンパス , 草津 , 日本 , (2011.11.24-25).

[186] 吉川英樹 ,“SPring-8 における HAXPES の現状と将来”, 日本表面科学会　第 71 回表面科学研究会 , 東京理科大学　森戸記念館 , 東京 , 日本 , (2012.2.2).

[187] 岩井秀夫 ,“中エネルギー分解能 AES －元素分析のためのエネルギー軸目盛の校正”, 表面分析実用化セミナー '11, 島津製作所 関西支社 マルチホール , 大阪 , 日本 , (2011.7.22).

[188] 岩井秀夫 ,“オージェ電子分光法（AES）”, 第 51 回 表面科学基礎講座「表面・界面分析の基礎と応用」, 東京理科大学 1 号館 17 階会議室 , 東京 , 日本 , (2011.06.28-30).

[189] 篠塚寛志 ,“第 1 原理計算による化合物半導体の誘電関数の計算”, 第 31 回表面科学学術講演会 , タワーホール船堀 , 東京 , 日本 , (2011.12.15-17).

[190] 吉川英樹 , 山下良之 , 長田貴弘 ,“実用デバイスにおける電圧駆動状態での in-situ 硬X線光電子分光”, 平成 23 年度 GINO 研究領域創成支援プロジェクトワークショップ, 国際ファッションセンター , 東京 , 日本 , (2012.3.21-22).

国際会議（一般）

[191] H.Shinotsuka, S.Tanuma, C.J. Powell, D.R. Penn,“Calculations of electron stopping powers for 41 elemental solids over the 50 eV to 30 keV range with the full Penn algorithm” ECAISA 11, Cardiff City Hall,Cardiff, Wales , UK, (2011.09.04-09).

[192] H.Iwai, M.Kobata, PIS Igor, H.Nohira, K.Kobayashi,“Application of laboratory type hard X-ray photoelectron spectroscopy system to more than 10 nm thickness overlayer thin films” 14th Europ. Conf. on Appl. of Surf. and Interf. (ECASIA), Cardiff City Hall,Cardiff, Wales , UK, (2011.09.04-09).

[193] H.Shinotsuka, H.Yoshikawa, S.Tanuma,“Evaluation of model energy loss functions for electron inelastic scattering in solids” ECAISA 11, Cardiff City Hall,Cardiff, Wales , UK, (2011.09.04-09).

[194] S.Fukushima, H.Shinotsuka, Y.Sonobayashi,“The Binding Energy Shift of Ag 3d between Ag2O and Ag2O2”, 14th Europ. Conf. on Appl. of Surf. and Interf. (ECASIA), Cardiff City Hall,Cardiff, Wales , UK, (2011.09.04-09).

[195] S.Fukushima, T.Kimura, H.Iwai, Y.Sejimo, Y.Kariya,“AES Analysis for The Oxide Layer between Stainless Steel and Metallic Tin” Cardiff City Hall,Cardiff, Wales , UK, (2011.09.04-09).

[196] S.Fukushima, S.Araki, Y.Iijima, N.Ishizu, H.Itoh, H.Iwai, M.Iwai, E.Iwase, T.Morimoto, K.Omura, M.Sato, M.Soma, K.Takahashi, M.Takano, Y.Takeuchi, Y.Tsujimoto, H,Yasufuku, A.Tanaka, K.Goto,“The Round-robin Test of Dispersion of Signal Intensity on XPS” Cardiff City Hall,Cardiff, Wales , UK, (2011.09.04-09).

[197] H.Yoshikawa, Hua Jin, H.Tanaka, H.Shinotsuka, H.Iwai, RAI Masao, Sven Tougaard, S.Tanuma,“Dielectric functions of GaAs and GaSb by factor analysis of reflection electron energy loss spectra” Cardiff City Hall,Cardiff, Wales , UK, (2011.09.04-09).

[198] H.Yoshikawa, SHIMODA Masahiko, Mitsuhiro Arisawa, Shuto Satoshi, Tomoya Konishi, Shiro Tsukamoto, Y.Yamashita, Shigenori Ueda, K.Kobayashi,“IMMOBILIZED PALLADIUM CATALYSTS ON SULFUR-TERMINATED SUBSTRATE STUDIED BY HARD X-RAY PHOTOEMISSON” HAXPES2011, Deutsches Elektronen-Synchrotron DESY,Hamburg, Bundesrepublik ,Deutschland , (2011.9.14-16).

国内学協会会議（一般）

[199] 石岡邦江 , H. Petek,“E0 ギャップ近傍で励起したガリウム砒素のコヒーレントフォノンの光検出メカニズム２”, 日本物理学会第 66 回年次大会 , 富山大学 , 富山市 , 日本 , (2011.9. 21-24).

[200] 田沼繁夫 ,“角度分解一反射電子スペクトルを用いた誘電関数計測法の開発と応用 / 角度分解一反射電子スペクトルを用いた誘電関数計測法の開発と応用 ”, NIMS-AIST 計算・計測シミュレーション合同 WS, 産業技術総合研究所 , つくば , 日本 ,(2011.10.25).

[201] 篠塚寛志 , 田沼繁夫 , C.J. Powell, D.R. Penn,“10eV - 30 keV における固体中の電子阻止能の計算”, 第 31 回表面科学学術講演会 , タワーホール船堀 , 東京 , 日本 , (2011.12.15-17).

[202] 篠塚寛志 , 吉川英樹 , 田沼繁夫 ,“ 固体中における電子の非弾性散乱に関するモデルエネルギー損失関数の u ひょう”, 2011 年度 実用表面分析講演会 , 東京大学 , 東京 , 日本 , (2011.10.17-18) .

[203] 荻原俊弥 , 永富隆清 , 田沼繁夫 ,“高傾斜試料ホルダーを用いた極低角度電子・イオン入射オージェ深さ方向分析”, 日本分析化学会第 60 年会 , 名古屋大学 , 名古屋市 , 日本 , (2011.9.14-16).

[204] 荻原俊弥， 永富隆清， 田沼繁夫 ,“極低角度入射ビームを用いた高感度， 高分解能オージェ深さ方向分析による極薄膜多層試料の分析”, 2011 年度実用表面分析講演会 , 東京大学 , 東京 , 日本 , (2011.10.17-18) .

[205] 荻原俊弥， 永富隆清， 田沼繁夫 ,“極低角度入射ビームを用いた極薄膜多層試料のオージェ深さ方向分析”, 第３１回表面科学学術講演会 , タワーホール船堀 , 東京 , 日本 ,(2011.12.15-17).

[206] 田中彰博 , 木村隆， 福島整 , 岩井秀夫， 荻原俊弥， 田沼繁夫 ,“ VAMAS- 電子ビーム損傷ラウンドロビン試験報告”, 表面科学会 , 名城大学名駅サテライト , 名古屋 , 日本 (2012.02.09-10)

■超先端電子顕微鏡技術の開発と先進材料応用

国際会議（招待）

[207] K. Kimoto, Status report of NIMS-Titan; preliminary results at 80 kV TEM and STEM, FEI “Acht 2011” Meeting Program, FEI Company & FEI Japan Ltd.,2011/07/20-2011/07/22

[208] T.Hara, K.Tsuchiya, K.Tsuzaki, X.Man, T.Asahata and A.Uemoto, “Application of orthogonally-arranged SEM-FIB to microstructure analysis of martensite”, International Conference on Martensitic Transformations 2011,Osaka, Japan, 2011/09/04-2011/09/09

[209] M. Takeguchi, K. Mitsuishi, L. Dan and M. Shimojo, Name, “Electron holography combined with a stage-scanning system” IUMAS-V, Seoul (Korea), 2011/05/22-2011/05/27.

[210] PD. Nellist, P. Wang, AI. Kirkland, JD. Adrian, AJ. Morgan LJ. Allen, A. Hashimoto, M. Takeguchi, K. Mitsuishi and M. Shimojo, “Aberration-corrected scanning confocal electron microscopy for three-dimensional imaging and analysis of materials” FEMMS2011, California (USA), 2011/09/18-2011/09/23.

[211] PD. Nellist, P. Wang, AI. Kirkland, JD. Adrian, AJ. Morgan LJ. Allen, A. Hashimoto, M. Takeguchi, K. Mitsuishi and M. Shimojo, “Optical sectioning and confocal microscopy in an aberration-corrected transmission electron microscope for three-dimensional imaging and analysis of materials”, International Symposium on Advanced Electron Microscopy, Beijing (China), 2012/01/05-2012/01/07.

[212] M. Tanaka and M. Takeguchi, “Si nano-dot formation in oxidezed Si film by TEM electron beams”, 1st Asia-Arab Sustainable Energy Forum, Nagoya (Japan), 2011/08/23-2011/08/26.

国内学協会会議（招待・依頼）

[213] 木本浩司 , 高分解能 TEM-EELS による極微小領域の結晶構造解析 , ナノプローブテクノロジー第 167 員会 , 日本学術振興会 ,2011/01/11-2011/01/11

[214] 木本浩司 ,EELS 基礎 , 第 27 回分析電子顕微鏡討論会 , 日本顕微鏡学会　分析電子顕微鏡分科会 ,2011/09/06-2011/09/07

[215] 木本浩司 ,Spatially-resolved diffractometry による原子コラムの観察 , 超分解能電子顕微鏡分科会 , 日本顕微鏡学会 ,2011/11/29-2011/11/29

[216] 原徹、直交配置型 SEM-FIB の特徴と金属材料観察への応用 , 日本学術振興会 132 委員会　第 196 回研究会 , 日本学術振興会 ,2011/07/29-2011/07/29

[217] 原徹、TES 型 X 線検出器の透過型電子顕微鏡分析装置としての応用 , 日本学術振興会第 141 委員会　第 145 回研究会 , 日本学術振興会 ,2011/09/15-2011/09/16

[218] 原徹 ,TEM での EDS 分析はどこまで定量できるか - 現状と課題 -, 日本顕微鏡学会デバイス解析分科会　電子顕微鏡解析技術フォーラム , 日本顕微鏡学会デバイス解析分科会 ,2011/08/26-2011/08/27

[219] 原徹 , 金属材料組織観察を目的とした直交配置型 FIB-SEM　- 特長と応用例 -, SMA シンポジウム 2011, 社団法人形状記憶合金協会 ,2011/11/25-2011/11/25

[220] 原徹 ,TEM/STEM での EDX の応用について , 学振 141 委員会研修セミナー , 日本学術振興会　マイクロビームアナリシス第 141 委員会 ,2011/12/01-2011/12/02

[221] 原徹 , 直交配置型 FIB-SEM の特徴と金属材料組織観察への応用 , 平成 23 年度マテリアル電子線トモグラフィ研究部会講演会 , 日本顕微鏡学会マテリアル電子線トモグラフィ研究部会 ,2011/12/16-2011/12/16

[222] 三石和貴 , 橋本綾子 , 下条雅幸 , 竹口雅樹 , 石塚和夫 ,“共焦点電子顕微鏡法による 3 次元観察の可能性”荷電粒子ビームの工業への応用第 132 委員会第 199 回研究会 , 東京 (日本), 2012/01/20.

[223] 三石和貴、” ２次電池材料の電子顕微鏡観察”、第３回 AIST-NIMS 計測分析シンポジウム , 産業技術総合研究所 , つくば（日本）2011/12/09.

[224] 三石和貴 , 橋本綾子 , 竹口雅樹 , 下条雅幸 , 石塚和夫 ,“共焦点電子顕微鏡の深さ分解のメカニズム”, 第 7 回日本顕微鏡学会　超分解能電子顕微鏡分科会 , 名古屋市 , 2011/11/30.

[225] 藤田大介、野口秀典、三石和貴、橋本綾子、石田暢之、“グリーンイノベーションのためのナノスケール表界面計測”、NCCG-41 第 41 回結晶成長国内会議、つくば市 (日本)、2011/11/04.

国際会議（一般）

[226] M. Takeguchi, X. Zhang, A. Hashimoto, K. Mitsuishi, M. Shimojo, P. Wang, PD. Nellist and AI. Kirkland, Three Dimensional Observation of Mesoporous Silica-Hematite Hollow Spheres by Scanning Confocal Electron Microscopy, APMC10, Perth (Australia), 2012/02/05-2012/02/09.

[227] M. Takeguchi, M. Shimojo, L. Dan and K. Mitsuishi, “Development of sample-scanning electron holography”, Microscopy and Microanalysis 2011, Nashville (USA), 2011/08/07-2011/08/11.

[228] M. Tanaka, “In-situ Observation of Ni Clusters on Oxide Surfaces by UHV-TEM/STM”, 6th International Symposium on Surface Science, Tokyo (Japan), 2011/12/11-2011/12/15.

[229] A. Hashimoto, “High Temperature Observation of Pt nanoparticles on Graphene Layers by Aberration Corrected Transmission Electron Microscopy “, APMC10, Perth (Australia), 2012/02/05-2012/02/09.

[230] S. J. Ye, M. Song, A. Matsumoto, K. Togano, M. Takeguchi, H. Kumakura, R. Teranishi, T. Kiyoshi, “Comparison of SiC and/or toluene additives to the critical current density of internal Mg diffusion-processed MgB2 wires”, 24th International Symposium on Superconductivity (ISS2011), FUNABORI,Tokyo, 日本 (Japan), 2011/10/24-2011/10/26.

国内学協会会議（一般）

[231] 木本浩司、“Spatially-resolved diffractometry による原子コラムの観察 ” 顕微鏡学会第 67 回学術講演会、福岡市 (日本)、2011/05/16-2011/05/18.

[232] 木本浩司、“モノクロメーターを備えた高分解能電子顕微鏡の空間分解能 ” 顕微鏡学会第 67 回学術講演会、福岡市 (日本)、2011/05/16-2011/05/18.

[233] 竹口雅樹、三石和貴、Lei Dan、下条雅幸、“試料走査電子線ホログラフィーの開発”顕微鏡学会第 67 回学術講演会、福岡市 (日本)、2011/05/16-2011/05/18.

[234] 竹口雅樹、神谷博道、小粥啓子、“コンパクトな電子線バイプリズムの開発”顕微鏡学会第 67 回学術講演会、福岡市 (日本)、2011/05/16-2011/05/18.

[235] 石川信博、板垣孟彦、長井寿、高橋克則、“藻場育成のためのスラグ浚渫土混合材固化メカニズムの解析” 日本鉄鋼協会第 162 回講演大会、大阪市 (日本)、2011/9/20-2011/9/22.

[236] 石川信博、荻原俊弥、竹口雅樹、渡部秀人、稲見隆、“SiO2 含有 FeO ウスタイトの溶融温度域での挙動 TEM 内その場観察” 日本金属学会第 149 回講演大会、宜野湾市 (日本)、2011/11/7-2011/11/9.

[237] 三石和貴、大西剛、高田和典、橋本綾子、竹口雅樹、藤田大介、奈良純、大野隆央“(111) 配向した La0.55 Li0.33TiO3 膜中の板状欠陥の高分解能 STEM 観察”日本顕微鏡学会第 67 回学術講演会、福岡市 (日本)、2011/05/16-2011/05/18.

[238] 田中美代子、“SrTiO3 上金属クラスター／薄膜の観察” 顕微鏡学会第 67 回学術講演会、福岡市 (日本)、2011/05/16-2011/05/18.

[239] 田中美代子、”UHV-TEM/STM による SrTiO3 上 Ni クラスターのその場観察” 2012 年春季第 59 回応用物理学関係連合講演会、新宿区（日本）、2012/03/15-2012/03-18.

[240] 橋 本 綾 子、“Control of observation environments in a transmission electron microscope by specimen holders”、第 3 回 ナノ材料科学環境拠点シンポジウム 、つくば市 (日本)、2012/02/27.

[241] 橋本綾子、XINGJuanJuan、竹口雅樹、“光照射 TEM 試料ホルダーの開発とその応用 / 光照射 TEM 試料ホルダーの開発とその応用”、NIMS 先端計測シンポジウム 2012 、つくば市 (日本)、2012/02/23.

[242] 橋本綾子、三石和貴、竹口雅樹、“光触媒材料観察ための試料ホルダーシステムの開発”、日本顕微鏡学会第 6 7回学術講演会 、福岡市 (日本)、2011/05/16 - 2011/05/18.

[243] 橋本綾子、“光機能材料観察に向けた透過型電子顕微鏡試料ホルダーの開発”、第 18 回シンポジウム「光触媒反応の最近の展開」、東京 (日本)、2011/12/12.

[244] 三石和貴、大西剛、高田和典、橋本綾子、藤田大介、竹口雅樹、大野隆央、奈良純、“(111) 配向した La0.55 Li0.33TiO3 膜中の板状欠陥の高分解能 STEM 観察”、日本顕微鏡学会 67 回学術講演会 、福岡市 (日本)、2011/05/16 - 2011/05/18.

[245] Xiaobin Zhang、竹口雅樹、橋本綾子、三石和貴、手塚 還、下条雅幸、“Effects of pinhole size and chromatic aberration on the depth”、日本顕微鏡学会第 67 回学術講演会 、福岡市 (日本)、2011/05/16 - 2011/05/18.

[246] M. Song, S. J. Ye, M. Takeguchi, M. Shimojo, K. Furuya, A. Matsumoto, K. Togano, H. Kumakura, “3 Dimensional-STEM of dispersed nano structures in materials”, 日本顕微鏡学会第 67 回学術講演会発表要旨集、福岡市 (日本)、2011/05/16-2011/05/18.

[247] 大吉啓司 , 長谷川明 , “アルミナ微粒子への低温電子線照射によるγ相から Re2O3(II) 型高圧相への相変態”, 2011 年春季第 58 回応用物理学関係連合講演会、厚木市 (日本)、2011/03/24 - 2011/03/27.

■強磁場固体ＮＭＲ計測技術の開発と先進材料応用

国内学協会会議（招待・依頼）

[248] 清水禎, “1GHz 級 NMR 磁石の大震災からの復旧状況（930MH ｚ磁石の場合）”, 2011 年度秋季低温工学・超電導学会, 金沢市,（12/9-12/11）

国際会議（一般）

[249] Mutsuo Igarashi, Takehito Nakano, Atsushi Goto, Kenjiro Hashi,Tadashi Shimizu, Atsufumi Hanazawa and Yasuo Nozue,"NMR Property of Rubidium Loaded Sodalite", 16th International Symposium on Intercalation Compounds, (Sec-Ustupky, Czech Republic, 2011/05/22-2011/05/27

[250] M Ando, I Oikawa, Y Noda, OHKI Shinobu, TANSHO Masataka, SHIMIZU Tadashi, H Kiyono, H Maekawa, “High field O-17 NMR study of defects in doped zirconia and ceria”, 17th International Conference on Solid State Ionics, Tronto,Canada, 2009/06/28 - 2009/07/03

[251] IGARASHI Mutsuo, 中野岳仁 , 清水禎 , 後藤敦 , 端健二郎 , 大木忍 , ファム・タン・ティ , 野 末 泰 夫 , “Relaxation Property of NMR in Low-Silica X Zeolite Heavily Loaded with Sodium”, Inter.Conf. of New Science Created by Materials with Nano Spaces, 仙 台 市 , 2011/11/24 - 2011/11/26

[252] 品川秀行 , 大木忍 , 藤戸輝昭 , 清水禎 , “Development of Leak-Tight MAS Rotor for Liquid Samples”, The 52nd ENC, Pacific Grove, California,USA, 2011/04/10 - 2011/04/15

国内学協会会議（一般）

[253] 五十嵐睦夫、中野岳仁、後藤 敦、端健二郎、清水禎、伊藤正行、水金貴裕、ファム・タン・ティ、野末泰夫 “ナトリウムを飽和吸蔵した LSX 型ゼオライトの高温 NMR 特性”, 日本物理学会 2011 年秋季大会（富山大学）(2011 年 9 月 21 日～ 24 日)

[254] 後藤 敦 ,”光ポンピング法を偏極源とした固体超偏極技術の開発”JST さきがけ物質と光作用」公開シンポジウム , アキバホール、東京、(2011 年 12 月 15 日～ 16 日)

[255] 大橋竜太郎 , 熊谷翼秀 , 水野元博 , 瀬川浩代 , 丹所正孝 , 清水禎 , ” 固体ＮＭＲによるハイブリドチタニアフィルムの解析”, 固体 NMR･材料フォーラム , 京都平安ホテル , 京都市 , (2011 年 10 月 25 日）

[256] 五十嵐睦夫 , 中野岳仁 , 後藤敦 , 端健二郎 , 清水禎 , 大木忍 , 伊藤正行 , 水金貴裕 , ファム・タン・ティ , 野末泰夫 , “ナトリウムを飽和吸蔵した LSX 型ゼオライトの高温 NMR 特性” 日本物理学会 2011 年秋季大会 , 富山大学五福キャンパス , 富山市 , 2011 年 9 月 21 日～ 2011 年 9 月 24 日

[257] 橋本康博 , 名雪三依 , 松井久仁雄 , 清水禎 , “ トバモライト生成への Al3+ の影響 : 高磁場 NMR による Al 置換位置の特定”, セメント技術大会 , ホテルメトロポリタン , 東京 , 2011 年 5 月 18 日～ 2011 年 5 月 20 日

[258] 後藤和馬 , 武田和行 , Lerner M. Michael, 後藤敦 , 丹所正孝 , 端健二郎 , 大木忍 , 清水禎 , 丸山晋平 , 石田祐之 , “19F NMR によるフッ化分子導入黒鉛層間化合物の状態分析”, 日本化学会第 91 春季年会 , 神奈川大学 , 横浜市 , 2011/03/26 ～ 2011/03/29

[259] 後藤敦 , 大木忍 , 端健二郎 , 清水禎 , 瀧澤智恵子 , 加藤誠一 , 北澤英明 , “光ポンピング法を偏極源とした固体超偏極技術の開発”, 日本物理学会第 66 回年次大会 , 新潟大学 , 新潟市 , 2011 年 03 月 25 日～ 2011 年 03 月 28 日

■強力中性子線計測技術の開発と先進材料応用

国際会議（招待）

[260] M. Ohnuma, “Combined Use of Small-Angle X-Ray and Neutron Scattering: SAS in Color”, TMS2012(アメリカ材料系３学会１４１回年会)、合衆国（オーランド）, 2012/3/11-15

[261] M. Ohnuma, "Microstructure and Magnetic Anisotropy in Amorphous and Nanocrystalline Materials",56th Annual Conference on Magnetism & Magnetic Materials (American Institute of Physics) , アメリカ合衆国（フェニックス）, 2011/10/30~11/3

[262] M. Ohnum,” Combined Use of Small-Angle X-ray and Neutron Scattering”, The 7th International Symposium on the Characterization of Metal , 韓 国 金 属 学 会 (大 田), 2011/09/26 -9/27

[263] M. Ohnuma, “Residual strain of the amorphous softmagnetic ribbons with creep induced anisotropy”, Thermec' 2011、カナダ（ケベック）, 2011/08/01-08/05

[264] M. Nishino, "Macroscopic nucleation and scale free phenomena in long-range elastic interaction systems", International Workshop on Studies on Phase Transitions, Tokyo Univ. Yayoi Auditorium, 2011/06/09

[265] H. Mamiya, B. Jeyadevan, "Numerical study on dissipative structures of magnetic nanoparticles in a large alternating magnetic field and targeted hyperthermia treatment"JT Conf. on Magnetic Nanoparticles for Biomedical Applications"（招待講演）2011/11/12,Institute of Biomedical Engineering,(台中市 , 台湾)

国内学協会会議（招待・依頼）

[266] 北澤英明,“ナノ計測技術によるアルミナ系 ReRAM デバイス開発”, 第３回 AIST-NIMS 計測分析シンポジウム, 産業技術総合研究所, 2011/12/09 - 2011/12/09

[267] 北澤英明,”中性子散乱によるマルチスケール解析と環境・エネルギー関連材料への応用”, NIMS-AIST（NRI）計測・計算シミュレーション合同 WS, 産業技術総合研究所, 2011/10/25 - 2011/10/25

[268] 北澤英明,”中性子散乱によるマルチスケール解析と環境・エネルギー関連材料への応用”, 第８回先端計測オープンセミナー, 物質・材料研究機構, 2012/1/23.

[269] 北澤英明,”希土類カゴ状化合物の中性子散乱研究”, 三機関連携＆鉄系超伝導合同研究会「超伝導と磁性とフォノン」, KKR 箱根宮ノ, 2012/01/23 - 2012/01/24

[270] 北澤英明,“中性子散乱によるマルチスケール解析と環境・エネルギー関連材料への応用 “, NIMS 先端計測シンポジウム 2012, 物質・材料研究機構, 2012/2/23.

[271] 茂筑高士,“新規マンガン酸リチウム正極物質の結晶構造と電池特性”, 中性子産業利用推進協議会「電池材料研究会」, 研究社英語センタービル（東京都新宿区）,（2011.11.17）

国際会議（一般）

[272] H. Kitazawa, A. Doenni, Y. Tsuchiya, N. Terada, Y. Kawamura, H. Suzuki, O. Sakai, M Matsuda, K.Kakurai, G. Ano, M. Akatsu, Y. Nemoto, T.Goto,“Inelastic Neutron Scattering and High-field Magnetization Studies of the Clathrate Compound Ce3Pd20Si6”, 5th European Conference on Neutron Scattering, Prague, 2011/07/17 - 2011/07/22

[273] H. Kitazawa, Y. Kawamura, K. Momma, S. Kato, N. Tsujii, T. Mochku, A. Doenni, J. Prchal, J. Zhang, S. Torii, M. Yonemur, T. Kamiyama,“The isostructural phase transition in TbPd1-xNixAl and TbNi1-yCuyAl studied by high-resolution powder neutron diffraction”, 1st Asia-Oceania Conference on Neutron Scattering 2011, Tsukuba, 2011/11/21 - 2011/11/24

[274] M. Hase, V. Yu. Pomjakushin, V. Sikolenko, L. Keller, A. Dönni, and H. Kitazawa,“Negative magnetization of Li2Ni2Mo3O12 including two spin subsystems, distorted honeycomb lattice and linear chain”, The 26th International Conference on Low Temperature Physics (LT26), Beijing, China, August 10 – 17, 2011.

[275] T. Hosaka, S. Hachiuma, H. Kuroe, T. Sekine, M. Hase, K. Oka, T. Ito, H. Eisaki, M. Fujisawa, S. Okubo, and H. Ohta,“Magnetic and Electric Properties in the Distorted Tetrahedral Spin Chain System Cu3Mo2O9”, The 26th International Conference on Low Temperature Physics (LT26), Beijing, China, August 10 – 17, 2011.

[276] K. Misoka, K. Doi, T. Hamasaki, H. Kuroe, T. Goto, T. Sekine, T. Sasaki, M. Hase, K. Oka, T. Ito, and H. Eisaki,“Cu-NMR study on dimer-chain complex quantum spin system Cu3Mo2O9”, The 26th International Conference on Low Temperature Physics (LT26), Beijing, China, August 10 – 17, 2011.

[277] M. Ohnuma, Y. Oba, Kozikowski, Wakabayashi, Sasakawa, Nakayama, Ishikawa, "Wetting process of β-FeOOH with Ti by Small-angle neutron and X-ray scattering", 21st Academic Symposium of MRS-Japan 2011, 2011/12/19-21, 横浜情報文化センター

[278] H.Ohtsuka, H.Suzuki, Y.Kawamura, N.Terada, H.Kitazawa and N.Metoki"Effects of a high magnetic field on martensitic transformation and reverse transformation from martensite to austenite", International Conference on Martensitic Transformations (2011ICOMAT), Sept.4-9, 2011, Senri-Hankyu Hotel, Osaka, Japan.

[279] H.Ohtsuka, H.Suzuki, Y.Kawamura, N.Terada, H.Kitazawa and N.Metoki"Effects of a High Magnetic Field on Martensitic Transformation in an Fe-Ni-C Alloy" 1st Asia-Oceania Conference on Neutron Scattering, Nov.20-24, Tsukuba, Japan

[280] Y. Suzuki, P. Das, T. Mochiku, T. Kashiwagi, M. Tachiki, K. Kadowaki,“Crystal structure and superconducting properties in CuxBi2Se3”, March Meeting 2012, American Physics Society, Boston, USA (2012.2.27-2012.3.2)

[281] H.S. Suzuki, S. Takagi, D. Kubo, I. Watanabe, T. Suzuki, T. Matsuzaki,“μ SR study on cubic PrMg3 with orbital degrees of freedom in the crystal-field ground state”12th international conference on Muson Spin Rotation, Relaxation, Cancun, Mexico, (2011/5/16~20).

[282] H.S. Suzuki, N. Terada, K. Kaneko, N. Metoki, T. Osakabe, T. Onimaru, M. Amara, R.-M. Galera, L.-P. Regnalt,“Crystalline Electreic Field excitations in Pr compounds with non-Kramers doublet Γ3 ground state”1st Asia-Oceania Conference on Neutron Scattering , Tsukuba, Japan, (2011/11/20~24).

[283] H. Mamiya and S. Nimori,"Memory effects in spin glasses: Spontaneous restoration of the original spin configuration rather than preservation in a frozen state", The 56th Magnetism and Magnetic Materials Conference ,2011/11/1, The JW Marriott Desert Ridge, (Scottsdale, USA)

[284] H. Mamiya, N. Terada, H. Kitazawa, A. Hoshikawa, T. Ishigaki , "Structural and magnetic characterization of dilute spinel ferrites"1st Asia-Oceania Conference on Neutron Scattering, 2011/11/22, EPOCHAL TSUKUBA, (TSUKUBA, Ibaraki)

[285] 片桐昌彦 , 加藤誠一 , 浦島邦子 Structural Stability of AlH3 as Hydrogen Storage Materi 2nd ISNPEDADM - 2001 Institut de Recherche pour le Developpement (IRD),Noumea,New Caledonia 2011/11/14 - 2011/11/19

[286] 片桐昌彦 , 浦島邦子 , 加藤誠一 Hydrogenation of Aluminum by Anodic Coating for AlH3 Hydrogen Storage Material ICFEE 2012 Comittee Quality Hotel Singapore,Singapore,Singapore 2012/02/26 - 2012/02/28

[287] 原田善之 , 児子精祐 , 加藤誠一 , 北澤英明 , 木戸義勇 Direct electron beam lithographic method for fabrication of long range ordered anodic porous aluminum Intern. Symp. Advanced Nanodevice and Nanotechnology Sheraton Maui,Kaanapali,USA 2011/12/04 - 2011/12/09

[288] 原田善之 , 児子精祐 , 加藤誠一 , 北澤英明 , 木戸義勇 Low forming voltage ReRAM in Al/Al:Al2O3/Al Intern. Symp. Advanced Nanodevice and Nanotechnology Sheraton Maui,Kaanapali,USA 2011/12/04 - 2011/12/09

[289] N. Terada, T. Osakabe and H. Kitazawa,“Pressure effect on magnetic orderings in a frustrated magnet CuFeO2”European Conference on Neutron Scattering 2011 (ESNS2011) Prague, Czeck July 17-23 (presentation on 21st), 2011

国内学協会会議（一般）

[290] 北澤英明，A. Doenni，T. Strassle，L. Keller，松田雅昌，加倉井和久，阿野元貴，赤津光洋，根本祐一，後藤輝孝，”中性子非弾性散乱法によるカゴ状化合物 Pr3Pd20Si6 の結晶場準位の決定 II”，日本物理学会 2011 年秋季大会，富山大学 , 2011/09/21 - 2011/09/24.

[291] 阿野元貴，藤田雅也，三本啓輔，赤津光洋，根本祐一，後藤輝孝，小野宏基，武田直也，柳町治，A. Doenni，北澤英明，”希土類化合物 Ce3Pd20Si6 の近藤効果 II”，日本物理学会 2011 年秋季大会，富山大学 , 2011/09/21 - 2011/09/24.

[292] 小野宏基，中野智仁，武田直也，阿野元貴，赤津光洋，根本祐一，後藤輝孝，北澤英明 ,“単結晶 R3Pd20Si6 の磁場中比熱 III”，富山大学 , 2011/09/21 - 2011/09/24.

[293] 森田憲吾，細矢信吾，大貫喜徳，橋尾範，田巻明，鈴木博之，北澤英明，”Sm1-xLaxSn3 の弾性的性質 II”，富山大学 , 2011/09/21 - 2011/09/24.

[294] 北澤英明 , 河村幸彦 , 門馬綱一 , 加藤誠一, 辻井直人 , 茂筑高士, A. Doenni, L. Keller, J. Prchal, P. Javorsky, J. Zhang, 鳥居周輝, 米村雅雄 , 神山　崇, ”希土類３元系化合物 TbPd1-xNixAl の同相構造相転移”, 日本物理学会 2012 年年次大会, 関西学院大学, 2012/03/24 - 2012/03/27

[295] 森田憲吾, 細矢信吾, 豊泉沙織, 橋尾範, 田巻明, 鈴木博之, 北澤英明, ”Sm1-xLaxSn3 の異常な帯磁率と弾性定”, 日本物理学会 2012 年年次大会, 関西学院大学, 2012/03/24 - 2012/03/27

[296] 岩上欧史, 浪指悠平, 阿部聡, 松本宏一, 阿野元貴, 赤津光洋, 三本啓輔, 根本祐一, 後藤輝孝, 武田直也, 北澤英明, ”希土類カゴ状化合物 Pr3Pd20Ge6 の交流帯磁率測”, 日本物理学会 2012 年年次大会, 関西学院大学, 2012/03/24 - 2012/03/27

[297] 河村幸彦, 北澤英明, 寺田典樹, 間宮広明, 井川直樹, 目時直人, 金子耕士, Seongsu Lee, ”磁気冷凍材料 R5Pd2（R=Tb,Ho) の中性子回折実験”, 日本物理学会 2012 年年次大会, 関西学院大学, 2012/03/24 - 2012/03/27

[298] 小嶋健児, 宮崎正範, 平石雅俊, 幸田章宏, 門野良典, 土屋佳則, 鈴木博之, 北澤英明, ”μSR で見るスピネル (Cu,Zn)Ir2S4 超伝導体の超伝導特性”, 日本物理学会 2012 年年次大会, 関西学院大学, 2012/03/24 - 2012/03/27

[299] 鳴海康雄, 森岡貴之, 野尻浩之, 中村哲也, 広野等子, 木下豊彦, 寺田典樹, 北澤英明, 金道浩一, ”三角格子反強磁性体 CuFeO2 の軟Ｘ線磁気円二色性測定”, 日本物理学会 2012 年年次大会, 関西学院大学, 2012/03/24 - 2012/03/27

[300] 北澤英明 , 河村幸彦 , 門馬綱一 , 加藤誠一, 辻井直人 , 茂筑高士, A. Doenni, L. Keller, J. Prchal, P. Javorsky, J. Zhang, 鳥居周輝, 米村雅雄 , 神山　崇, “希土類３元系化合物 TbPd1-xNixAl の同相構造相転移 “、第３回 MLF シンポジウム, いばらき量子ビーム研究センター, 2012/01/19 - 2012/01/20

[301] 北澤英明, 河村幸彦, 寺田典樹, 間宮広明, 鈴木博之, A. Doenni, 目時直人, 金子耕士, 井川直樹, ”巨大磁気冷凍材料の中性子回折による研究”, NIMS 先端計測シンポジウム 2012, 物質・材料研究機構, 2012/2/23

[302] 北澤英明, 児子精祐, 原田善之, 加藤誠一, 中野嘉博, 大吉啓司, 柳町治, 井上純一, 木戸義勇, ”AlOx-ReRAM 素子開発の現状”, 2011 年秋季 第７２回応用物理学会学術講演会 , 山形大学, 2011/08/29 - 2011/09/02

[303] 加藤誠一, 児子精祐, 原田善之, 北澤英明, 木戸義勇, ”陽電子消滅法によるアルミ陽極酸化膜のナノ空孔測定”, 2011 年秋季 第７２回応用物理学会学術講演会 , 山形大学, 2011/08/29 - 2011/09/02

[304] 岡邦彦, 伊藤利充, 永崎洋, 長谷正司, 浜崎智彰, 黒江晴彦, 関根智幸、”連続固相反応法による Cu3Mo2O9 単結晶育成”、第 41 回結晶成長国内会議(NCCG-41)、日本結晶成長学会、つくば国際会議場、2011 年 11/3 木－ 5 土

[305] 長谷正司, Vladimir Yu. Pomjakushin, Vadim Sikolenko, Lukas Keller, Andreas Doenni, 北澤英明、”絶縁体 Li2Ni2Mo3O12 の負の磁化”、2011 年秋季大会、富山大学、2011 年 9/21 水－ 24 土

[306] 黒江晴彦, 保坂朋宏, 八馬傑, 関根智幸, 赤木暢, 桑原英樹, 長谷正司, 岡邦彦, 伊藤利充, 永崎洋、”擬一次元反強磁性体 Cu3Mo2O9 の電気的性質 II”、2011 年秋季大会、富山大学、2011 年 9/21 水－ 24 土

[307] 八馬傑, 保坂朋宏, 木野亮, 黒江晴彦, 関根智幸, 長谷正司, 岡邦彦, 伊藤利充, 永崎洋、”擬一次元反強磁性体 Cu3Mo2O9 の磁場中誘電率 III”、2011 年秋季大会、富山大学、2011 年 9/21 水－ 24 土

[308] 新聡一郎, 後藤貴行, 長谷正司, ”ネマチック状態が期待される一次元競合系 Rb2Cu2Mo3O12 における 87Rb-NMR”、2011 年秋季大会、富山大学、2011 年 9/21 水－ 24 土晦日慶太, 土井憲一, 浜崎智彰, 黒江晴彦, 後藤貴行, 関根智幸, 佐々木孝彦, 長谷

正司，岡邦彦，伊藤利充，永崎洋、”一次元鎖とダイマーからなる磁性 Cu3Mo2O9 の Cu-NMR III”、2011 年秋季大会、富山大学、2011 年 9/21 水－ 24 土

[309] 八馬傑，保坂朋宏，伊藤龍亮，長谷川卓哉，黒江晴彦，赤木暢，桑原英樹，関根智幸，長谷正司，岡邦彦，伊藤利充，永崎洋、”マルチフェロイック物質 (CuZn)3Mo2O9 の磁場 - 温度相図”、第 67 回年次大会（2012 年）、関西学院大学、2012 年 3/24 土－ 27 火

[310] 保坂朋宏，伊藤龍亮，長谷川卓哉，八馬傑，黒江晴彦，関根智幸，長谷正司，岡邦彦，伊藤利充，永崎洋、”マルチフェロイック物質 (CuZn)3Mo2O9 の磁化の組成依存性”、第 67 回年次大会（2012 年）、関西学院大学、2012 年 3/24 土－ 27 火

[311] 長谷川卓哉 , 保坂朋宏 , 伊藤龍亮 , 八馬傑 , 黒江晴彦 , 関根智幸 , 木原工 , 徳永将史 , 長谷正司 , 岡邦彦 , 伊藤利充 , 永崎洋 , 松本正茂、”マルチフェロイック物質 Cu3Mo2O9 の強磁場磁化・分極測定”、第 67 回年次大会（2012 年）、関西学院大学、2012 年 3/24 土－ 27 火

[312] 伊藤龍亮，保坂朋宏，長谷川卓哉，八馬傑，黒江晴彦，関根智幸，長谷正司，岡邦彦，伊藤利充, 永崎洋、”マルチフェロイック物質 Cu3Mo2O9 の交差相関”、第 67 回年次大会(2012 年)、関西学院大学、2012 年 3/24 土－ 27 火

[313] 新聡一郎，後藤貴行，長谷正司、”ネマチック状態が期待される一次元競合系 Rb2Cu2Mo3O12 における 87Rb-NMR II”、第 67 回年次大会（2012 年）、関西学院大学、2012 年 3/24 土－ 27 火

[314] 星野侑宏，新聡一郎，後藤貴行，長谷正司，佐々木孝彦、”ネマチック状態が期待される一次元競合系 Cs2Cu2Mo3O12 における 133Cs-NMR”、第 67 回年次大会（2012 年）、関西学院大学、2012 年 3/24 土－ 27 火

[315] 新聡一郎，後藤貴行，長谷正司、”CuO2 リボン鎖を持つ 1 次元競合系 Rb2Cu2Mo3O12 における 87Rb-NMR”、第 67 回年次大会（2012 年）、関西学院大学、2012 年 3/24 土－ 27 火

[316] 晦日慶太，土井憲一，浜崎智彰，黒江晴彦，後藤貴行，関根智幸，佐々木孝彦，長谷正司，岡邦彦，伊藤利充，永崎洋、”一次元鎖とダイマーからなる磁性 Cu3Mo2O9 の Cu-NMR IV”、第 67 回年次大会（2012 年）、関西学院大学、2012 年 3/24 土－ 27 火

[317] 大塚秀幸 , 鉄系合金における固相 / 固相変態変態挙動と組織に及ぼす強磁場効果日本鉄鋼協会第 162 回秋季講演大会　大阪大学　吹田キャンパス

[318] 大塚秀幸、鈴木博之、北澤英明 , Fe-Ni-C 合金におけるマルテンサイト変態に及ぼす強磁場の影響 , NIMS 先端計測シンポジウム 2012, 物質・材料研究機構

[319] 茂筑高士, 畑慶明, 星川晃範, 岩瀬謙二, Dyah Sulistyanintyas, 小黒英俊, 石垣徹, 土屋佳則, 安岡宏，平田和人“FeSr2YCu2O6+ ▪ 系における欠損・超伝導・磁性”，日本セラミックス協会第 24 回秋季シンポジウム，北海道大学,（2011.9.7-2011.9.9）

[320] 茂筑高士，畑慶明，松下能孝，勝矢良雄，星川晃範，岩瀬謙二，Dyah Sulistyanintyas，小黒英俊，石垣徹，土屋佳則，岩井秀夫，安岡宏，平田和人“FeSr2YCu2O6+ ▪ 磁性超伝導体の規則･不規則構造”，日本物理学会 2011 年秋季大会，富山大学,（2011.9.21-2011.9.24）

[321] 茂筑高士，畑慶明，土屋佳則，星川晃範，岩瀬謙二，Dyah Sulistyanintyas，小黒英俊，石垣徹，安岡宏，平田和人“FeSr2YCu2O6+ ▪ における磁化と構造的な乱れ”，日本物理学会 2011 年秋季大会，関西学院大学,（2012.3.24-2011.9.27）

[322] 鈴木博之、寺田典樹、鬼丸孝博、金子耕士,“非磁性 2 重項基底状態Γ 3 をとる Pr 化合物における結晶場励起”, 日本物理学会 2011 年秋季大会, 富山大学,（2011 年 9 月 21 日～ 24 日）

[323] 鈴木博之、高木滋、久野大輔、鈴木栄男、渡邊功雄、松崎禎市郎、H. Luetkens, C. Baines, A. Amato,“Non-Kramers 二重項Γ 3 基底立方晶 Pr 化合物のμ SR”，日本物理学会第 67 回年次大会、関西学院大学（2012 年 3 月 24 日～ 27 日）

[324] 西野正理, 宮下精二, C. Enachescu(Alexandru Ioan Cuza大), K. Boukheddaden(Versailles大), F. Varret (Versailles 大) " スピンクロスオーバーモデルにおける 長距離的弾性相互作用がもたらすスケールフリーな緩和現象 " 2011 日本物理学会秋季大会 富山大 2011/09/21

[325] 西野正理 , 宮下精二 , 中田 太郎 , 藤堂眞治 , " 格子変形を伴う双安定状態間相転移シミュレーションの開発と応用 " 文科省次世代スーパーコンピュータプロジェクト 次世代ナノ統合シミュレーションソフトウェアの研究開発 学士会館 2012/01/26

[326] 西野正理 , 中田 太郎 , 遠藤 祐介, 宮下精二 , " スピンクロスオーバー系におけるスピンと格子自由度の時間スケールの相違により発現する緩和ダイナミクス ", 日本物理学会年次大会 関西学院大 2012/03/24

[327] 間宮広明 , 二森茂樹 , " ハイゼンベルグスピングラスにおけるスピン配列の再生現象 " 日本物理学会 2012 年年次大会 ,2012/3/24, 関西学院大学西宮上ケ原キャンパス (西宮市 , 兵庫県)

[328] 間宮広明 , バラチャンドラン ジャヤデワン " 磁性ナノ粒子の大振幅交流磁場応答と選択的癌温熱療法 " 平成 23 年度磁性流体連合講演会 ,2011/12/2, 滋賀県立大学 ,(彦根市 , 滋賀県)

[329] 間宮広明 , バラチャンドラン ジャヤデワン, " 回転の自由度にともなう磁性ナノ粒子の大振幅交番磁界応答の変化とそのハイパーサーミア最適条件への影響 " 第 35 回日本磁気学会学術講演会 ,2011/9/27, 新潟コンベンションセンター (新潟市 , 新潟県)

[330] 間宮広明 , バラチャンドラン ジャヤデワン " 大振幅交流磁場中で磁性ナノ粒子が形成する散逸構造と癌温熱療法 " 日本物理学会 2011 年秋季大会 ,2011/9/21," 富山大学五福キャンパス (富山市 , 富山県)

[331] 間宮広明 , バラチャンドラン ジャヤデワン," 強磁性体単磁区粒子の大振幅交流磁場応答と癌温熱療法への最適化 ", 日本物理学会第 66 回年次大会 2011 年 03 月 25 日 新潟大学五十嵐キャンパス , (新潟市 , 新潟県)

[332] 間宮広明 , 寺田典樹 , 北澤英明 , 石垣 徹 ," 資源環境調和型室温磁気冷凍材料の構造解析と物性評価 ", J-PARC 物質・生命科学ディビジョンシンポジウム 2011 年 01 月 17 日 高エネルギー加速器研究機構 (つくば市 , 茨城県)

[333] 辻井直人、“YbPdSi の強磁性と重い電子状態の共存 “、 日本物理学会 2011 年秋季大会、富山大学、2011 年 9 月 21 日 -24 日

[334] 辻井直人、“YbPdSi の強磁性と重い電子状態の共存 II “、 日本物理学会 2012 年年次大会、関西学院大学、2012 年 3 月 24 日 -27 日

[335] 加藤誠一 , “陽極酸化皮膜によるアルミの水素吸蔵特性の向上”, NIMS 先端計測シンポジウム 2012 NIMS 2012/2/23

[336] 加藤誠一 , 大平俊行 , 児子精祐 , 原田善之 , 北澤英明 , 木戸義勇 , “陽極酸化アルミニウムの構造解析”, NIMS-AIST (NRI) 計測・計算シミュレーション合同 WS 2011/10/25.

[337] 原田善之 , 児子精祐 , 加藤誠一 , 中野嘉博 , 北澤英明 , 木戸義勇 , “Al2O3:Al-ReRAM デバイスの作製”, 第 59 回応用物理学関係連合講演会 , 早稲田大学 2012/03/15 - 2012/03/18

[338] 北澤英明 , 児子精祐 , 原田善之 , 李政祐 , 加藤誠一 , 中野嘉博 , 大吉啓司 , 籾田浩義 , 大野隆央 , 柳町治 , 井上純一 , 熊谷和博 , 関口隆史 , 木戸義勇 , “ナノ計測技術によるアルミナ系 ReRAM デバイス開発”, 第３回 AIST-NIMS 計測分析シンポジウム , 産業技術総合研究所 2011/12/09

[339] 児子精祐 , 原田善之 , 加藤誠一 , 柳町治 , 中野嘉博 , 北澤英明 , 木戸義勇 , “MIS 構造の AlOx-ReRAM”, 第 72 回応用物理学会学術講演会 , 山形大学 2011/08/29 - 2011/09/02

[340] 原田善之 , 大井暁彦 , 児子精祐 , 加藤誠一 , 北澤英明 , 生田目俊秀 , 木戸義勇 , “酸化アルミニウム系 ReRAM デバイスの作製２”, 第 72 回応用物理学会学術講演会 , 山形大学 2011/08/29 - 2011/09/02

[341] 原田善之 , 児子精祐 , 加藤誠一 , 中野嘉博 , 北澤英明 , 木戸義勇 , “Al:Al2O3-ReRAM デバイスの作製”, 第 72 回応用物理学会学術講演会 , 山形大学 2011/08/29 - 2011/09/02

[342] 原田善之 , 加藤誠一 , 児子精祐 , 木戸義勇 ,“化合物薄膜の作製と物性”, 岡山大学理学研究科池田研究室セミナー , 岡山大学 2011/07/27 - 2011/07/27

[343] 中島多朗 , 須能梓 , 満田節生 , 寺田典樹 , 木村尚次郎 , 金子耕士 , 山内宏樹,“フラストレートした磁性体 CuFeO2 のスピン･格子･電荷自由度が結合した基底状態におけるスピン波励起”, フラストレーション特定領域第7回トピカルミーティング「フラストレーションと スピン・電荷・軌道・格子自由度」 2011 年 7 月 1 日 東京大学

[344] 萩原政幸, 木村尚次郎 , 藤田崇仁、山口博則、寺田典樹, 金道浩一 ,“三角格子反強磁性体 CuFeO2 の交換相互作用の磁場中変化”, フラストレーション特定領域第7回トピカルミーティング「フラストレーションと スピン・電荷・軌道・格子自由度」 2011 年 7 月 1 日 東京大学

[345] 玉造博夢, 青木優, 中村佑希, 満田節生, 中島多朗, 竹端寛治, 高増正, 寺田典樹, 北澤英明“マルチフェロイック CuFeO2 の強誘電相における磁場掃引による分極誘起”, 2012 年日本物理学会年会（関西学院大学）

[346] 中村真一, 不破章雄, 寺田典樹、”マルチフェロイック酸化物 CuFeO2 系のメスバウアー分光” 2012 年日本物理学会年会（関西学院大学）

[347] 木村尚次郎, 渡邊和雄, 藤田崇仁, 萩原政幸, 山口博則, 柏木隆成, 寺田典樹、”三角格子反強磁性 CuFeO2 の電場励起マグノン II”, 2012 年日本物理学会年会（関西学院大学）

[348] 金子周史, 中島多朗, 満田節生, 吉冨啓祐, 寺田典樹, 脇本秀一, 武田全康, 加倉井和久, 田中良和 ,“3 次元中性子偏極解析及び共鳴 X 線散乱を用いたマルチフェロイック CuFe1-xGaxO2 のらせん磁気相における磁気･結晶構造の精密探査”,2012 年日本物理学会年会（関西学院大学）

[349] 中島多朗, 満田節生, Jason T. Haraldsen, Randy S. FishmanB, Tao Hong, Jamie A. Fernandez-Baca, 寺田典樹, 上床美也、”マルチフェロイック CuFe1-xGaxO2 の一軸圧力を用いて実現した磁気的単ドメイン状態における磁気励起”, 2012 年日本物理学会年会（関西学院大学）

[350] 木村尚次郎, 渡邊和雄, 藤田崇仁, 萩原政幸, 山口博則, 柏木隆成, 寺田典樹 ,“三角格子反強磁性体 CuFeO2 の電場励起マグノン”, 2011 年日本物理学会秋季大会（富山大学）

■放射光を利用した先進計測技術の開発と先進材料応用

国際会議（招待）

[351] Kenji Sakurai, "Time-resolved X-ray analysis -To see how samples change in real time", IUPAC international congress on analytical sciences (ICAS 2011), Kyoto(京都国際会議場)、2011.5 22 ～ 5.26

国内学協会会議（招待・依頼）

[352] 桜井健次、サマリートーク : X線･放射光による埋もれた界面の構造計測の今後の課題と展望、「X線・放射光による埋もれた界面の構造計測」 シンポジウム（中止になった3月の応用物理学会シンポジウムを期日場所を変更して開催）、物質・材料研究機構千現地区、2011.7.25

[353] Vallerie Ann Innis Samson, 水沢まり、桜井健次、Neutron and X-ray reflection tomography: new and complementary tools for surface and interface imaging of thin films and multilayer materials, 第５９回応用物理学関係連合講演会、早稲田大学、2012.3.15 ～ 3.18

国際会議（一般）

[354] Vallerie Ann Innis Samson, Mari Mizusawa and Kenji Sakurai, X-RAY REFLECTION TOMOGRAPHY: FIRST RESULTS ON SURFACE IMAGING, 60th Annual Conference on X-Ray Analysis (Denver X-Ray Conference DXC 2011), Colorado Springs, USA, 2011.8.1~5

[355] Vallerie Ann Innis Samson and Kenji Sakurai, Surface Property and X-ray Reflectivity Evaluation of the Hydrophobic Switching Nature of Methylcellulose Ultra-Thin Films: Effects of Annealing and Swelling Gordon-Kenan Research Seminar, Colby College, Waterville, USA, 2011.8.6 ～ 7

[356] David Behal, Yangping Zhang, Mari Mizusawa, Hiroyuki Takeya and Kenji Sakurai, Phase transformation of cerium-aluminum intermetallic compounds during high-energy ball milling, International Conference on Martensitic Transformations (ICOMAT), Osaka(千里阪急ホテル), 2011.9.4 ～ 9.9

[357] Mari Mizusawa, Vallerie Ann Innis Samson and Kenji Sakurai, Visualization in neutron reflectivity, 1st Asia-Oceania Conference on Neutron Scattering, Tsukuba（エポカルつくば）, 2011.11.20 ～ 24

国内学協会会議（一般）

[358] Vallerie Ann Innis Samson, 桜井健次、Hydrophobic switch property of methylcellulose thin films: Influence of film thickness and thermal stresses, 第63回コロイドおよび界面化学討論会、京都大学、2011.9.7 ～ 9

[359] 桜井健次、水沢まり、短パルスX線を用いた時間分解蛍光 X 線スペクトル測定法の検討、日本分析化学会第 60 年会、名古屋大学、2011.9.14 ～ 16

[360] 桜井健次、水沢まり、化学組成・結晶構造の迅速イメージング　ー新しいX線顕微鏡、日本原子力学会２０１１秋の年会、北九州国際会議場、2011.9.19 ～ 22

[361] Vallerie Ann Innis Samson, 水沢まり、桜井健次、Visualization of surface and interfaces in multilayered thin films (1) First experimental results、第４７回Ｘ線分析討論会、九州大学、2011.10.28 ～ 29

[362] Vallerie Ann Innis Samson, 水沢まり、桜井健次、Visualization of surface and interfaces in multilayered thin films (2) Model calculations、第４７回Ｘ線分析討論会、九州大学、2011.10.28 ～ 29

[363] 水沢まり、桜井健次、クイック X 線反射率測定によるポリビニル酢酸薄膜のガラス転移の観察、第５９回応用物理学関係連合講演会、早稲田大学、2012.3.15 ～ 3.18

3. プレス発表

■先端表面敏感計測技術の開発と先進材料応用

[1] A. Bandyopadhyay「有機分子層における脳のようなコンピューティング」(2010.4.26)

■先端表層領域計測技術の開発と先進材料応用

[2] 化学工業日報「固体 NMR で相関性実証（触媒中の分子運動性）」(2010.9.17)

■強力中性子線計測技術の開発と先進材料応用

[3] 西野正理　他、日刊工業新聞「物質の核生成に新理論」(2012.3.5)

[4] 間宮広明　他、中日新聞　「がん温熱治療に光明　ナノサイズ磁力動き解明」2011年11月16日(朝刊）掲載、日刊工業新聞　「ナノ磁石の動きを予測　がん温熱療法　実用化後押し」2011年11月16日（27面）掲載

４．特許

■先端表面敏感計測技術の開発と先進材料応用

[1] A. Bandyopadhyay, S. Satyajit, D. Fujita," アレイ状のキャパシタで構成されるインダクタ（An inductor composed of arrayed capacitors）" 2010-096217-JP

[2] 藤田大介、大西桂子、長村俊彦「超高真空走査型プローブ顕微鏡」特許第 4431733 号、2010 年 1 月 8 日登録

[3] 五十嵐真一、中村 (板倉) 明子「高分子膜の体積膨張に伴うストレス変化を利用した湿度センサー」 特許第 4665144 号、平成 23 年 1 月 21 日登録

■先端表層領域計測技術の開発と先進材料応用

[4] 特許登録　第 4831604 号 (平成 23 年 9 月 30 日登録)　帯電中和電子の斜め照射法を用いた絶縁物試料観察用放射電子顕微鏡、安福秀幸，吉川英樹

[5] 特許登録　第 4900660 号 (平成 24 年 1 月 13 日登録)　X 線集束素子及び X 線照射装置，中澤弘基，吉川英樹，ブライクアウレルミハイ，駒谷慎太郎，大澤澄人，大堀謙一

■超先端電子顕微鏡技術の開発と先進材料応用

[6]「固体粒子充填方法」、下条雅幸、チューフーミン、田中美代子、古屋一夫、登録日:2011 年 4 月 8 日、特許登録第 4714829 号.

[7]「低エネルギーイオン照射による導電体物質からの特性X線発生方法とその装置」長谷川明、三石和貴、古屋一夫、登録日 : 2011 年 5 月 13 日、特許登録第 4735805 号

■強力中性子線計測技術の開発と先進材料応用

[8] 吉井賢資、水木純一郎、阿部英樹、北澤英明、「超伝導ホウ素化合物 MgB2 薄膜の作成方法」(特許第 4792597 号)、登録日 : 平成 23 年 8 月 5 日

[9] 原田善之、加藤誠一、北澤英明、木戸義勇、「アルミナ抵抗変化型メモリ素子及びその製造方法」、特許出願 2011-228511、出願日 : 2011 年 10 月 18 日

[10] 原田善之、加藤誠一、北澤英明、木戸義勇、「アルミニウム酸化物層を抵抗変化層に用いた抵抗変化型メモリ素子」、特許出願 2012-66523、出願日 : 2012 年 3 月 23 日

■強磁場固体ＮＭＲ計測技術の開発と先進材料応用

[11] 特願 2008-069261（2008.3.18 出願）磁気フィルター、品川秀行　特許　第 4831493 号

[12] 特願 2008-069279（2008.3.18 出願）磁気フィルター、品川秀行　特許　第 4831494 号

[13] 特願 2008-069287（2008.3.18 出願）磁気フィルター、品川秀行　特許　第 4831495 号

[14] 特願 2008-069288（2008.3.18 出願）磁気フィルター、品川秀行　特許　第 4831496 号出願

[15] 特願 2011-521003（2011.7.5 出願）超伝導磁石用シミング装置、品川秀行 , 清水禎 , 大木忍

[16] 特願 2012-29281 NMR プローブ装置、品川秀行 , 清水禎 , 大木忍 , 根本貴宏 , 馬場栄次郎 , 樋岡克哉

[17] 特願 2012-074625　NMR プローブ装置、品川秀行 , 清水禎 , 大木忍

[18] 特願 2011-248829 (2011.11.14 出願)　極低温環境で作動する CCD カメラ、端健二郎、清水禎、野口隆志、大木忍

5. 主要論文別刷り

■先端表層領域計測技術の開発と先進材料応用

[19] H.Shinotsuka,　S.Tanuma, C, J. Powell, D.R. Penn, “Calculations of electron stopping powers for 41 elemental solids over the 50 eV to 30 keV range with the full Penn algorithm”, NUCLEAR INSTRUMENTS & METHODS IN PHYSICS RESEARCH SECTION B-BEAM INTERACTIONS WITH MATERIALS AND ATOMS,Vol.270（2011).

■超先端電子顕微鏡技術の開発と先進材料応用

[20] K. Mitsuishi, A. Hashimoto, M. Takeguchi, M. Shimojo and K. Ishizuka, Ultramicrosc. 112 (2012) 53-60.

■強磁場固体ＮＭＲ計測技術の開発と先進材料応用

[21] 後藤敦， 大木忍， 端健二郎， 清水禎，“Optical switching of nuclear spin-spin couplings in semiconductors”, NATURE COMMUNICATIONS , Vol.115, No.20,10284-10291,（2011）.

■強力中性子線計測技術の開発と先進材料応用

[22] H. Mamiya and B. Jeyadevan, "Hyperthermic effects of dissipative structures of magnetic nanoparticles in large alternating magnetic fields", Scientific Reports Vol.1 (2011) 00157-1-7.

Nuclear Instruments and Methods in Physics Research B 270 (2012) 75–92

Contents lists available at SciVerse ScienceDirect

Nuclear Instruments and Methods in Physics Research B

journal homepage: www.elsevier.com/locate/nimb

Calculations of electron stopping powers for 41 elemental solids over the 50 eV to 30 keV range with the full Penn algorithm

H. Shinotsuka [a], S. Tanuma [a], C.J. Powell [b,*], D.R. Penn [b]

[a] National Institute for Materials Science, 1-2-1 Sengen, Tsukuba, Ibaraki 305-0047, Japan
[b] National Institute of Standards and Technology, Gaithersburg, MD 20899, USA

ARTICLE INFO

Article history:
Received 2 May 2011
Received in revised form 19 September 2011
Available online 1 October 2011

Keyword:
Electron stopping powers

ABSTRACT

We present mass collision electron stopping powers (SPs) for 41 elemental solids (Li, Be, graphite, diamond, glassy C, Na, Mg, Al, Si, K, Sc, Ti, V, Cr, Fe, Co, Ni, Cu, Ge, Y, Nb, Mo, Ru, Rh, Pd, Ag, In, Sn, Cs, Gd, Tb, Dy, Hf, Ta, W, Re, Os, Ir, Pt, Au, and Bi) that were calculated from experimental energy-loss-function data with the full Penn algorithm for electron energies between 50 eV and 30 keV. Improved sets of energy-loss functions were used for 19 solids. Comparisons were made of these SPs with SPs calculated with the single-pole approximation, previous SP calculations, and experimental SPs. Generally satisfactory agreement was found with SPs from the single-pole approximation for energies above 100 eV, with other calculated SPs, and with measured SPs.

Published by Elsevier B.V.

1. Introduction

In previous papers [1,2], we reported calculations of collision electron stopping powers (SPs) over the 100 eV to 30 keV energy range in 41 elemental solids from their "optical" energy-loss functions (ELFs). These ELFs were obtained from experimental optical data representing the dependence of the inelastic-scattering probability on energy loss and the theoretical Lindhard dielectric function [3] to represent the dependence of the scattering probability on momentum transfer. SPs were calculated with Penn's algorithm that was originally developed for the calculation of electron inelastic mean free paths (IMFPs) [4]. Our SPs were determined using the single-pole approximation or so-called simple Penn algorithm (SPA) that was expected to be satisfactory for electron energies greater than about 100 eV [1,2]. We have extended this earlier work in two ways. First, we have calculated SPs with the full Penn algorithm (FPA) which should be valid for electron energies down to about 50 eV [5]. Second, we have adopted better sets of optical ELF data in recent IMFP calculations with the FPA for 19 of our 41 elemental solids [6], and we make use of the improved ELF data in the present work.

We report mass collision SPs calculated with the FPA for 41 elemental solids (Li, Be, graphite, diamond, glassy C, Na, Mg, Al, Si, K, Sc, Ti, V, Cr, Fe, Co, Ni, Cu, Ge, Y, Nb, Mo, Ru, Rh, Pd, Ag, In, Sn, Cs, Gd, Tb, Dy, Hf, Ta, W, Re, Os, Ir, Pt, Au, and Bi) over the 50 eV to 30 keV energy range with the same optical ELF data sets that were used in the IMFP calculations [6]. We give a brief description of our SP algorithm in the next section. The new SPs are presented in the following section where we compare SPs from the new ELFs (and the FPA) to SPs from the old ELFs (and the SPA) and compare SPs from the FPA to SPs from the SPA. We then make comparisons of our new SPs with values from previous SP calculations and measurements.

We note that the collision electron SP is an important parameter in radiation dosimetry [7] and in the modeling of electron transport in matter for many other applications. The SP has been used in Monte Carlo simulations of electron transport relevant to electron-probe microanalysis [8–10], Auger-electron spectroscopy [11,12], and dimensional metrology in the scanning electron microscope [13]. The Bethe SP equation [14–16] has been used extensively as a predictive tool for energies where it is expected to be valid (i.e., at energies much larger than the largest K-shell binding energy in the material of interest), but there is a scarcity of SP data at lower energies, typically less than 10 keV. SPs calculated from the Bethe equation are available from a National Institute of Standards and Technology (NIST) database [17] and ICRU Report 37 for electron energies of 10 keV and above [7]. It is thus important to have SPs available for lower energies in order to describe electron-solid interactions for a variety of applications.

2. Calculation of electron stopping powers with the full Penn algorithm

Penn developed an algorithm for the calculation of electron IMFPs from a model dielectric function $\varepsilon(q,\omega)$, a function of momentum transfer q and energy loss $\hbar\omega$ [4]. The energy dependence of the energy-loss function (ELF), $\mathrm{Im}[-1/\varepsilon(q,\omega)]$, can

* Corresponding author.
E-mail address: cedric.powell@nist.gov (C.J. Powell).

0168-583X/$ - see front matter Published by Elsevier B.V.
doi:10.1016/j.nimb.2011.09.016

be obtained from experimental optical data for the material of interest and the dependence of the ELF on q can be obtained from the Lindhard model dielectric function [3]. IMFPs were determined from a triple integration (the FPA) for energies down to about 50 eV, while a simpler procedure involving a single integration (the SPA) was judged satisfactory for electron energies larger than about 200 eV [4–6]. We utilized the SPA in our previous SP calculations, but now use the FPA to extend the energy range down to 50 eV.

We give here a summary of our implementation of the full Penn algorithm for SP calculations. We will use Hartree atomic units ($m_e = e = \hbar = 1$) where m_e is the electron rest mass, e is the elementary charge, and $\hbar$ is the reduced Planck constant.

The relativistic differential cross section (DCS) for inelastic scattering can be expressed as the sum of a longitudinal DCS and a transverse DCS [42]. For electron energies less than about 0.5 MeV, the transverse DCS can be neglected [18]. The relativistic inelastic DCS can then be written as [42]:

$$\frac{d^2\sigma}{d\omega dQ} \approx \frac{d^2\sigma_L}{d\omega dQ} = \frac{1}{v^2}\frac{1+Q/c^2}{Q(1+Q/2c^2)}\frac{1}{\pi N}\mathrm{Im}\left(\frac{-1}{\varepsilon(Q,\omega)}\right), \tag{1}$$

where Q is the recoil energy given by $Q(Q+2c^2) = (cq)^2$ [19,42], v is the electron velocity, c is the speed of light, and N is the number of atoms or molecules per unit volume. The last factor in Eq. (1) is the ELF expressed here as a function of energy loss ω and recoil energy Q. The relativistic DCS in Eq. (1) can be conveniently written as a function of momentum transfer q:

$$\frac{d^2\sigma}{d\omega dq} \approx \frac{2}{\pi N v^2}\mathrm{Im}\left(\frac{-1}{\varepsilon(q,\omega)}\right)\frac{1}{q}. \tag{2}$$

Stopping powers can be calculated with the FPA from the probability $p(T,\omega)$ for energy loss ω per unit distance traveled by an electron with relativistic kinetic energy T. This probability can be calculated from Eq. (2):

$$\begin{aligned} p(T,\omega) &= \frac{2}{\pi v^2}\int_{q_-}^{q_+}\frac{dq}{q}\mathrm{Im}\left[\frac{-1}{\varepsilon(q,\omega)}\right] \\ &= \frac{(1+T/c^2)^2}{1+T/(2c^2)}\frac{1}{\pi T}\int_{q_-}^{q_+}\frac{dq}{q}\mathrm{Im}\left[\frac{-1}{\varepsilon(q,\omega)}\right], \end{aligned} \tag{3}$$

where $q_\pm = \sqrt{T(2+T/c^2)} \pm \sqrt{(T-\omega)(2+(T-\omega)/c^2)}$. The collision stopping power, S, can be calculated from the following equation [20]:

$$S = \int_0^{\omega_{\max}} \omega p(T,\omega)d\omega, \tag{4}$$

where $\omega_{\max} = T - E_f$ and E_f is the Fermi energy.

The ELF in the FPA can be expressed as:

$$\mathrm{Im}\left[\frac{-1}{\varepsilon(q,\omega)}\right] = \int_0^\infty d\omega_p g(\omega_p)\mathrm{Im}\left[\frac{-1}{\varepsilon^L(q,\omega;\omega_p)}\right], \tag{5a}$$

where ε^L denotes the Lindhard model dielectric function of the free electron gas with plasmon energy $\omega_p(=\sqrt{4\pi n})$, n is the electron density, $g(\omega_p)$ is a coefficient introduced to satisfy the condition $\mathrm{Im}[-1/\varepsilon(q=0,\omega)] = \mathrm{Im}[-1/\varepsilon(\omega)]$, and $\mathrm{Im}[-1/\varepsilon(\omega)]$ is the optical energy-loss function. The coefficient $g(\omega_p)$ is then given by

$$g(\omega) = \frac{2}{\pi\omega}\mathrm{Im}\left[\frac{-1}{\varepsilon(\omega)}\right]. \tag{5b}$$

The Lindhard ELF, $\varepsilon^L = \varepsilon_1^L + i\varepsilon_2^L$, can be written as [3,21]:

$$\mathrm{Im}\left[\frac{-1}{\varepsilon^L(q,\omega;\omega_p)}\right] = \frac{\varepsilon_2^L}{(\varepsilon_1^L)^2 + (\varepsilon_2^L)^2}, \tag{6a}$$

$$\varepsilon_1^L(q,\omega;\omega_p) = 1 + \frac{1}{\pi k_F z^2}\left[\frac{1}{2} + \frac{1}{8z}\left\{F\left(z-\frac{x}{4z}\right) + F\left(z+\frac{x}{4z}\right)\right\}\right], \tag{6b}$$

$$\varepsilon_2^L(q,\omega;\omega_p) = \frac{1}{8k_F z^3}\times\begin{cases} x & \text{for} \quad 0 < x < 4z(1-z) \\ 1-(z-(x/4z))^2 & \text{for} \quad |4z(1-z)| < x < 4z(1+z), \\ 0 & \text{otherwise} \end{cases} \tag{6c}$$

where $F(t) = (1-t^2)\ln|(t+1)/(t-1)|$, $x = \omega/E_f$, $z = q/2k_F$, and k_F is the Fermi wave vector corresponding to a given ω_p .

We used the following expressions for the real and imaginary parts of the Lindhard dielectric function in our numerical calculations to reduce numerical errors at the limiting conditions of $\omega/qk_F(=u) \ll 1$ and $u \gg z+1$. When $u \ll 1$, ε_1^L and ε_2^L can be written as:

$$\begin{aligned} \varepsilon_1^L(q,\omega;\omega_p) = 1 + \frac{1}{\pi k_F z^2}\Bigg[\frac{1}{2} + \frac{1}{4z}\Bigg\{&(1-z^2-u^2)\ln\left|\frac{z+1}{z-1}\right| \\ &+(z^2-u^2-1)\frac{2u^2 z}{(z^2-1)^2}\Bigg\}\Bigg] \end{aligned} \tag{7a}$$

and

$$\varepsilon_2^L(q,\omega;\omega_p) = \frac{u}{2k_F z^2}. \tag{7b}$$

When $u \gg z+1$, ε_1^L and ε_2^L can be expressed as:

$$\varepsilon_1^L(q,\omega;\omega_p) = 1 - \frac{\omega_p^2}{\omega^2}\left\{1 + \left(z^2 + \frac{3}{5}\right)\frac{1}{u^2}\right\} \tag{8a}$$

]and

$$\varepsilon_2^L(q,\omega;\omega_p) = 0. \tag{8b}$$

The energy-loss function in Eq. (5) from the FPA can be described as the sum of two contributions, one associated with the plasmon pole and the other with single-electron excitations [3,21,22]. That is,

$$\mathrm{Im}\left[\frac{-1}{\varepsilon(q,\omega)}\right] = \mathrm{Im}\left[\frac{-1}{\varepsilon(q,\omega)}\right]_{pl} + \mathrm{Im}\left[\frac{-1}{\varepsilon(q,\omega)}\right]_{se}. \tag{9}$$

The plasmon-pole contribution can be expressed as:

$$\mathrm{Im}\left[\frac{-1}{\varepsilon(q,\omega)}\right]_{pl} = g(\omega_0)\frac{\pi}{|\partial\varepsilon_1^L(q,\omega;\omega_p)/\partial\omega_p|_{\omega_p=\omega_0}}\Theta(q^-(\omega;\omega_0)-q), \tag{10a}$$

where

$$\frac{\partial\varepsilon_1^L(q,\omega;\omega_p)}{\partial\omega_p} = \frac{1}{3\pi\omega_p q z^2}\left\{\ln\left|\frac{Y_-+1}{Y_--1}\right| + \ln\left|\frac{Y_++1}{Y_+-1}\right|\right\}, \tag{10b}$$

and $Y_\pm \equiv z \pm x/4z$. To reduce calculation errors for $z/x \ll 1$ and for $z/x \gg 1$, we use the following equations:

$$\begin{aligned} &\ln\left|\frac{Y_-+1}{Y_--1}\right| + \ln\left|\frac{Y_++1}{Y_+-1}\right| \\ &\approx -\frac{64}{3}za^2\{3 + 48(1+z^2)a^2 + 256(3+z^2)(1+3z^2)a^4\}, \end{aligned} \tag{10c}$$

where $a \equiv z/x$ when $z/x \ll 1$, and

$$\begin{aligned} &\ln\left|\frac{Y_-+1}{Y_--1}\right| + \ln\left|\frac{Y_++1}{Y_+-1}\right| \\ &\approx \ln\left(\frac{z+1}{z-1}\right)^2 + 4zb^2\{1 + (1+z^2)b^2 + \frac{1}{3}(3+z^2)(1+3z^2)b^4\}, \end{aligned} \tag{10d}$$

where $b \equiv x/(z(z^2-1)$ when $z/x \gg 1$.

The single-electron-excitation contribution in Eq. (9) is given by:

$$\mathrm{Im}\left[\frac{-1}{\varepsilon(q,\omega)}\right]_{se} = \int_0^\infty d\omega_p g(\omega_p)\mathrm{Im}\left[\frac{-1}{\varepsilon^L(q,\omega;\omega_p)}\right]\Theta(q^+(\omega;\omega_p) - q)\Theta(q - q^-(\omega;\omega_p)), \tag{11a}$$

where

$$q^\pm(\omega;\omega_p) = \pm k_F(\omega_p) + \sqrt{k_F^2(\omega_p) + 2\omega}. \tag{11b}$$

Finally, when $Y_- = \pm 1$ (corresponding to quadratic curves in the (q,ω) plane separating single-electron excitations), we note that $F(\pm 1)$ is theoretically zero.

Several factors limit the reliability of SPs calculated from our model [2]. First, the Lindhard dielectric function model used in the FPA is expected to provide a useful approximation for the q-dependence of valence-electron excitations in free-electron-like materials but may be less reliable for non-free-electron-like solids. Second, use of the Lindhard model for describing the q-dependence of core-electron excitations is unlikely to be correct. Third, no account has been taken of exchange effects in inelastic scattering. Nevertheless, IMFPs calculated from optical ELFs with the FPA and the SPA are in good agreement with IMFPs determined experimentally by elastic-peak electron spectroscopy (EPES) in many elemental solids (including non-free-electron-like solids) for electron energies between 100 eV and 5 keV [23–25]. It is difficult to extend these comparisons to energies less than 100 eV due to limitations of the EPES technique [26].

3. Results

3.1. Stopping powers from the full Penn algorithm

We calculated values of the mass collision SP, S/ρ, where ρ is the mass density of the solid. Values of S/ρ were determined for 41 elemental solids (Li, Be, graphite, diamond, glassy C, Na, Mg, Al, Si, K, Sc, Ti, V, Cr, Fe, Co, Ni, Cu, Ge, Y, Nb, Mo, Ru, Rh, Pd, Ag, In, Sn, Cs, Gd, Tb, Dy, Hf, Ta, W, Re, Os, Ir, Pt, Au, and Bi) from the FPA. We utilized the same sets of optical ELFs as those used in our recent calculations of IMFPs for the same solids over the same energy range [6]. For 19 of our 41 solids (Ti, V, Cr, Fe, Ni, Y, Nb, Mo, Ru, Rh, Pd, Hf, Ta, W, Re, Os, Ir, Pt, and Au), we adopted improved sets of optical ELF data [6] compared to those used for our previous SP results [1,2]. We note that the new ELF data sets for Mg and Cu utilized in our recent IMFP calculations [6] had also been employed in our previous SP calculations for these solids [2]. Although we previously reported SPs for Zr [2], further analysis of its optical ELF data showed what we considered to be excessive errors in values of the f-sum and KK-sum [6] that we used to evaluate the internal consistency of a given ELF data set. Our SP values for Zr should therefore be considered only as rough estimates.

Values of S/ρ were calculated for relativistic electron kinetic energies between 10 eV and 30 keV (with respect to the Fermi level) at equal intervals on a logarithmic energy scale corresponding to increases of 10%. Table 1 shows the S/ρ values for our 41 elemental solids at electron energies between 50 eV and 30 keV. These SPs are given in units of MeVcm^2/g. The mass collision SPs can be converted to collision SPs (e.g., in eV/Å or eV/nm units) by multiplying by the material densities given in Table 1 of Ref. [6].

Plots of calculated mass collision SPs from the FPA as a function of energy are shown as solid lines in Figs. 1–7. SPs are included in these plots for energies less than 50 eV to illustrate trends, but these data are not considered as reliable [2]. The solid circles in Figs. 1–7 are SPs calculated with the SPA [1,2]. The SPs calculated with the FPA and SPA show similar systematic trends with atomic number. Sometimes, a single maximum is observed in the SP-versus-energy curves, sometimes secondary structures or multiple maxima are observed, and there are varying widths of the main maximum that generally occurs at energies between 10 eV and 300 eV. These trends have been discussed previously and are due to the varying contributions of valence-electron and different inner-shell excitations to the SP [2,27]. We also see in Figs. 1–7 that SPs from the SPA are larger than those from the FPA at energies in the vicinity of the maximum in each SP-versus-energy curve. On the other hand, SPs from the SPA are smaller than the corresponding SPs from the FPA for very low energies (typically less than 30 eV). This result is mainly due to differences in the ELF models used in each algorithm and will be discussed in more detail later.

The dashed lines in Figs. 1–7 show mass collision SPs calculated from the relativistic Bethe equation [2,14–16]:

$$S/\rho = \frac{784.58Z}{m_e v^2 A}[\ln(T/I)^2 + \ln(1+\tau/2) + G(\tau)] \quad (\text{in MeVcm}^2\text{g}^{-1}), \tag{12a}$$

where

$$G(\tau) = (1-\beta^2)[1 + \tau^2/8 - (2\tau+1)\ln 2], \tag{12b}$$

Z is the atomic number of the target, β is the electron velocity divided by the velocity of light, c, $\tau = T/m_e c^2$ is the ratio of the electron relativistic kinetic energy to its rest energy, and I is the mean excitation energy (MEE). Eq. (12) omits a density-effect correction which has been assumed here to be zero since its contribution is very small (less than 0.3% for our energy range [7]). SPs were calculated from Eq. (12) using MEEs listed in Table 4.3 of Ref. [7] except for the three carbon allotropes. SPs for glassy C, graphite and diamond were calculated with MEEs from our previous analysis [2]. SPs from Eq. (12) are shown in Figs. 1–7 from the minimum energies for which S is positive to 30 keV. As expected, we see generally good agreement between SPs from the FPA and those from Eq. (12) for energies larger than 10 keV. The root-mean-square (RMS) relative deviations between these calculated SPs and those from the Bethe equation were 9.1% and 8.7% at energies of 9.897 and 29.733 keV, respectively. These RMS deviations are almost the same as the corresponding deviations of 9.8% and 8.5% found previously between our SPs from the SPA and those from the Bethe equation [2].

3.2. Comparisons of stopping powers from new and old energy-loss functions

The energy-loss function (ELF) is the critical material-dependent parameter in our SP calculations. These ELFs were obtained from experimental optical data or ELF measurements for each solid. Sources of ELF data were given and details of our ELF analyses were described in a previous paper [6]. We comment now on differences between ELFs for 19 solids (Ti, V, Cr, Fe, Ni, Y, Nb, Mo, Ru, Rh, Pd, Hf, Ta, W, Re, Os, Ir, Pt, and Au) used here and the ELFs used for our previous SP calculations [1,2].

We first point out that we utilized photoabsorption data for these 19 solids at photon energies over 50 eV from Henke et al. [28] that are more recent than the data used previously [1,2]. For eight of these solids (Cr, Fe, Mo, Hf, Ta, W, Re, and Pt), it was necessary to make interpolations between two photon-energy (or electron energy-loss) regions, and we were guided in this process by measured transmission and reflection electron energy-loss spectroscopy (EELS) data. The resulting ELFs agreed better overall with the energy-loss data and resulted in smaller sum-rule errors for most of the solids than in our earlier SP and IMFP work [1,2,5,29]. For Ti, we selected optical data from a recent analysis of reflection EELS data by Werner et al. [30] for energy losses up to 54 eV because the resulting ELF was in much better agreement

Table 1
Calculated mass collision SPs (i.e., collision SPs divided by density) for the 41 elemental solids as a function of electron relativistic kinetic energy *T*.

T (eV)	Collision stopping power/density ($MeVcm^2g^{-1}$)						
	Li	Be	C (glassy)	C (graphite)	C (diamond)	Na	Mg
54.6	439.6	361.6	217.0	259.7	141.7	187.2	240.0
60.3	422.3	366.0	227.8	286.5	166.1	180.9	235.2
66.7	404.6	366.8	236.6	307.7	192.0	175.0	229.5
73.7	387.1	364.3	243.3	323.4	216.4	169.8	223.4
81.5	369.8	359.1	247.9	334.3	236.7	165.6	217.0
90.0	353.3	351.8	250.5	340.8	251.6	163.0	210.5
99.5	337.3	342.7	251.3	343.4	261.8	161.6	204.1
109.9	322.4	332.3	250.5	342.8	267.8	160.9	198.0
121.5	308.3	320.8	248.2	339.4	270.3	160.7	192.2
134.3	295.4	308.6	244.4	333.8	270.0	160.7	187.4
148.4	284.8	296.0	239.4	326.3	267.4	160.9	183.6
164.0	276.7	283.2	233.4	317.3	262.9	160.9	180.5
181.3	270.0	270.2	226.4	307.0	256.8	160.8	177.9
200.3	263.4	257.6	218.7	295.9	249.4	160.4	175.9
221.4	256.6	245.1	210.5	284.1	241.1	159.6	173.8
244.7	249.4	233.0	201.9	271.8	232.1	158.2	171.5
270.4	241.9	221.4	193.2	259.3	222.6	156.3	169.0
298.9	233.7	210.4	184.2	246.7	212.8	153.8	166.0
330.3	224.9	200.2	175.3	234.2	202.8	150.7	162.5
365.0	215.7	191.2	166.4	221.7	192.7	147.1	158.6
403.4	206.2	182.9	157.7	209.6	182.8	142.9	154.1
445.9	196.5	174.8	149.2	197.7	173.0	138.3	149.3
492.7	186.7	166.9	140.9	186.2	163.4	133.4	144.0
544.6	177.0	159.0	133.0	175.2	154.1	128.1	138.6
601.8	167.3	151.2	125.3	164.6	145.2	122.7	132.9
665.1	157.8	143.5	118.1	154.5	136.6	117.2	127.1
735.1	148.6	135.9	111.2	145.0	128.4	111.5	121.3
812.4	139.6	128.4	104.7	135.9	120.7	105.9	115.5
897.8	130.9	121.1	98.6	127.4	113.4	100.3	109.7
992.3	122.6	114.0	92.9	119.5	106.6	94.8	103.9
1096.6	114.6	107.2	87.8	112.2	100.3	89.4	98.3
1212.0	107.1	100.6	83.2	105.4	94.5	84.1	92.8
1339.4	99.9	94.2	78.8	99.0	88.9	79.1	87.4
1480.3	93.0	88.2	74.5	92.9	83.6	74.2	82.2
1636.0	86.6	82.4	70.3	87.1	78.6	69.5	77.2
1808.0	80.5	76.9	66.3	81.5	73.7	65.0	72.4
1998.2	74.8	71.7	62.4	76.3	69.1	60.7	67.8
2208.3	69.4	66.7	58.6	71.3	64.7	56.7	63.4
2440.6	64.4	62.1	55.0	66.5	60.5	52.9	59.3
2697.3	59.7	57.7	51.6	62.0	56.5	49.3	55.3
2981.0	55.3	53.6	48.3	57.8	52.7	45.9	51.5
3294.5	51.2	49.7	45.1	53.8	49.1	42.7	48.0
3640.9	47.4	46.1	42.1	50.0	45.7	39.7	44.7
4023.9	43.8	42.7	39.3	46.5	42.5	36.9	41.5
4447.1	40.5	39.6	36.6	43.2	39.5	34.3	38.6
4914.8	37.5	36.7	34.0	40.0	36.7	31.9	35.9
5431.7	34.6	33.9	31.7	37.1	34.1	29.7	33.3
6002.9	32.0	31.4	29.4	34.4	31.6	27.6	31.0
6634.2	29.5	29.0	27.3	31.9	29.3	25.7	28.8
7332.0	27.3	26.8	25.3	29.5	27.2	23.9	26.7
8103.1	25.2	24.8	23.5	27.3	25.2	22.2	24.8
8955.3	23.2	22.9	21.8	25.3	23.3	20.6	23.1
9897.1	21.4	21.2	20.2	23.4	21.6	19.1	21.4
10938.0	19.8	19.6	18.7	21.6	20.0	17.7	19.9
12088.4	18.3	18.1	17.3	20.0	18.5	16.5	18.5
13359.7	16.9	16.7	16.0	18.5	17.1	15.3	17.1
14764.8	15.6	15.4	14.9	17.1	15.8	14.2	15.9
16317.6	14.4	14.2	13.7	15.8	14.6	13.1	14.7
18033.7	13.3	13.1	12.7	14.6	13.5	12.2	13.7
19930.4	12.2	12.1	11.8	13.5	12.5	11.3	12.7
22026.5	11.3	11.2	10.9	12.5	11.6	10.5	11.8
24343.0	10.4	10.4	10.1	11.6	10.7	9.7	10.9
26903.2	9.65	9.60	9.36	10.7	9.92	9.01	10.1
29732.6	8.92	8.88	8.67	9.91	9.18	8.36	9.39

T (eV)	Al	Si	K	Sc	Ti	V	Cr
54.6	220.1	227.7	156.8	152.7	119.4	79.9	73.6
60.3	216.9	226.1	163.6	161.8	125.4	84.5	79.8
66.7	212.6	222.9	170.4	170.6	130.4	88.6	85.1
73.7	207.3	218.4	175.9	179.1	134.6	92.2	89.5
81.5	201.2	212.8	180.7	187.3	138.4	95.2	92.9
90.0	194.8	206.6	186.3	195.5	142.5	98.0	95.5
99.5	188.0	199.7	189.8	204.0	147.4	100.9	97.4

Table 1 (*continued*)

T (eV)	Al	Si	K	Sc	Ti	V	Cr
109.9	181.1	192.6	190.1	212.6	153.5	104.1	98.8
121.5	174.0	185.1	187.7	219.3	159.5	107.7	100.2
134.3	167.1	177.6	183.1	221.5	163.3	111.5	101.7
148.4	160.4	170.1	177.2	220.2	163.5	114.8	103.0
164.0	154.1	162.7	170.5	216.2	161.4	117.3	104.0
181.3	148.1	155.6	163.3	210.6	157.9	118.7	104.4
200.3	142.7	148.8	156.1	203.9	153.7	119.0	104.1
221.4	138.1	142.3	148.8	196.4	148.9	118.4	103.1
244.7	134.0	136.3	141.6	188.5	143.8	116.9	101.5
270.4	130.5	130.7	134.6	180.3	138.4	114.9	99.5
298.9	127.2	125.9	127.7	172.0	132.8	112.2	97.0
330.3	124.1	122.1	121.0	163.7	127.2	109.1	94.3
365.0	121.0	118.7	114.6	155.5	121.4	105.6	91.3
403.4	117.9	115.6	108.3	147.4	115.7	101.7	88.2
445.9	114.6	112.6	102.3	139.5	110.0	97.6	84.9
492.7	111.2	109.7	96.6	131.8	104.4	93.5	81.5
544.6	107.7	106.6	91.1	124.3	98.9	89.2	78.1
601.8	104.0	103.5	86.0	117.1	93.6	85.0	74.6
665.1	100.2	100.1	81.1	110.2	88.4	80.8	71.1
735.1	96.3	96.5	76.4	103.7	83.4	76.6	67.7
812.4	92.3	92.8	72.1	97.4	78.6	72.6	64.2
897.8	88.3	89.0	68.1	91.4	74.0	68.6	60.9
992.3	84.2	85.1	64.4	85.8	69.6	64.8	57.6
1096.6	80.1	81.1	61.1	80.5	65.4	61.1	54.5
1212.0	76.0	77.1	58.1	75.5	61.5	57.6	51.4
1339.4	72.0	73.1	55.4	70.8	57.7	54.2	48.5
1480.3	68.0	69.1	52.7	66.5	54.2	51.0	45.7
1636.0	64.1	65.3	50.2	62.5	51.0	48.0	43.0
1808.0	60.4	61.5	47.7	58.9	47.9	45.1	40.5
1998.2	56.7	57.8	45.2	55.5	45.2	42.5	38.1
2208.3	53.2	54.3	42.8	52.2	42.6	40.0	35.9
2440.6	49.9	50.9	40.5	49.2	40.2	37.8	33.9
2697.3	46.6	47.6	38.2	46.2	37.9	35.7	32.0
2981.0	43.6	44.5	35.9	43.4	35.7	33.7	30.3
3294.5	40.7	41.6	33.8	40.7	33.6	31.7	28.6
3640.9	37.9	38.8	31.7	38.1	31.5	29.8	27.0
4023.9	35.3	36.2	29.7	35.6	29.6	28.1	25.4
4447.1	32.9	33.7	27.8	33.3	27.7	26.3	23.9
4914.8	30.6	31.3	26.0	31.1	25.9	24.7	22.5
5431.7	28.5	29.1	24.3	29.0	24.3	23.1	21.1
6002.9	26.4	27.1	22.7	27.0	22.7	21.6	19.8
6634.2	24.6	25.2	21.1	25.2	21.1	20.2	18.5
7332.0	22.8	23.4	19.7	23.4	19.7	18.9	17.3
8103.1	21.2	21.7	18.3	21.8	18.4	17.6	16.2
8955.3	19.7	20.1	17.1	20.2	17.1	16.4	15.1
9897.1	18.3	18.7	15.9	18.8	15.9	15.3	14.1
10938.0	17.1	17.4	14.7	17.4	14.8	14.2	13.2
12088.4	15.8	16.1	13.7	16.2	13.7	13.2	12.3
13359.7	14.7	15.0	12.7	15.0	12.8	12.3	11.4
14764.8	13.7	13.9	11.8	13.9	11.9	11.4	10.6
16317.6	12.7	12.9	11.0	12.9	11.0	10.6	9.87
18033.7	11.8	12.0	10.2	12.0	10.2	9.87	9.18
19930.4	10.9	11.1	9.4	11.1	9.48	9.17	8.53
22026.5	10.2	10.3	8.8	10.3	8.80	8.52	7.93
24343.0	9.44	9.60	8.15	9.57	8.17	7.91	7.37
26903.2	8.76	8.92	7.58	8.88	7.59	7.35	6.86
29732.6	8.14	8.28	7.05	8.25	7.05	6.83	6.38

T (eV)	Fe	Co	Ni	Cu	Ge	Y
54.6	66.9	56.8	53.3	49.6	96.0	83.4
60.3	70.5	62.1	57.7	53.3	95.8	88.7
66.7	73.5	67.2	62.1	57.0	95.3	94.2
73.7	75.9	71.7	66.4	60.3	94.5	99.9
81.5	77.7	75.6	70.4	63.2	93.4	106.1
90.0	79.2	79.0	74.0	65.7	92.0	112.1
99.5	80.4	81.9	77.2	68.0	90.5	117.0
109.9	81.3	84.4	80.0	70.0	88.8	120.0
121.5	82.0	86.6	82.4	71.7	87.1	121.0
134.3	82.5	88.6	84.5	73.1	85.5	120.2
148.4	83.5	90.7	86.3	74.3	83.8	118.0
164.0	84.8	93.7	87.7	75.2	82.2	114.9
181.3	85.8	96.2	89.0	75.9	80.7	111.0
200.3	86.2	97.7	90.3	76.4	79.3	106.7
221.4	86.2	98.3	91.3	76.7	77.9	102.2
244.7	85.8	98.3	91.9	76.9	76.5	97.5

(*continued on next page*)

Table 1 (*continued*)

T (eV)	Fe	Co	Ni	Cu	Ge	Y
270.4	84.9	97.6	92.0	76.9	75.1	92.8
298.9	83.8	96.4	91.6	76.5	73.8	88.2
330.3	82.3	94.8	90.6	75.8	72.4	83.7
365.0	80.5	92.9	89.2	74.9	71.1	79.4
403.4	78.6	90.6	87.4	73.8	69.7	75.2
445.9	76.4	88.0	85.4	72.5	68.2	71.3
492.7	74.0	85.2	83.0	70.9	66.7	67.6
544.6	71.5	82.2	80.4	69.2	65.1	64.2
601.8	68.9	79.0	77.7	67.3	63.5	61.0
665.1	66.2	75.8	74.8	65.2	61.7	58.1
735.1	63.4	72.5	71.8	63.0	59.9	55.5
812.4	60.6	69.2	68.7	60.6	57.9	53.0
897.8	57.8	65.8	65.6	58.2	55.9	50.8
992.3	55.0	62.5	62.5	55.7	53.8	48.6
1096.6	52.2	59.3	59.4	53.2	51.7	46.5
1212.0	49.5	56.1	56.3	50.6	49.5	44.6
1339.4	46.8	52.9	53.2	48.1	47.2	42.6
1480.3	44.2	49.9	50.3	45.6	45.0	40.8
1636.0	41.7	47.0	47.4	43.2	42.8	38.9
1808.0	39.3	44.2	44.7	40.8	40.6	37.1
1998.2	37.0	41.5	42.0	38.5	38.4	35.2
2208.3	34.8	39.0	39.5	36.2	36.3	33.5
2440.6	32.8	36.6	37.1	34.1	34.2	31.7
2697.3	30.8	34.3	34.8	32.1	32.2	30.0
2981.0	29.0	32.2	32.6	30.1	30.3	28.3
3294.5	27.3	30.2	30.6	28.3	28.5	26.7
3640.9	25.8	28.4	28.7	26.6	26.7	25.1
4023.9	24.3	26.7	26.9	24.9	25.0	23.6
4447.1	22.9	25.0	25.3	23.4	23.5	22.1
4914.8	21.6	23.5	23.8	22.0	22.0	20.7
5431.7	20.3	22.1	22.3	20.7	20.6	19.4
6002.9	19.0	20.7	20.9	19.5	19.3	18.2
6634.2	17.9	19.4	19.6	18.3	18.1	17.0
7332.0	16.7	18.2	18.4	17.1	16.9	15.8
8103.1	15.7	17.0	17.2	16.0	15.9	14.8
8955.3	14.6	15.9	16.1	15.0	14.9	13.8
9897.1	13.7	14.8	15.0	14.0	13.9	12.9
10938.0	12.8	13.8	14.0	13.1	13.0	12.0
12088.4	11.9	12.9	13.1	12.3	12.1	11.2
13359.7	11.1	12.0	12.2	11.4	11.3	10.5
14764.8	10.3	11.2	11.4	10.7	10.6	9.77
16317.6	9.62	10.4	10.6	9.94	9.87	9.12
18033.7	8.96	9.65	9.84	9.25	9.20	8.51
19930.4	8.33	8.98	9.16	8.62	8.58	7.94
22026.5	7.75	8.35	8.52	8.02	7.99	7.40
24343.0	7.21	7.76	7.92	7.47	7.44	6.90
26903.2	6.71	7.22	7.37	6.95	6.93	6.44
29732.6	6.24	6.72	6.86	6.47	6.45	6.00

T (eV)	Nb	Mo	Ru	Rh	Pd	Ag	In
54.6	48.0	48.6	39.8	40.9	40.7	36.4	53.9
60.3	51.9	54.1	44.7	45.6	45.3	40.8	55.1
66.7	55.5	59.0	50.1	50.6	50.3	45.6	56.3
73.7	59.0	63.2	55.5	55.8	55.3	50.7	57.6
81.5	62.5	66.9	60.6	61.0	60.4	56.0	59.1
90.0	66.3	70.4	64.9	65.8	65.2	61.3	60.7
99.5	70.6	73.9	68.8	69.9	69.6	66.6	62.5
109.9	75.3	77.6	72.1	73.3	73.5	71.7	64.4
121.5	80.0	81.3	75.0	76.3	77.0	76.6	66.3
134.3	84.1	84.8	77.7	79.1	80.2	81.3	68.3
148.4	86.7	87.2	80.1	81.7	82.9	85.5	70.2
164.0	87.8	88.4	82.1	84.0	85.3	89.2	72.0
181.3	87.6	88.3	83.5	85.9	87.1	92.4	73.5
200.3	86.2	87.1	83.9	87.0	88.3	94.9	74.7
221.4	84.1	85.1	83.2	87.2	88.4	96.7	75.6
244.7	81.4	82.5	81.7	86.4	87.5	97.5	76.1
270.4	78.4	79.5	79.4	84.6	85.5	97.1	76.1
298.9	75.2	76.3	76.7	82.1	82.9	95.6	75.4
330.3	71.9	72.9	73.7	79.2	79.8	93.2	74.0
365.0	68.6	69.6	70.5	76.0	76.4	90.2	72.0
403.4	65.3	66.2	67.3	72.6	73.0	86.7	69.5
445.9	62.0	62.9	64.1	69.2	69.5	83.0	66.7
492.7	58.9	59.7	60.9	65.8	66.0	79.3	63.8
544.6	55.9	56.6	57.8	62.5	62.6	75.5	60.8
601.8	53.1	53.7	54.8	59.3	59.3	71.8	57.8

Table 1 (*continued*)

T (eV)	Nb	Mo	Ru	Rh	Pd	Ag	In
665.1	50.4	50.9	51.9	56.1	56.1	68.1	54.8
735.1	48.0	48.3	49.1	53.1	53.1	64.6	51.9
812.4	45.7	45.9	46.5	50.3	50.2	61.2	49.1
897.8	43.6	43.7	44.1	47.6	47.4	58.0	46.5
992.3	41.7	41.7	41.8	45.1	44.8	54.9	43.9
1096.6	39.9	39.8	39.6	42.7	42.4	52.1	41.5
1212.0	38.2	38.1	37.7	40.4	40.0	49.3	39.2
1339.4	36.6	36.5	36.0	38.4	37.9	46.8	37.0
1480.3	35.0	35.0	34.3	36.6	36.0	44.5	34.9
1636.0	33.5	33.5	32.8	34.8	34.2	42.5	33.0
1808.0	32.0	32.0	31.3	33.2	32.5	40.5	31.2
1998.2	30.5	30.6	29.9	31.7	31.0	38.5	29.6
2208.3	29.1	29.2	28.5	30.2	29.5	36.6	28.1
2440.6	27.7	27.8	27.2	28.8	28.1	34.8	26.6
2697.3	26.3	26.5	25.9	27.4	26.7	33.0	25.3
2981.0	24.9	25.1	24.6	26.0	25.4	31.2	24.0
3294.5	23.6	23.8	23.3	24.6	24.1	29.4	22.8
3640.9	22.3	22.5	22.1	23.3	22.8	27.7	21.6
4023.9	21.0	21.3	20.9	22.0	21.5	26.1	20.5
4447.1	19.8	20.0	19.7	20.8	20.3	24.6	19.4
4914.8	18.6	18.8	18.6	19.6	19.2	23.1	18.3
5431.7	17.5	17.7	17.5	18.4	18.1	21.6	17.2
6002.9	16.4	16.6	16.4	17.3	17.0	20.3	16.2
6634.2	15.4	15.6	15.4	16.2	15.9	19.0	15.3
7332.0	14.4	14.6	14.4	15.2	14.9	17.7	14.3
8103.1	13.4	13.6	13.5	14.3	14.0	16.5	13.4
8955.3	12.6	12.8	12.6	13.3	13.1	15.4	12.6
9897.1	11.7	11.9	11.8	12.5	12.2	14.4	11.8
10938.0	11.0	11.1	11.0	11.6	11.4	13.4	11.0
12088.4	10.2	10.4	10.3	10.9	10.7	12.5	10.3
13359.7	9.56	9.70	9.62	10.1	9.96	11.6	9.62
14764.8	8.93	9.05	8.97	9.45	9.30	10.8	8.98
16317.6	8.35	8.45	8.37	8.82	8.67	10.1	8.38
18033.7	7.80	7.90	7.81	8.23	8.09	9.38	7.81
19930.4	7.29	7.38	7.30	7.68	7.55	8.73	7.29
22026.5	6.81	6.89	6.81	7.17	7.04	8.13	6.80
24343.0	6.36	6.43	6.36	6.69	6.57	7.57	6.34
26903.2	5.94	6.01	5.94	6.25	6.14	7.06	5.92
29732.6	5.54	5.61	5.55	5.83	5.73	6.58	5.53

T (eV)	Sn	Cs	Gd	Tb	Dy	Hf	Ta
54.6	48.8	86.0	57.6	60.9	53.5	29.8	31.1
60.3	50.2	86.8	60.9	64.8	57.3	31.7	33.5
66.7	51.6	86.7	64.3	68.8	61.0	33.7	35.6
73.7	52.8	85.9	67.3	72.8	64.7	35.8	37.6
81.5	53.9	84.5	69.6	77.1	68.4	37.9	39.5
90.0	55.0	82.7	71.2	81.4	72.1	40.2	41.3
99.5	56.2	80.4	72.1	85.2	75.5	42.5	43.2
109.9	57.6	77.9	72.4	88.1	78.3	44.7	45.1
121.5	59.1	75.3	72.3	89.8	80.2	46.8	46.9
134.3	60.9	72.6	71.8	90.3	81.3	48.6	48.7
148.4	62.8	70.1	70.8	89.9	81.4	49.9	50.2
164.0	64.8	67.7	69.6	88.8	80.9	50.8	51.2
181.3	66.8	65.4	68.2	87.2	79.8	51.1	51.8
200.3	68.5	63.4	66.5	85.2	78.4	51.0	51.8
221.4	70.0	61.8	64.7	83.0	76.6	50.6	51.5
244.7	71.1	60.5	62.9	80.5	74.7	49.9	50.9
270.4	71.6	59.8	61.0	77.9	72.6	49.1	50.0
298.9	71.5	59.6	59.0	75.2	70.4	48.1	49.0
330.3	70.7	59.4	57.1	72.4	68.1	47.0	47.9
365.0	69.3	59.0	55.1	69.7	65.8	45.8	46.6
403.4	67.4	58.0	53.2	66.9	63.4	44.6	45.3
445.9	65.0	56.4	51.4	64.2	61.1	43.3	44.0
492.7	62.4	54.4	50.0	61.8	58.9	42.1	42.7
544.6	59.6	52.1	48.5	59.5	56.9	40.8	41.3
601.8	56.8	49.7	46.9	57.2	54.8	39.5	40.0
665.1	54.0	47.2	45.2	54.8	52.7	38.2	38.6
735.1	51.3	44.8	43.4	52.4	50.5	36.9	37.3
812.4	48.6	42.4	41.6	50.0	48.3	35.6	35.9
897.8	46.0	40.1	39.8	47.6	46.2	34.3	34.6
992.3	43.5	37.9	37.9	45.3	44.0	33.0	33.3
1096.6	41.1	35.8	36.1	43.0	41.9	31.7	32.0
1212.0	38.8	33.8	34.3	40.8	39.8	30.4	30.7
1339.4	36.7	31.9	32.6	38.6	37.8	29.1	29.4
1480.3	34.6	30.0	30.9	36.6	35.8	27.8	28.1

(*continued on next page*)

Table 1 (*continued*)

T (eV)	Sn	Cs	Gd	Tb	Dy	Hf	Ta
1636.0	32.7	28.3	29.3	34.5	33.9	26.6	26.9
1808.0	30.9	26.7	27.7	32.6	32.1	25.4	25.7
1998.2	29.2	25.1	26.2	30.8	30.3	24.2	24.5
2208.3	27.6	23.7	24.7	29.0	28.6	23.0	23.3
2440.6	26.2	22.3	23.3	27.3	26.9	21.8	22.1
2697.3	24.9	21.0	22.0	25.6	25.4	20.7	21.0
2981.0	23.6	19.8	20.7	24.1	23.9	19.6	19.9
3294.5	22.4	18.8	19.5	22.6	22.4	18.6	18.8
3640.9	21.3	17.8	18.3	21.2	21.1	17.5	17.8
4023.9	20.1	16.8	17.2	19.9	19.8	16.5	16.8
4447.1	19.1	15.9	16.2	18.7	18.5	15.6	15.8
4914.8	18.0	15.1	15.2	17.5	17.4	14.7	14.9
5431.7	17.0	14.3	14.3	16.4	16.3	13.8	14.0
6002.9	16.0	13.5	13.5	15.4	15.3	13.0	13.2
6634.2	15.1	12.7	12.7	14.5	14.3	12.2	12.4
7332.0	14.1	12.0	12.0	13.6	13.5	11.5	11.6
8103.1	13.3	11.3	11.3	12.8	12.7	10.8	10.9
8955.3	12.4	10.6	10.6	12.0	11.9	10.1	10.3
9897.1	11.6	10.0	10.0	11.3	11.2	9.54	9.64
10938.0	10.9	9.35	9.43	10.55	10.46	8.98	9.06
12088.4	10.2	8.77	8.87	9.89	9.81	8.45	8.52
13359.7	9.52	8.21	8.33	9.27	9.19	7.94	8.01
14764.8	8.88	7.68	7.82	8.67	8.61	7.46	7.52
16317.6	8.29	7.18	7.33	8.11	8.05	7.01	7.06
18033.7	7.74	6.71	6.87	7.58	7.53	6.58	6.62
19930.4	7.22	6.27	6.43	7.09	7.04	6.17	6.21
22026.5	6.73	5.86	6.02	6.62	6.57	5.78	5.82
24343.0	6.28	5.47	5.63	6.18	6.14	5.41	5.45
26903.2	5.86	5.11	5.27	5.77	5.73	5.07	5.11
29732.6	5.47	4.77	4.92	5.39	5.35	4.75	4.78

T (eV)	W	Re	Os	Ir	Pt	Au	Bi
54.6	27.0	24.4	21.1	21.7	23.7	24.3	40.8
60.3	30.3	28.1	23.9	24.6	26.4	26.9	42.1
66.7	33.3	32.0	26.9	27.8	29.4	29.7	43.2
73.7	36.0	35.3	29.9	31.0	32.5	32.6	44.3
81.5	38.2	38.0	32.6	34.2	35.5	35.7	45.4
90.0	39.9	40.3	35.0	36.9	38.1	38.7	46.5
99.5	41.4	42.3	36.8	39.1	40.3	41.6	47.8
109.9	42.9	44.0	38.3	41.0	42.1	44.2	49.0
121.5	44.3	45.6	39.7	42.6	43.6	46.5	50.4
134.3	45.8	47.1	41.1	44.0	44.9	48.4	51.9
148.4	47.3	48.4	42.5	45.1	45.9	49.9	53.4
164.0	48.4	49.5	43.7	46.0	46.6	51.0	54.8
181.3	49.1	50.2	44.5	46.6	47.0	51.8	56.0
200.3	49.3	50.5	44.9	47.0	47.1	52.1	56.9
221.4	49.1	50.3	44.9	46.9	46.9	52.0	57.3
244.7	48.5	49.7	44.6	46.4	46.5	51.5	57.4
270.4	47.7	48.8	43.9	45.7	45.8	50.7	57.0
298.9	46.8	47.7	43.0	44.7	44.8	49.7	56.1
330.3	45.6	46.5	42.0	43.5	43.7	48.4	54.9
365.0	44.5	45.2	40.9	42.2	42.5	47.0	53.5
403.4	43.2	43.8	39.7	40.8	41.1	45.4	51.7
445.9	41.9	42.5	38.5	39.4	39.7	43.7	49.8
492.7	40.7	41.1	37.3	38.1	38.3	42.0	47.8
544.6	39.4	39.7	36.1	36.7	37.0	40.3	45.8
601.8	38.1	38.3	34.9	35.4	35.6	38.6	43.7
665.1	36.8	37.0	33.7	34.1	34.3	37.0	41.7
735.1	35.6	35.6	32.5	32.9	33.1	35.4	39.7
812.4	34.3	34.3	31.4	31.7	31.9	34.0	37.8
897.8	33.1	33.0	30.3	30.6	30.7	32.5	36.0
992.3	31.9	31.8	29.2	29.4	29.5	31.2	34.3
1096.6	30.7	30.5	28.1	28.4	28.4	29.8	32.7
1212.0	29.5	29.3	27.0	27.3	27.3	28.6	31.2
1339.4	28.3	28.1	26.0	26.2	26.2	27.3	29.8
1480.3	27.1	26.9	24.9	25.2	25.2	26.1	28.4
1636.0	25.9	25.8	23.9	24.2	24.2	25.0	27.1
1808.0	24.8	24.6	22.9	23.2	23.1	23.9	25.9
1998.2	23.7	23.5	21.9	22.2	22.2	22.8	24.7
2208.3	22.6	22.4	20.9	21.2	21.2	21.8	23.5
2440.6	21.5	21.4	19.9	20.3	20.2	20.7	22.4
2697.3	20.4	20.3	19.0	19.3	19.3	19.7	21.3
2981.0	19.4	19.3	18.0	18.4	18.3	18.7	20.3
3294.5	18.4	18.3	17.1	17.4	17.4	17.8	19.2
3640.9	17.4	17.3	16.2	16.6	16.5	16.8	18.3

Table 1 (*continued*)

T (eV)	W	Re	Os	Ir	Pt	Au	Bi
4023.9	16.4	16.3	15.4	15.7	15.7	16.0	17.3
4447.1	15.5	15.4	14.5	14.8	14.8	15.1	16.4
4914.8	14.6	14.5	13.7	14.0	14.0	14.2	15.5
5431.7	13.7	13.7	12.9	13.2	13.2	13.4	14.6
6002.9	12.9	12.9	12.2	12.4	12.5	12.7	13.8
6634.2	12.2	12.1	11.5	11.7	11.7	11.9	12.9
7332.0	11.4	11.4	10.8	11.0	11.0	11.2	12.2
8103.1	10.7	10.7	10.1	10.3	10.4	10.5	11.4
8955.3	10.1	10.0	9.52	9.72	9.74	9.88	10.7
9897.1	9.46	9.42	8.94	9.13	9.14	9.27	10.0
10938.0	8.89	8.84	8.40	8.57	8.58	8.69	9.41
12088.4	8.36	8.31	7.89	8.05	8.06	8.16	8.82
13359.7	7.86	7.81	7.42	7.57	7.57	7.65	8.25
14764.8	7.38	7.34	6.98	7.11	7.11	7.19	7.73
16317.6	6.93	6.89	6.56	6.68	6.68	6.75	7.24
18033.7	6.51	6.47	6.16	6.27	6.28	6.34	6.78
19930.4	6.10	6.07	5.78	5.89	5.89	5.95	6.36
22026.5	5.72	5.69	5.42	5.53	5.53	5.58	5.95
24343.0	5.36	5.33	5.09	5.18	5.19	5.24	5.58
26903.2	5.02	5.00	4.77	4.86	4.86	4.91	5.23
29732.6	4.70	4.68	4.47	4.55	4.56	4.61	4.90

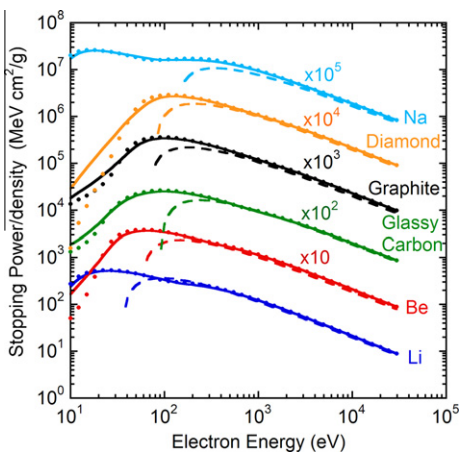

Fig. 1. Energy dependence of calculated mass collision stopping powers (or collision stopping powers divided by density) for Li, Be, glassy carbon, graphite, diamond, and Na. The solid lines show stopping powers calculated for each solid with the full Penn algorithm as a function of electron relativistic kinetic energy T. The solid circles show stopping powers calculated with the single-pole approximation. The dashed lines show stopping powers calculated from the relativistic Bethe equation (Eq. (12)).

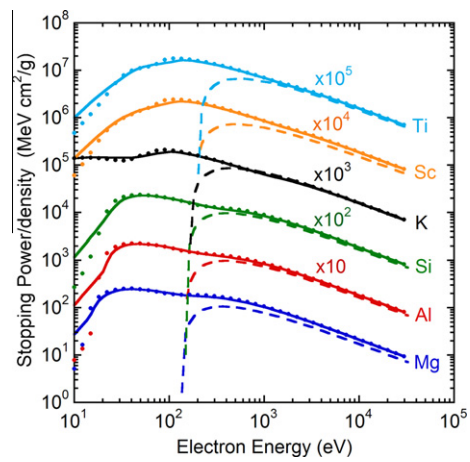

Fig. 2. Energy dependence of calculated mass collision stopping powers for Mg Al, Si, K, Sc, and Ti. See caption to Fig. 1.

with the reflection EELS data of Robins and Swan [31]. We also chose a set of optical data from Palik [32] for Au since this data set gave an ELF in better agreement with reflection EELS experiments [31] than the data set from Hagemann et al. [33] we used previously [1,2,5,29].

For two solids, Pd and V, there were large gaps in our previous ELFs (between 20 and 100 eV for Pd and between 40 and 100 eV for V). Our new ELF for Pd between 18 and 120 eV was obtained from an interpolation of ELF data [34] with a cubic spline function. The error in the f-sum for the new ELF was −2.3%, a value much smaller than that for the previous ELF (−12%) [29]. For V, we used a new set of optical data from Palik [32] for photon energies between 42.5 and 120 eV. We also chose new ELF data for photon energies less than 24 eV from Ref. [34] because this ELF better resembled transmission and reflection EELS data [30,35] than the previous ELF data. The resulting error in the f-sum was −0.8% (compared to the previous value of −20%) [29]. As a result, the new SPs for Pd and V are much larger than our previous SPs.

We checked the internal consistency of the new ELF data through use of the oscillator-strength sum rule (or f-sum rule) and a limiting form of the Kramers–Kronig integral (or KK-sum rule) [36–39]. The average root-mean-square (RMS) errors for the ELF data sets of our 41 solids were 4.2% and 7.7% based on the f-sum and KK-sum rules, respectively. These values are superior to the corresponding results for our previous ELFs (about 10% RMS error in both sum rules for 27 elemental solids) [5,29]. For over 80% of our 41 elemental solids, the ELFs satisfied the f-sum and KK-sum rules to better than 10%.

Fig. 8 shows ratios of SPs determined from the non-relativistic FPA, which are obtained from Eq. (3) when $T/c^2 \to 0$, and the new ELF data sets, S_{new}, to those calculated previously from the SPA and the old ELF data sets, S_{old}, [1,2] as a function of non-relativistic kinetic energy for the 19 elemental solids for which we adopted new ELF data. The largest changes occurred for Pd (where the SP increased by up to 58%), V (where the SP increased by up to 52%), and Re (where the SP decreased by up to 26%). These changes are the opposite of those found in similar comparisons of IMFPs (as shown in Fig. 11 of Ref. [6]). The changes in Fig. 8 result from two causes: use here of improved sets of ELF data [6] and differences in the SP calculation algorithms (the FPA and the SPA). The inset in

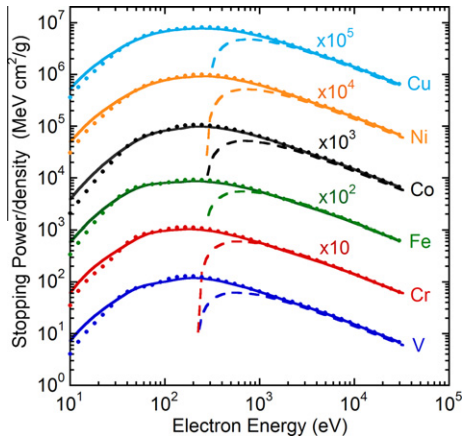

Fig. 3. Energy dependence of calculated mass collision stopping powers for V, Cr, Fe, Co, Ni, and Cu. See caption to Fig. 1.

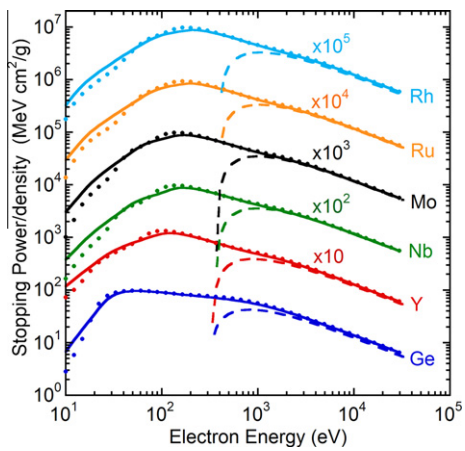

Fig. 4. Energy dependence of calculated mass collision stopping powers for Ge, Y, Nb, Mo, Ru, and Rh. See caption to Fig. 1.

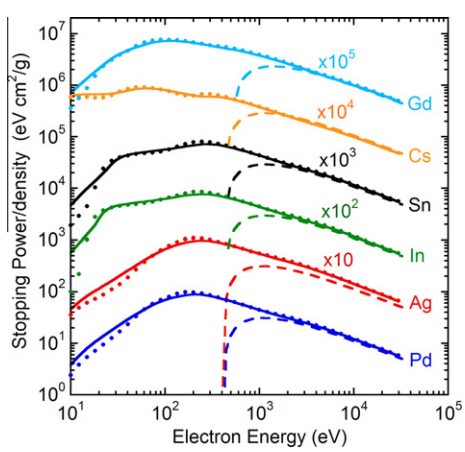

Fig. 5. Energy dependence of calculated mass collision stopping powers for Pd, Ag, In, Sn, Cs, and Gd. See caption to Fig. 1.

Fig. 8 shows ratios of SPs from the FPA, S_{FPA}, to those from the SPA, S_{SPA}, for the 19 solids that were calculated using the new ELFs for each algorithm. We see that the SP changes are smaller than 10% and that most of the differences occur for energies less than 200 eV (as will be discussed further in the following section). Since the ratios S_{new}/S_{old} in Fig. 8 generally deviate from unity by more than the values of S_{FPA}/S_{SPA} in the inset, it is clear that most of the changes in S_{new}/S_{old} are due to the differences in the ELFs.

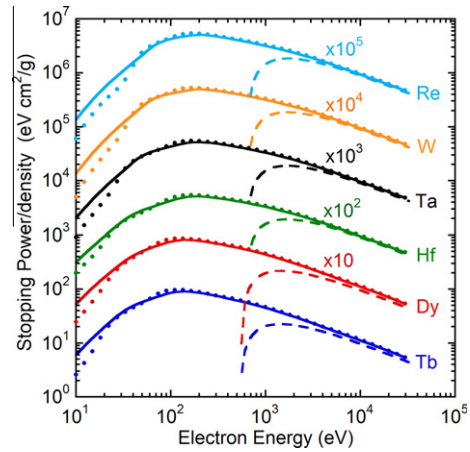

Fig. 6. Energy dependence of calculated mass collision stopping powers for Tb, Dy, Hf, Ta, W, and Re. See caption to Fig. 1.

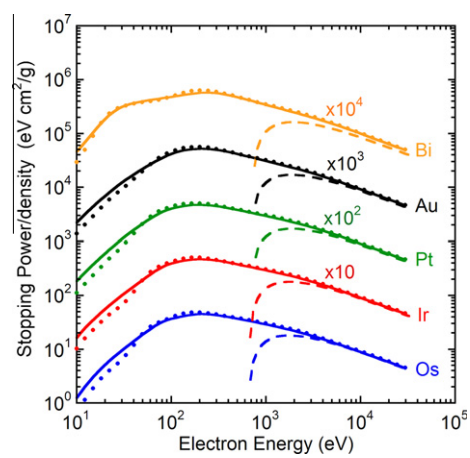

Fig. 7. Energy dependence of calculated mass collision stopping powers for Os, Ir, Pt, Au, and Bi. See caption to Fig. 1.

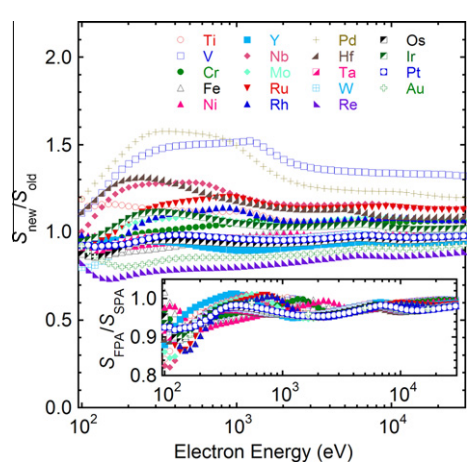

Fig. 8. Plots of ratios of SPs determined from the FPA and the new ELF data sets, S_{new}, to those calculated previously from the SPA and the old ELF data sets, S_{old}, [1,2] as a function of electron non-relativistic kinetic energy (i.e., $E = v^2/2$) for the 19 elemental solids for which we adopted new ELF data. The inset shows ratios of SPs from the FPA, S_{FPA}, to those from the SPA, S_{SPA}, for the same 19 solids. These SPs were calculated with the new ELFs for each algorithm.

3.3. Comparison of stopping powers from the FPA and SPA

We now make comparisons of RMS differences between SPs calculated from the FPA and SPA using the same (new) ELF data set for each of our 41 solids. Relative percentage RMS differences, *RMS*, were calculated from

$$RMS = 100 \times \left[\sum_{i=1}^{41} \left(\frac{S_{SPA}(T)_i - S_{FPA}(T)_i}{S_{FPA}(T)_i} \right)^2 / 41 \right]^{0.5} \quad (\%) \tag{13}$$

as a function of electron energy from 10 eV to 30 keV.

Fig. 9 shows plots of *RMS* as a function of relativistic kinetic energy. We see a steep decrease from about 50% for E = 10 eV to less than 10% for energies above 40 eV. The steep decrease must be due to the contributions of single-electron excitations to the SP that are neglected in the SPA (which only considers excitations at the plasmon pole). For energies above 40 eV, *RMS* generally decreases with increasing energy, reaching 1% at 30 keV. Three maxima are observed in Fig. 9 at energies of about 100 eV, 2 keV, and 10 keV. These maxima are due to the different energy positions of maxima and structure found in the SP plots from the FPA and SPA as a function of energy in Figs. 1–7.

3.4. Influence of electron exchange on stopping powers

It is important to know the effect of exchange between projectile and target electrons on SP calculations with the FPA. There is no consensus, however, on how to incorporate exchange effects within the dielectric formalism [6]. Nevertheless, we can estimate the influence of exchange on calculated SPs using the Born–Ochkur exchange correction [40,41].

The non-relativistic DCS with the Born–Ochkur correction can be written as [41]:

$$\frac{d^2\sigma}{dqd\omega} = \frac{C_{ex}}{\pi NE} \mathrm{Im}\left[\frac{-1}{\varepsilon(q,\omega)}\right]\frac{1}{q}, \tag{14}$$

where E is the non-relativistic kinetic energy (i.e., $E = v^2/2$) and C_{ex} is the exchange correction factor given by

$$C_{ex} = 1 - \frac{q^2}{2E} + \left(\frac{q^2}{2E}\right)^2. \tag{15}$$

We calculated SPs of Al, Cu, Ag, and Au with the exchange correction from Eqs. (14) and (15) and compared the results with corresponding SPs calculated without the exchange correction. Fig. 10 shows plots of ratios of SPs with the exchange correction to those without this correction as a function of non-relativistic kinetic energy. We see that SPs with the exchange correction are smaller than those without the exchange correction for these four solids and energies between 10 eV and 30 keV. Above 100 eV, SPs with the exchange correction are smaller than those without the exchange correction by less than about 10%. The SP ratios generally increase with increasing electron energy, reaching about 0.95 at 30 keV.

The influence of electron exchange on calculated SPs is almost the same as that found in IMFP calculations for electron energies between 50 and 100 eV [26]. We note, however, that the Born–Ochkur approximation is essentially a high-energy approximation. It is then not clear whether this approximation is useful for evaluating the exchange correction for energies less than 100 eV.

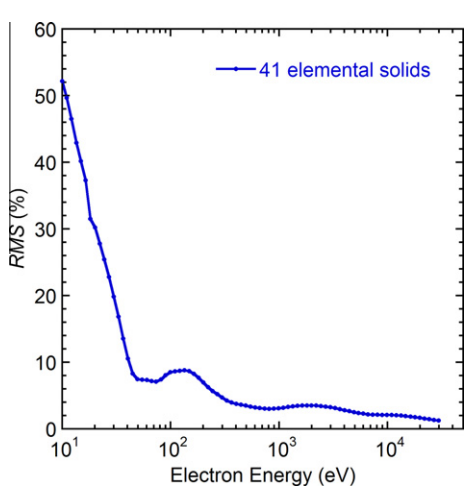

Fig. 9. The root-mean-square relative differences, *RMS*, of stopping powers calculated with the full Penn algorithm from stopping powers calculated with the single-pole approximation for the 41 elemental solids as a function of electron relativistic kinetic energy. The RMS differences were calculated from Eq. (13).

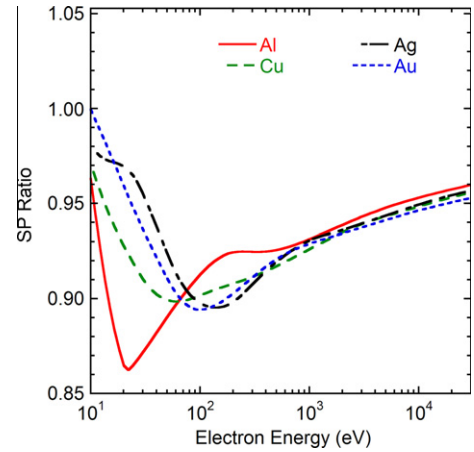

Fig. 10. Ratios of SPs calculated from the FPA with and without an exchange correction for Al, Cu, Ag, and Au as a function of non-relativistic electron kinetic energy (i.e., $E = v^2/2$).

4. Discussion

We will compare our calculated mass collision SPs with SPs from other calculations and from experiments. Although the FPA is expected only to provide a qualitative guide to SPs for energies less than about 50 eV, we show SPs calculated from the FPA for energies as low as 3 eV in Figs. 11–15 in order to make comparisons with available SP data.

4.1. Comparisons with calculated stopping powers

Mao et al. [21] calculated SPs of Al and Cu from 1 eV to 10 keV with the FPA. Fig. 11 shows comparisons of our SPs for Al and Cu calculated from the FPA and SPA with those of Mao et al. There is excellent agreement between our FPA SPs for Al and those of Mao et al. and satisfactory agreement for Cu. The slight differences for Cu at energies less than about 30 eV are probably due to the selection of different sets of optical ELF data in each calculation. As discussed in Section 3.3, the substantial differences in the SPs for Al from the FPA and SPA at energies less than 20 eV are associated with the contributions of single-electron excitations to the SP that occur at much lower energy losses than the relatively sharp plasmon peak at about 15 eV in the ELF. In contrast, there is broad structure in the Cu ELF, and a wide range of excitation energies contribute to the SP in the SPA calculation for Cu.

Fernandez-Varea et al. [42] calculated SPs for Al, Si, Cu, and Au for electron energies between 10 eV and 100 MeV. Their

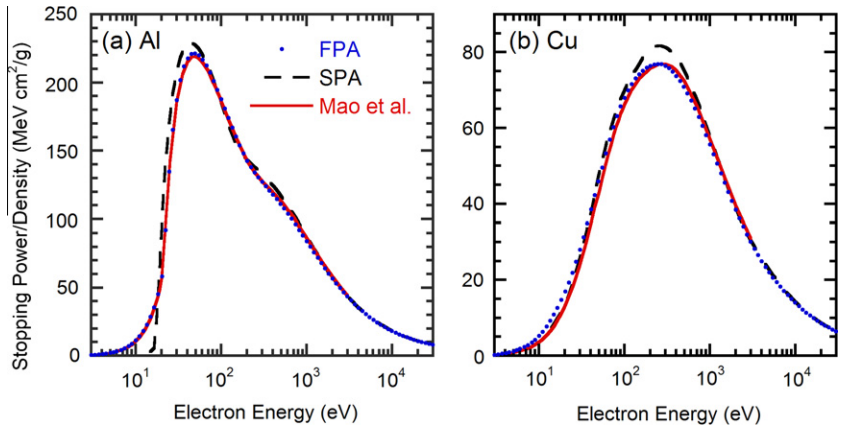

Fig. 11. Comparison of mass collision SPs calculated from optical data for (a) Al and (b) Cu with the full Penn algorithm by Mao et al. [21] (solid lines) as a function of electron relativistic kinetic energy with our SPs calculated with the single-pole approximation (long-dashed line) and the full Penn algorithm (solid circles).

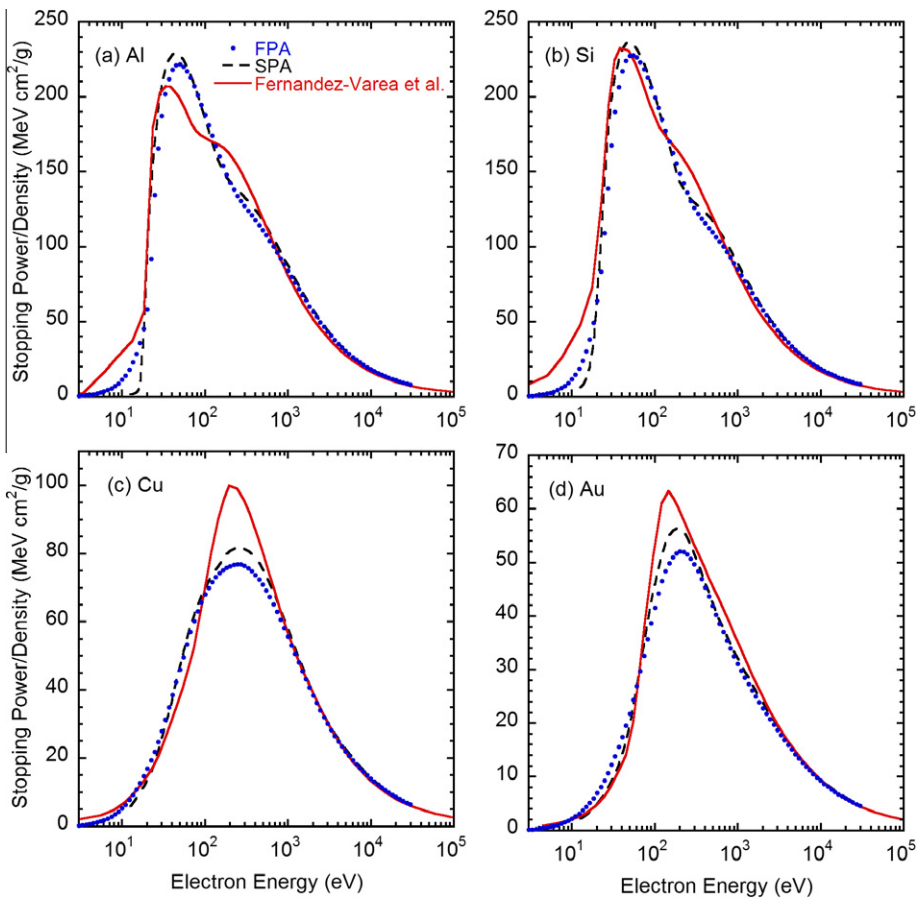

Fig. 12. Comparison of mass collision SPs calculated from optical data for (a) Al, (b) Si, (c) Cu, and (d) Au by Fernandez-Varea et al. [42] (solid lines) as a function of electron relativistic kinetic energy with our SPs that were obtained with the single-pole approximation (long-dashed line) and the full Penn algorithm (solid circles).

calculations were based on a so-called "N-oscillator" model in which different dispersion relations were applied for valence-electron excitations and inner-shell excitations. They also included a correction for electron exchange to cross sections for inner-shell excitations. We compare their SPs with our SPs from the FPA and SPA in Fig. 12. For energies over 1 keV, the SPs of Fernandez-Varea et al. for Al, Si, Cu, and Au are in excellent agreement with our values from the FPA. For Al and Si, there are differences in the shapes of the SP versus energy curves in the vicinity of 100 eV. These differences might be associated with the "switch energies" of 73 eV and 99 eV for Al and Si, respectively, used by Fernandez-Varea et al. to represent the demarcation between their models for valence-electron and inner-shell excitations. For Cu and Au, the switch energies are 74 eV and 54 eV, respectively, but there are no obvious changes of slope in the SP-versus-energy curves for these solids in Fig. 12. This difference from the Al and Si behavior occurs because the switch energies for Cu and Au occur in a structureless region of their ELFs. Tan et al. [43] reported SP

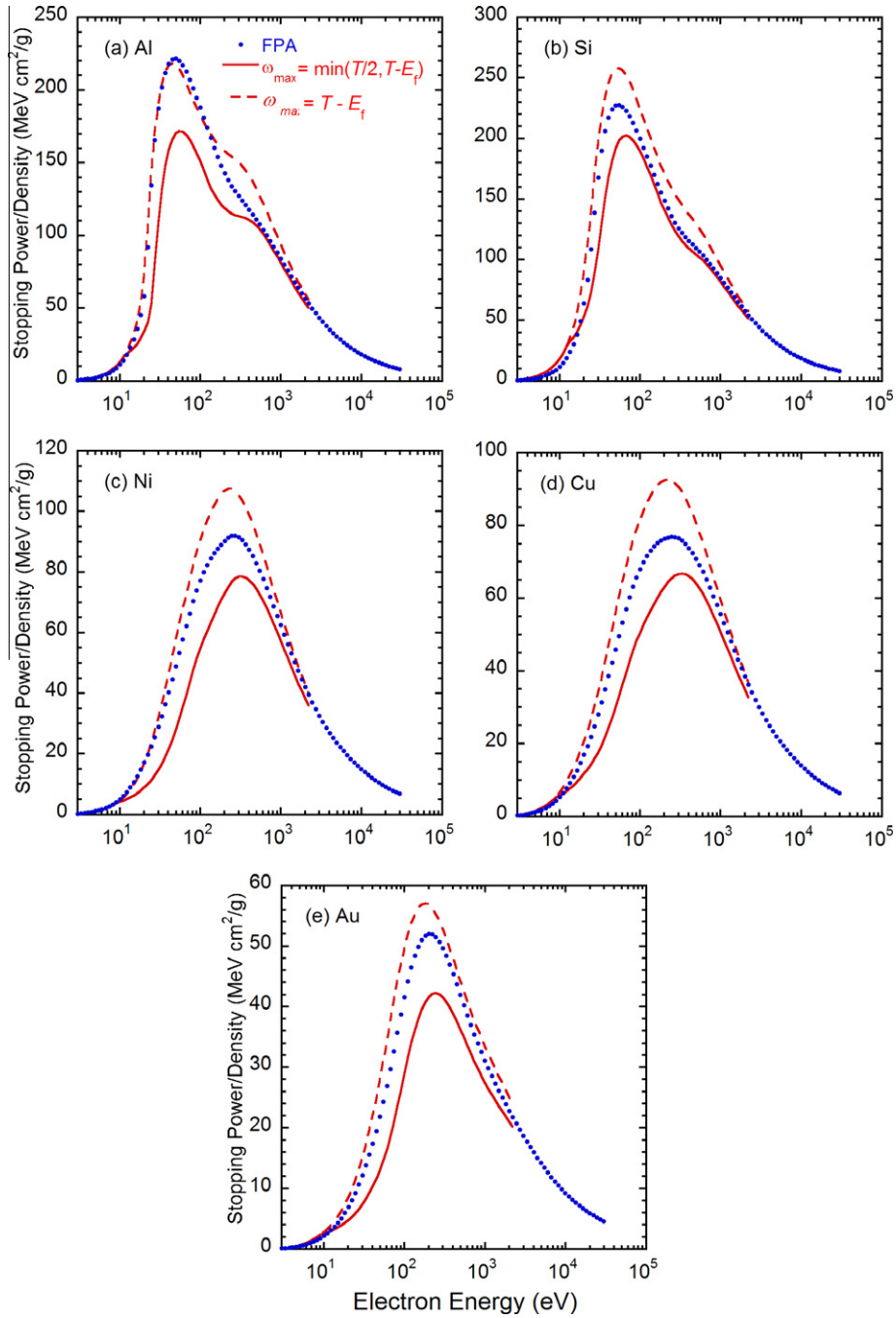

Fig. 13. Comparison of our mass collision SPs obtained from the full Penn algorithm (solid circles) as a function of relativistic kinetic energy for (a) Al, (b) Si, (c) Ni, (d) Cu, and (e) Au with SPs calculated from the Mermin-ELF model with $\omega_{\max} = \min(T/2, T - E_f)$ (solid lines) and with $\omega_{\max} = T - E_f$ (long-dashed lines).

calculations for a group of organic compounds with the SPA and two types of exchange correction [41,44]. They found that inclusion of exchange reduced their computed SPs by an average of 28%, 9%, and 9% for energies of 100 eV, 1 keV, and 10 keV, respectively. These differences are in good agreement with our estimates of electron exchange effect for SPs as shown in Fig. 10 except at 100 eV. Their calculations were done up to $\omega_{max} = T/2$ in Eq. (4). They must then obtain larger SPs at a low energy such as 100 eV if they used the same $\omega_{max}(= T - E_f)$ value as we used. We will refer later to this issue in comparison of SPs from the FPA and from the Mermin model. Nevertheless, the maximum SPs of Fernandez-Varea et al. (with an exchange correction) for Cu and Au are larger than our corresponding maximum SPs from the FPA (without an exchange correction). For Si and Al, however, there is close agreement in the maximum SPs from Fernandez-Varea et al. and our calculations with the FPA. It therefore appears that the exchange correction must be smaller than differences due to other factors (e.g., differences in optical ELFs and differences in the models). We have also pointed out in our related IMFP calculations that correlation and exchange should be treated in an integrated manner together with information on the band structure of the solid [6].

Abril et al. [45] proposed an algorithm for IMFP and SP calculations based largely on a Mermin-model dielectric function for the ELF (Mermin-ELF model) [46]. The Mermin function is an improvement over the Lindhard dielectric function used here in that it accounts for the finite lifetimes of the various excitations. Their

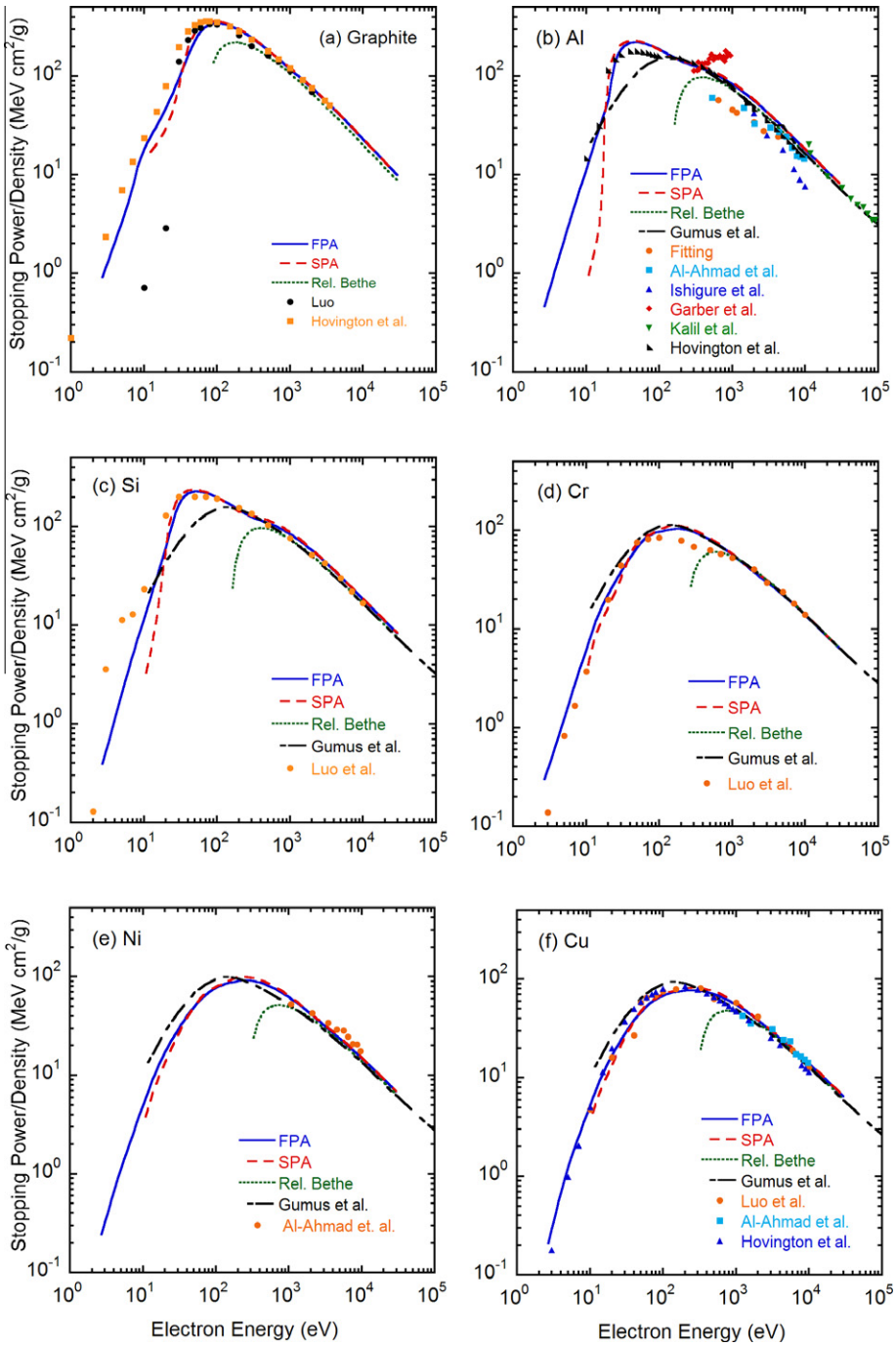

Fig. 14. Mass collision stopping powers for (a) graphite, (b) Al, (c) Si, (d) Cr, (e) Ni, and (f) Cu as a function of electron relativistic kinetic energy. The dotted lines show SPs from the relativistic Bethe formula (Eq. (12)), and the solid and long-dashed lines show our SPs from the full Penn algorithm and the single-pole approximation, respectively. The long-short dashed lines show SPs calculated from a modified Bethe-Bloch SP equation and expressions for the effective atomic electron number and the effective mean excitation energies [51]. The symbols indicated SPs derived from the experiments of Luo et al. [53] (for Si, Cr, and Cu), Luo [54] (for graphite), Hovington et al. [55] (for graphite, Al, and Cu), Kalil et al. [57] (for Al), Al-Ahmad and Watt [58] (for Al, Ni, and Cu), Garber et al. [59] (for Al), Fitting [60] (for Al), and Ishigure et al. [61] (for Al).

model of Mermin energy-loss functions was combined with generalized oscillator strengths (MELF-GOSs) to fit experimental ELF data. The part of an experimental ELF ascribed to excitations of outer-shell electrons was fitted with a linear combination of Mermin-type ELFs, and the part associated with excitations of inner-shell electrons was fitted with hydrogenic generalized oscillator strengths [47].

We have calculated SPs for Al, Si, Ni, Cu, and Au with the Mermin-ELF model using the parameters for outer-electron excitations given in Table 1 of Ref. [48] for Al, Si, Ni, and Cu and Table 1 of Ref. [49] for Au; these parameters were determined from fits to optical ELFs for excitation energies up to about 1 keV and thus include the contributions of several inner shells. In our calculations we ignored the contributions of GOSs for inner-shell ionization of the K shells of Al and Si, of the K and L shells of Ni and Cu, and of the K, L, and M shells of Au. We estimated their contribution to be less than a few percent for electron energies less than 2 keV for Ni and Cu and less than 10 keV for Al, Si, and Au.

Fig. 13 shows comparisons between SPs from the FPA (solid symbols) and from the Mermin-ELF model (solid and dashed lines)

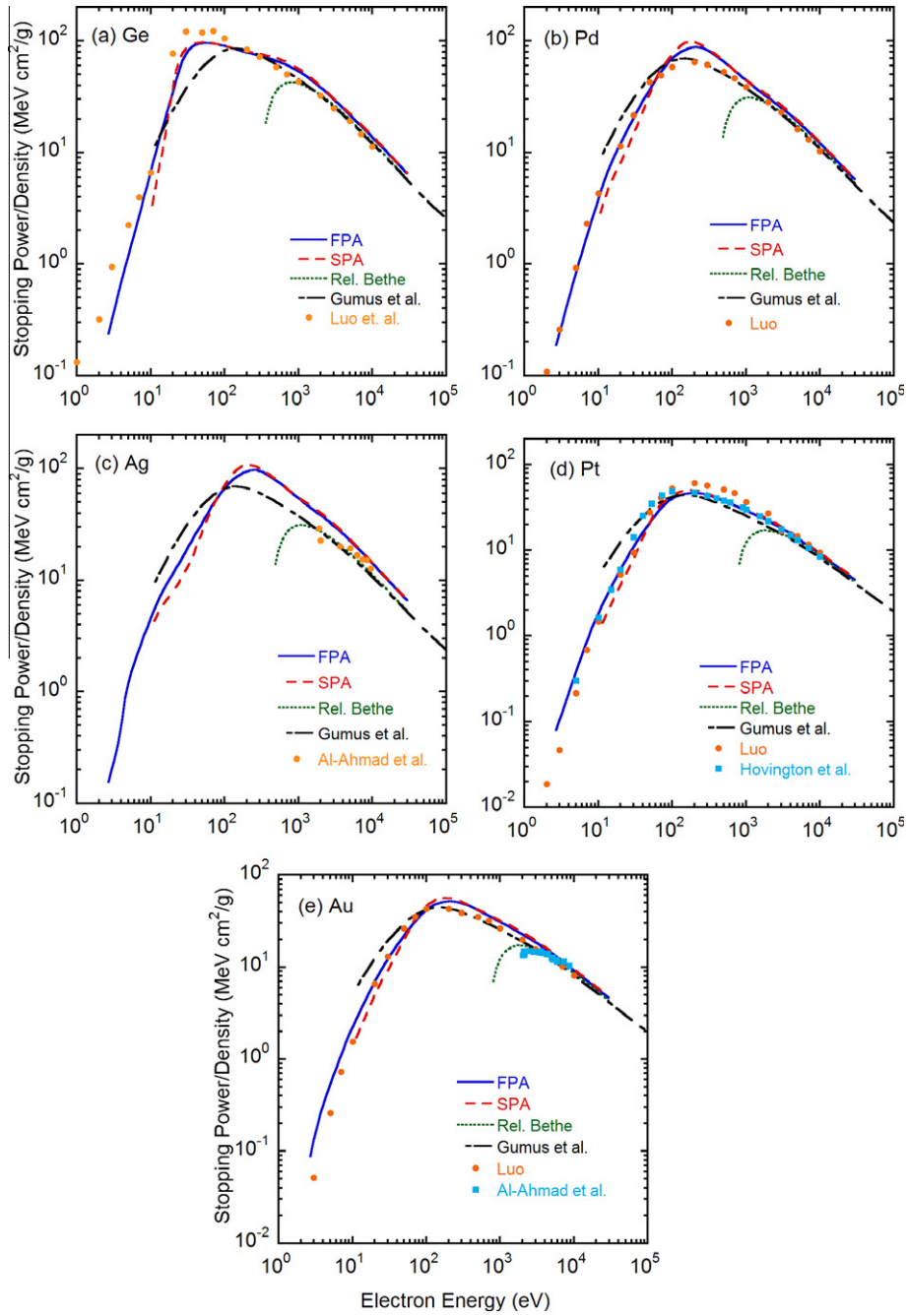

Fig. 15. Mass collision stopping powers for (a) Ge, (b) Pd, (c) Ag, (d) Pt, and (e) Au as a function of electron relativistic kinetic energy. The dotted lines shows SPs from the relativistic Bethe formula (Eq. (12)), and the solid and long-dashed lines show our SPs from the full Penn algorithm and the single-pole approximation, respectively. The long-short dashed lines show SPs calculated from a modified Bethe–Bloch SP equation and expressions for the effective atomic electron number and the effective mean excitation energies [51]. The symbols indicated SPs derived from the experiments of Luo et al. [53] (for Ge), Luo [54] (for Pd, Pt, and Au), Hovington et al. [55] (for Pt), and Al-Ahmad and Watt [58] for Ag and Au).

for Al, Si, Ni, Cu, and Au using two choices for the upper limit $\omega_{\max}$ for excitation energy in the latter SP calculations. One value of $\omega_{\max}$ was $\omega_{\max} = \min(T/2, T - E_f)$, as recommended by Denton et al. [50], while the other was $\omega_{\max} = T - E_f$ as chosen here for evaluation of Eq. (2). Denton et al. chose the former limit to avoid consideration of secondary electrons having energies larger than inelastically-scattered primary electrons. Larger energy transfers are possible, however, although secondary electrons may then be indistinguishable from scattered primary electrons, either in experiments or in model calculations of electron energy spectra. We believe that the upper limit $\omega_{\max} = T - E_f$ is more appropriate for the SP calculation, as we have chosen here for the results in Figs. 1–7.

Fig. 13 indicates that SPs from the FPA are smaller than those from the Mermin-ELF model with the same upper limit $\omega_{\max} = T - E_f$ for Si, Ni, Cu, and Au. These differences are generally less than 20% for energies over 50 eV and may be associated with different q-dependences of the ELF in the two models. For Al, SPs from the Mermin-ELF model (with $\omega_{\max} = T - E_f$) and from the FPA are in good agreement for energies less than 200 eV. This agreement, in contrast to the results for Si, Ni, Cu, and Au, may be fortuitous because of the relatively poorer fit for Al of the

Mermin-ELF to the optical ELF (particularly around the volume-plasmon energy-loss peak between 12 and 17 eV) than for the other four solids.

Fig. 13 also shows that calculated SPs from the FPA are larger by up to about 250% than those from the Mermin-ELF model with $\omega_{\max} = \min(T/2, T - E_f)$ for energies between 20 eV and 1 keV. For energies above 1 keV, there is generally good agreement between SPs from the two approaches. In contrast, we previously found much better agreement between IMFPs calculated with the FPA for Al and Au [6] and those reported by Denton et al. [50] who used the Mermin-ELF model with the same parameters as those given in Refs. [48] and [49]. This observation suggests that choice of the upper limit ω_{max} is more significant in SP calculations than in IMFP calculations because of the greater relative contributions of possible large-energy-loss excitations to the SP [the factor ω in Eq. (4)] than to the IMFP. Fig. 13 indicates that the choice of the upper limit is most important for electron energies between about 20 eV and about 1 keV.

Gumus et al. [51] calculated SPs for Al, Si, Cr, Ni, Cu, Ge, Pd, Ag, Pt, and Au for electron energies between 10 eV and 100 MeV. Their calculations were performed using a modified Bethe–Bloch SP expression and analytical expressions for the effective atomic number and the effective mean excitation energy of each material. We show their SPs in Figs. 14 and 15 together with our SPs (and the experimental SPs discussed in the next section). For energies over 200 eV, the SPs of Gumus et al. for Al, Si, Cr, Cu, Ge, and Pt, are in good agreement with our values from the FPA and SPA. We also see that the SPs of Gumus et al. for the other solids are smaller than our SPs from the FPA for energies above 200 eV. For energies between 10 and 200 eV, the SPs of Gumus et al. for Al, Si, and Ge are smaller than our SPs while they obtain larger SPs for the other solids. Except for Ag, there is generally good agreement between the Gumus et al. SPs and our SPs from the FPA and SPA for energies over 200 eV. Since their calculations were made with a modified Bethe formula that is usually applied for much higher energies, 200 eV must be an effective low-energy limit for their approach.

For Ag, there are larger differences between our SPs from the FPA and those of Gumus et al. at energies above 200 eV, as stated above. Since the SPs of Ag for Gumus et al. are in good agreement with SPs from the relativistic Bethe formula (Eq. (12)) for energies above 5 keV, the differences with our SPs might be due to uncertainties in the experimental ELF data for Ag (despite relatively small errors in the f-sum and KK-sum rules [6]).

4.2. Comparison with experimental stopping powers

We compare calculated SPs from the FPA for graphite, Al, Si, Cr, Ni, Cu, Ge, Pd, Ag, Pt, and Au in Figs. 14 and 15 with experimental SP data that were mostly obtained from Joy's database [52]. We previously made similar comparisons of SPs from the SPA for Al, Si, Cr, Ni, Cu, Ge, Pd, Ag, Pt, and Au and for electron energies between 100 eV and 30 keV [1]. We will therefore emphasize comparisons here between SPs from the FPA and measured SPs as well as comparisons for energies less than 100 eV. Comparisons will also be made with SPs from the relativistic Bethe equation (Eq. (12)) using MEEs listed in Table 4.3 of Ref. [7] except graphite. The MEE value for graphite was obtained from our previous work [2]. We also show SPs from the SPA in Figs. 14 and 15 so that similarities and differences with the FPA results are visible.

The experimental SPs in Figs. 14 and 15 can be classified into two groups. Almost all of the experimental SPs for energies less than 1 keV were reported by Luo et al. [53], Luo [54], and Hovington et al. [55,56]. These SPs are based on measurements of transmission electron energy-loss spectra of 100 or 200 keV electrons transmitted through thin specimen films. The energy-loss spectra for energy losses up to 1 keV and for the angular acceptance of their spectrometer were analyzed to obtain the single-scattering ELF. These ELFs were extended to larger energy losses using atomic X-ray absorption data. Checks were made to ensure that the ELFs satisfied the expected sum rules. SPs were then calculated from the experimental ELFs without consideration of any q-dependence other than that expected from the scattering kinematics. Their SP calculation, although derived from experimental ELFs, is very similar in principle to our SP calculation from optical ELFs. The other group of measured SPs in Figs. 14 and 15 was obtained from calorimetric methods for Al, Ni, Cu, Ag, and Au [57,58], from a novel thin-film method in which currents to electrodes at the top and bottom surfaces of a film were measured (and with the electrodes separated from the film by thin insulating layers) for Al [59], from analyses of energy distributions of electrons transmitted through a thin Al film with a retarding-field analyzer [60], and from analyses of energy distributions of electrons transmitted through a thin Al film at various scattering angles [61].

We see generally excellent agreement between our SPs from the FPA and the Joy SPs for energies larger than about 10 eV and in some cases (Cu, Pd, and Pt) for lower energies. However, the excellent agreement at energies near 10 eV is very likely fortuitous because our SP calculations with the FPA ignored the effects of electron exchange and correlation that must be important at such low energies. Some small but systematic differences are found at energies between 10 and 100 eV for graphite, Al, Si, and Ge, and similar differences can be seen for larger energies for Cr, Pd, Pt, and Au. Generally good agreement is found between our SPs from the FPA and the SPs measured by calorimetry for Al, Ni, Cu, Ag, and Au for energies between about 4 and 30 keV, but there are disagreements between our SPs and those of Al-Ahmad and Watt [58] for Al, Ag, and Au at lower energies.

The comparisons in Fig. 14 for Al show a wide spread in measured SPs for the same material as measured by different methods. The measured SPs at a given energy can differ by a factor of more than two, and the energy dependence of the SPs reported by Garber et al. [59] differs from those obtained by other methods (including the FPA). Given this disparity in SP results for a single material, we believe that there is satisfactory agreement between SPs from the FPA and the measured SPs. Definitive experimental tests are still required, however, to determine whether and how any exchange correction should be included in the SP calculation, as discussed in Sections 3.4 and 4.1. Further experimental tests are also required to distinguish differences in SPs corresponding to different choices of the upper limit ω_{max} in Eq. (4), as discussed in Section 4.1.

We note that there is good agreement between SPs from the FPA and SPA in Figs. 14 and 15 for all solids except Al, Si, and Ge at energies less than 20 eV. These solids have strong and narrow plasmon peaks in their energy-loss spectra. As discussed in Sections 3.3 and 4.1, substantial differences can occur for such solids between SPs determined from the FPA and SPA because SPs from the SPA do not have contributions from single-electron excitations.

Finally, we see satisfactory agreement in Figs. 14 and 15 between SPs from the relativistic Bethe equation (Eq. (12)), SPs calculated from the FPA, and most measured SPs for energies larger than about 5 keV for low-Z and most medium-Z elements (graphite, Al, Si, Cr, Ni, Cu, Ge, and Pd) and for energies larger than about 10 keV for high-Z elements (Pt and Au). For Ag, however, there are larger differences between SPs from the FPA and those from Eq. (12) at energies above 5 keV than for the other solids. These differences might be due to uncertainties in the experimental ELF data for Ag [6].

5. Summary

We have reported mass collision electron SPs for Li, Be, graphite, diamond, glassy C, Na, Mg, Al, Si, K, Sc, Ti, V, Cr, Fe, Co, Ni, Cu, Ge, Y,

Nb, Mo, Ru, Rh, Pd, Ag, In, Sn, Cs, Gd, Tb, Dy, Hf, Ta, W, Re, Os, Ir, Pt, Au, and Bi over the 50 eV to 30 keV energy range. These SPs were calculated from ELFs determined from experimental optical data or ELF measurements [6] with the full Penn algorithm [4]. For 19 of our 41 solids, we adopted improved sets of optical ELF data [6] over those used for our previous SP calculations with the single-pole approximation or simple Penn algorithm [1,2]. The largest changes occurred for Pd (where the SP increased by up to 58%), V (where the SP increased by up to 52%), and Re (where the SP decreased by up to 26%).

We made comparisons of RMS differences between SPs calculated from the FPA and SPA using the same ELF data sets for the calculations with each algorithm. For energies above 50 eV, the RMS relative differences were less than 10% and generally decreased with increasing energy, reaching 1% at 30 keV.

We compared our calculated SPs with results from other calculations. Mao et al. [21] calculated SPs of Al and Cu from 1 eV to 10 keV with the FPA. There was excellent agreement between our SPs from the FPA for Al and those of Mao et al. and satisfactory agreement for Cu. Fernandez-Varea et al. [42] calculated SPs of Al, Si, Cu, and Au for electron energies between 10 eV and 100 MeV with their N-oscillator model. For energies over 1 keV, the SPs of Fernandez-Varea et al. for Al, Si, Cu, and Au were in excellent agreement with our values from the FPA. For Al and Si, there were differences in the shapes of the SP-versus-energy curves in the vicinity of 100 eV. These differences might be associated with the "switch energies" of 73 and 99 eV for Al and Si, respectively, used by Fernandez-Varea et al. to represent the demarcation between their models for valence-electron and inner-shell excitations. Their maximum values of the SPs for Al and Si were in reasonable agreement with our maximum values, but their maximum values for Cu and Au were larger than our maximum values.

Abril et al. [45] developed an algorithm for IMFP and SP calculations based on a Mermin-model dielectric function (Mermin-ELF model) [46]. We calculated SPs for Al, Si, Ni, Cu, and Au with the Mermin-ELF model using the parameters for outer-electron excitations adopted by the Abril group [48,49]. These calculations were performed with two choices for the upper limit $\omega_{\max}$ for excitation energy, one being $\omega_{\max} = \min(T/2, T - E_f)$, as recommended by Denton et al. [50], while the other was $\omega_{\max} = T - E_f$ as chosen here for our SP calculations. The differences between SPs with the latter choice of $\omega_{\max}$ and our SPs from the FPA were generally less than 20% for Si, Ni, Cu, and Au at energies above 50 eV and for Al at energies above 200 eV. In similar comparisons of SPs with the former choice of ω_{max}, our SPs were larger than those from the Mermin-ELF model by up to 250% for energies between 20 eV and 1 keV. There was, however, good agreement for energies less than 20 eV for Al, Si, Cu, and Au or less than 10 eV for Ni and greater than 1 keV for the five solids. We believe that $\omega_{\max} = T - E_f$ is the more appropriate choice for the upper limit.

We compared our SPs calculated from the FPA for graphite, Al, Si, Cr, Ni, Cu, Ge, Pd, Ag, Pt, and Au with values derived from available experimental data. Most of these comparisons were made with SPs derived by Joy et al. [52–56] from ELFs obtained from analyses of energy-loss spectra measured by transmission of 100 or 200 keV electrons through thin specimen films. We found generally excellent agreement between SPs derived in this way and our SPs from the FPA for energies larger than about 10 eV, although there were small but systematic differences for some solids between 10 and 100 eV. There was satisfactory agreement between our calculated SPs and values determined from calorimetry experiments for Al, Ni, Cu, Ag, and Au [57,58] at energies between 4 keV and 30 keV, but there were disagreements with the experimental SPs for Al, Ag, and Au [58] at lower energies. SPs have been measured by other methods for only one material (Al) [59–61], but the reported SPs at a particular energy can differ by a factor of more than two.

Finally, we compared our calculated SPs with values from the relativistic Bethe equation with recommended mean excitation energies derived from a wide variety of experimental data [7] and from our previous analysis for the three carbon allotropes [2]. The RMS relative deviations between our calculated SPs and values from the Bethe equation were 9.1% and 8.7% for energies of 9.897 and 29.733 keV, respectively. Satisfactory agreement was found between SPs from the Bethe equation, our SPs, and most measured SPs for energies larger than about 5 keV for low-*Z* and most medium-*Z* elements (graphite, Al, Si, Cr, Ni, Cu, Ge, and Pd) and for energies larger than about 10 keV for high-Z elements (Pt and Au). Larger differences between SPs from the Bethe equation and from the FPA were found for Ag at energies above 5 keV, presumably due to uncertainties in the experimental ELF data set for Ag.

Acknowledgments

We thank Drs. Z.-J. Ding and J. M. Fernandez-Varea for supplying numerical data and Drs. I. Abril and C. D. Denton for useful comments and discussions.

References

[1] S. Tanuma, C.J. Powell, D.R. Penn, Surf. Interface Anal. 37 (2005) 978.
[2] S. Tanuma, C.J. Powell, D.R. Penn, J. Appl. Phys. 103 (2008) 063707.
[3] J. Lindhard, K. Dan, Vidensk. Selsk. Mat.-Fys. Medd. 28 (8) (1954) 1.
[4] D.R. Penn, Phys. Rev. B 35 (1987) 482.
[5] S. Tanuma, C.J. Powell, D.R. Penn, Surf. Interface Anal. 17 (1991) 911.
[6] S. Tanuma, C.J. Powell, D.R. Penn, Surf. Interface Anal. 43 (2011) 689.
[7] M.J. Berger, M. Inokuti, H.H. Anderson, H. Bichsel, J.A. Dennis, D. Power, S.M. Seltzer, J.E. Turner. Stopping Powers for Electrons and Positrons, ICRU Report 37, International Commission on Radiation Units and Measurements, Bethesda, 1984.
[8] R. Gauvin, Surf. Interface Anal. 37 (2005) 875.
[9] N.W.M. Ritchie, Surf. Interface Anal. 37 (2005) 1006.
[10] F. Salvat, X. Llovet, J.M. Fernandez-Varea, J. Sempau, Surf. Interface Anal. 37 (2005) 1054.
[11] A. Jablonski, C.J. Powell, S. Tanuma, Surf. Interface Anal. 37 (2005) 861.
[12] A. Jablonski, C.J. Powell, Surf. Sci. 604 (2010) 1928.
[13] J.S. Villarrubia, A.E. Vladar, M.T. Postek, Surf. Interface Anal. 37 (2005) 951.
[14] H. Bethe, Ann. Physik (Leipzig) 5 (1930) 325.
[15] H. Bethe, Handbuch der Physik, in: H. Geiger, K. Scheel (Eds.), vol. 24/1, Springer, Berlin, 1933, p. 273.
[16] H.A. Bethe J. Ashkin, Experimental Nuclear Physics, in: E. Segre (Ed.), Wiley, New York, 1953, p. 166.
[17] M.J. Berger, J.S. Coursey, M.A. Zucker, J. Chang, Stopping Power and Range Tables for Electrons, Positrons, and Helium Ions, version 1.2.3, <http://www.nist.gov/pml/data/star/index.cfm>, 2005.
[18] J.M. Fernandez-Varea, D. Liljequist, S. Csillag, R. Raty, F. Salvat, Nucl. Instrum. Methods Phys. Res. B 108 (1996) 35.
[19] U. Fano, Ann. Rev. Nucl. Sci. 13 (1963) 1.
[20] M. Dapor, Electron-Beam Interactions with Solids, Springer, Berlin, 2003.
[21] S.F. Mao, Y.G. Li, R.G. Zeng, Z.J. Ding, J. Appl. Phys. 104 (2008) 114907.
[22] K.O. Jensen, A.B. Walker, Surf. Sci. 292 (1993) 83.
[23] S. Tanuma, T. Shiratori, T. Kimura, K. Goto, S. Ichimura, C.J. Powell, Surf. Interface Anal. 37 (2005) 833.
[24] W.S.M. Werner, C. Tomastik, T. Cabela, G. Richter, H. Störi, Surf. Sci. 470 (2000) L123.
[25] W.S.M. Werner, C. Tomastik, T. Cabela, G. Richter, H. Störi, J. Electron Spectrosc. Relat. Phenom. 113 (2001) 127.
[26] C.J. Powell, A. Jablonski, J. Phys. Chem. Ref. Data 28 (1999) 19.
[27] K. Kumagai, S. Tanuma, C.J. Powell, Nucl. Instrum. Methods Phys. Res. B 267 (2009) 167.
[28] B.L. Henke, J.C. Davis, E.M. Gullikson, R.C.C. Perera, Lawrence Berkeley Laboratory Report 26259 (1988);
B.L. Henke, E.M. Gullikson, J.C. Davis, At. Data Nucl. Data Tables 54 (1993) 181.
[29] S. Tanuma, C.J. Powell, D.R. Penn, Surf. Interface Anal. 11 (1988) 577.
[30] W.S.M. Werner, K. Glantschnig, C. Ambrosch-Draxl, J. Phys. Chem. Ref. Data. 38 (2009) 1013.
[31] J.L. Robins, J.B. Swan, Proc. Phys. Soc. (London) 76 (1960) 857.
[32] E.D. Palik (Ed.), Handbook of Optical Constants of Solids, Academic Press, New York, 1985.
[33] H.-J. Hagemann, W. Gudat, and C. Kunz, Deutsches Elektronen-Synchrotron Report SR-74/7, Hamburg, 1974, (unpublished).;
H.–J. Hagemann, W. Gudat, C. Kunz, J. Opt. Soc. Am. 65 (1975) 742.

[34] E.D. Palik (Ed.), Handbook of Optical Constants of Solids II, Academic Press, New York, 1991.
[35] C.C. Ahn (Ed.), Transmission Electron Energy Loss Spectrometry in Materials Science and the EELS ATLAS, Wiley-VCH, Germany, 2004.
[36] D.Y. Smith, Handbook of Optical Constants of Solids in: E.D. Palik (Ed.), Academic Press, New York, 1985, p. 210.
[37] G.D. Mahan, Many-Particle Physics, Plenum, New York, 2000. p. 358.
[38] S. Tanuma, C.J. Powell, D.R. Penn, Surf. Interface Anal. 17 (1991) 929.
[39] S. Tanuma, C.J. Powell, D.R. Penn, J. Electron Spectrosc. Relat. Phenom. 62 (1993) 95.
[40] V.I. Ochkur, Sov. Phys. JETP 18 (1964) 503.
[41] J.M. Fernandez-Varea, R. Mayol, D. Liljequist, F. Salvat, J. Phys.: Condens. Matter. 5 (1993) 3593.
[42] J.M. Fernandez-Varea, F. Salvat, M. Dingfelder, D. Liljequist, Nucl. Instrum. Methods Phys. Res. B 229 (2005) 187.
[43] Z. Tan, Y. Xia, M. Zhao, X. Liu, F. Li, B. Huang, Y. Ji, Nucl. Instrum. Methods Phys. Res. B 222 (2005) 47.
[44] J.C. Ashley, V.E. Anderson, J. Electron Spectrosc. Relat.Phenom. 24 (1981) 127.
[45] I. Abril, R. Garcia-Molina, C.D. Denton, F.J. Pérez-Pérez, N.R. Arista, Phys. Rev. A 58 (1998) 357.
[46] N.D. Mermin, Phys. Rev. B 1 (1970) 2362.
[47] R.F. Egerton, Electron Energy Loss Spectroscopy in the Electron Microscope, Plenum Press, New York, 1989.
[48] C.D. Denton, I. Abril, J.C. Moreno-Marín, S. Heredia-Avalos, R. Garcia-Molina, Phys. Stat. Sol. (b) 245 (2008) 1498.
[49] S. Heredia-Avalos, I. Abril, C.D. Denton, J.C. Moreno-Marín, R. Garcia-Molina, J. Phys.: Condens. Matter. 19 (2007) 466205.
[50] C.D. Denton, I. Abril, R. Garcia-Molina, J.C. Moreno-Marin, S. Heredia-Avalos, Surf. Interface Anal. 40 (2008) 1481.
[51] H. Hasan Gumus, O. Kabadayi, Vacuum 85 (2010) 245.
[52] D.C. Joy, http://web.utk.edu/~srcutk/htm/interact.htm, April, 2008.
[53] S. Luo, X. Zhang, D.C. Joy, Rad. Eff. Defects Solids 117 (1991) 235.
[54] S. Luo, Study of Electron-Solid Interactions, PhD Thesis, University of Tennessee, May, 1994.
[55] P. Hovington, D. C. Joy, R. Gauvin, and N. Evans, unpublished data summarized in Ref. [56].
[56] D.C. Joy, S. Luo, R. Gauvin, P. Hovington, N. Evans, Scanning Microsc. 10 (1996) 653.
[57] F. Kalil, W.G. Stone, H.H. Hubell, R.D. Birkhoff, Oak Ridge National Laboratory Report 2731 (1959).
[58] K.O. Al-Ahmad, R.E. Watt, J. Phys. D: Appl. Phys. 16 (1983) 2257.
[59] F.W. Garber, M.Y. Nakai, J.A. Harter, R.D. Birkhoff, J. Appl. Phys. 42 (1971) 1149.
[60] H.-J. Fitting, Phys. Stat. Sol. (a) 26 (1974) 525.
[61] N. Ishigure, C. Mori, T. Watanabe, J. Phys. Soc. Japan. 44 (1978) 973.

Ultramicroscopy 112 (2012) 53–60

Contents lists available at SciVerse ScienceDirect

Ultramicroscopy

journal homepage: www.elsevier.com/locate/ultramic

Imaging properties of bright-field and annular-dark-field scanning confocal electron microscopy: II. Point spread function analysis

K. Mitsuishi [a,*], A. Hashimoto [a], M. Takeguchi [a], M. Shimojo [b], K. Ishizuka [a,c]

[a] Surface Physics and Structure Unit, National Institute for Materials Science, 1-2-1 Sengen, Tsukuba 305-0047, Japan
[b] Department of Materials Science and Engineering, Shibaura Institute of Technology, 3-7-5 Toyosu, Koto-ku, Tokyo 135-8548, Japan
[c] HREM Research Inc., 14-48 Matsukazedai, Higashimatsuyama, Saitama 355-0055, Japan

ARTICLE INFO

Article history:
Received 8 June 2011
Received in revised form
30 September 2011
Accepted 14 October 2011
Available online 25 October 2011

Keywords:
Scanning confocal electron microscopy
SCEM
Point spread function
Contrast transfer function
PSF
CTF
Optical sectioning
Multislice method
Image simulation

ABSTRACT

The imaging properties of bright field and annular dark field scanning confocal electron microscopy (BF-SCEM and ADF-SCEM) are discussed based on their point spread functions (PSFs) in comparison with multislice simulations. Although the PSFs of BF-SCEM and ADF-SCEM show similar hourglass shapes, their numerical distributions are quite different: BF-SCEM PSF is always positive and shows a center of symmetry whereas the ADF-SCEM PSF is complex and has Hermitian symmetry. These PSF properties explain the large elongation effect in BF-SCEM for laterally extended object and almost no-elongation in ADF-SCEM, illustrating the importance of the numerical analysis of PSFs. The Hermitian symmetry of the ADF-SCEM PSF results in an interesting "edge enhancement effect" at the interface. Simulation using the PSF and the multislice method verified this effect at GaAs surfaces and InAs interfaces embedded in GaAs. This unique feature of ADF-SCEM can potentially be useful for depth sectioning. It is also pointed out that a PSF imaging model cannot be applicable for BF-SCEM of a phase object, when the system is symmetric and aberration free.

1. Introduction

Scanning confocal electron microscopy (SCEM) [1,2] is the electron version of the well-established optical three-dimensional imaging technique, scanning confocal optical microscopy (SCOM) [3,4] and was firstly reported in 2002 [2]. The schematic of the system is depicted in Fig. 1. The SCEM ray path consists of scanning transmission electron microscopy (STEM) illumination system and transmission electron microscopy (TEM) imaging system with pin-hole aperture placed at the detector. The image is formed by scanning the focused probe over the sample and by de-scanning the probe image on the detector. The original report [2] demonstrated an image improvement for thick semiconductor device by SCEM in comparison with STEM or TEM.

Takeguchi et al. [5] and Hashimoto et al. [6] developed a stage-scan system that forms an image by scanning the sample instead of scanning the beam. This system avoids the difficulties associated with beam scanning such as adjusting the probe positions on the sample and detector during the scan and de-scan, which is a technically very demanding task especially at high-resolution. Using the stage scan system they obtained for the first time high-resolution SCEM images from Au particles.

However, the depth sectioning (*z*-sectioning) capability of a sample has not been achieved by usual SCEM yet partially because in comparison with optical lenses used in SCOM, the available numerical aperture size is much smaller for the SCEM due to the aberrations in magnetic lenses used in SCEM. Recent progress of aberration correctors is now improving this situation rapidly [7–9].

A more intrinsic problem of *z*-sectioning with SCEM is, as pointed by many authors [10–12] including our previous paper [13], conventional bright field (BF)-SCEM is susceptible to the elongation effect depending on the sample lateral size, and thus the depth resolution is much worse than the vertical spread of the focused probe. Note that the point spread functions of aberration free BF-SCEM is the same with for high-angle annular dark field (HAADF)-STEM [10–12,14,15]. Therefore, the depth resolution achievable with BF-SCEM is the same with HAADF-STEM.

On the other hand, annular dark field (ADF)-SCEM, recently suggested SCEM technique that uses annular dark field aperture placed at the collector lens (Fig. 1(b)), shows more readily interpretable image contrast. Depth sectioned images of a nano-coil were obtained with ADF-SCEM using an uncorrected microscope, and no obvious elongation effects due to the sample lateral

* Corresponding author. Tel.: +81 29 863 5474; fax: +81 863 5571.
E-mail address: Mitsuishi.Kazutaka@nims.go.jp (K. Mitsuishi).

0304-3991/$ - see front matter © 2011 Elsevier B.V. All rights reserved.
doi:10.1016/j.ultramic.2011.10.004

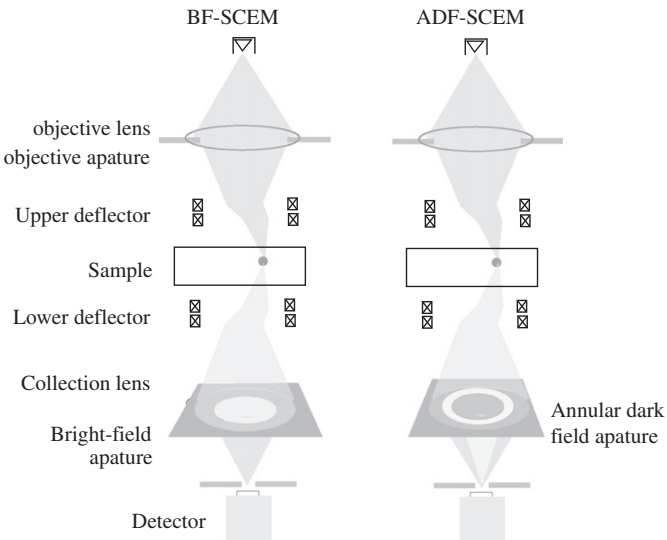

Fig. 1. Schematic drawing of BF and ADF-SCEM setups. The sample is illuminated by an electron beam, which is focused by the objective lens and scanned by the upper deflection coils. The transmitted beam is de-scanned by the lower deflection coils and re-focused by the collector lens on the detector. The detector pin-hole aperture selects only electrons passing through the focus. A BF or ADF aperture is applied at the collector lens.

size were observed [16,17]. In the previous paper, we provided a geometrical explanation of the image features observed in BF and ADF-SCEM [13]. It was demonstrated that the BF-SCEM intensity profile consists of broad and sharp features originated from the sample shape and atomic structure close to the probe focus, respectively.

The properties of imaging system are often discussed using the contrast transfer function (CTF), and the boundaries of the CTF are used to discuss the limit of frequency transfer. However, since CTF is an expression in reciprocal space, it is difficult to predict the imaging property in real space. Furthermore, the values of the CTF within the boundary are equally important for imaging.

In this paper, we illustrate the properties of BF and ADF-SCEM using the point spread function (PSF) and CTF and explain some unusual features of ADF-SCEM that can be explained by taking account of the value of PSF. To accentuate the imaging nature of BF and ADF-SCEM, we only discuss the case of aberration free system. This assumption may be justified by the recent developments of electron microscopes equipped with double (objective and collector lenses) aberration correctors that is capable of opening up the aperture as wide as a few 10 mrad and potentially realize a nanometer resolution in the z-direction.

2. Calculations conditions

Throughout this paper, the objective semiangles are 30 mrad for both BF and ADF-SCEM and the collection semiangles are 30 mrad for BF and 30 to 40 mrad for ADF-SCEM. The PSFs are calculated for the region of 2.56 nm × 2.56 nm × 25.6 nm divided by 512 × 512 × 512. Dynamical calculations were performed using the FFT-multislice method [18] implemented into the EMS software [19], which was modified for SCEM simulations. The incident energy was 200 keV. All aberrations but defocus were ignored and a point detector was assumed. Both BF and ADF intensities at the point detector were normalized at each illumination angle by the BF intensities without a sample. The supercell of 9.60 × 9.58 nm was used for GaAs/InAs where 1024 × 1024 waves were calculated; this corresponds to 17 × 24 unit cells of GaAs(110). The lattice constant was assumed to be the same for InAs and GaAs. All absorption has been neglected, although the elastic potential was smeared through the use of the Debye–Waller factors.

3. Imaging model of HAADF-STEM and SCEM

In this and following sections we restrict the discussion of SCEM to coherent scattering by a weak scattering object and neglect multiple scattering. In this case the image amplitude may be expressed by a convolution between an object distribution and a PSF, which describes the system response to a point object. Then, a Fourier transform of the image amplitude is given by a simple product between a Fourier transform of the object distribution and a CTF, which is a Fourier transform of the PSF. Thus, either function expresses a system performance, if the system shows a linear response against the object distribution.

For ADF-STEM in which we can assume the incoherent imaging, the image can be described as [12,14]

$$I(x,y,z) = o_{STEM}(x,y,z) \otimes \left|h^{obj}(x,y,z)\right|^2 = o_{STEM}(\mathbf{r}) \otimes PSF(\mathbf{r}), \quad (1)$$

where o_{STEM} is the cross section of an incoherent signal (object function), such as electron intensity scattered to the ADF-detector, $h^{obj}(x,y,z)$ describes a wave field formed by the objective lens and $\otimes$ expresses the three-dimensional (3D) convolution operation. In this case, the PSF of the system is the probe intensity, namely $\left|h^{obj}(x,y,z)\right|^2$.

SCEM imaging is described as [12,14,20]

$$I(x,y,z) = \left|o(x,y,z) \otimes h^{obj}(-x,-y,-z)h^{col}(x,y,z)\right|^2 = \left|o(\mathbf{r}) \otimes PSF(\mathbf{r})\right|^2, \quad (2)$$

where $o(\mathbf{r})$ is the object function, $h^{obj}(x,y,z)$ and $h^{col}(x,y,z)$are the PSFs of the objective and collector lenses, respectively. Thus, the PSF of the whole system is $h^{obj}(-x,-y,-z)h^{col}(x,y,z)$. As discussed below, for an aberration-free symmetric SCEM, $h^{obj}(-x,-y,-z) = h^{obj}(x,y,-z) = h^{col}(x,y,z)^*$and the PSF becomes identical to that of ADF-STEM. However, we have to note that the object function is different between ADF-STEM and SCEM. The object function of HAADF-STEM is a HAADF absorption potential in the absorption model [18], whereas for the object function of SCEM, a transmission function derived within the phase object approximation is often used [12,14,15,21]. The phase object has the form of $t(\mathbf{r}) = \exp(i\sigma V(\mathbf{r}))$, where $V(\mathrm{r})$ is the crystal potential and $\sigma$is the interaction constant. For a single-layer or a single atom, a phase-grating works well as the transmission function and can predict an intensity distribution [12,14]. However, its value is unity in the area of zero potential, namely in vacuum, and the convolution between the phase grating and PSF depends on the volume of integration [12].

In optics, this unphysical situation is avoided by defining the object function as a sum of the unscattered and scattered components as $o(\mathbf{r}) = \delta(z) + s(\mathbf{r})$ [20], where $\delta(z)$ is the Dirac delta function. The delta function gives the unscattered wave at the observation plane when it is convoluted with a 3D-PSF and$s(\mathbf{r})$represents the scattering object, which is assumed to be weaker than the unscattered wave. In the case of phase object $s(\mathbf{r}) = t(\mathbf{r}) - 1 = \exp(i\sigma V(\mathbf{r})) - 1$, which becomes zero in vacuum. Using the scattering power $s(\mathrm{r})$ for an object function, as in optics, we can avoid the unphysical dependence on the integration volume.

Then, the BF-SCEM intensity may be given using $s(\mathbf{r})$ as the object function:

$$I(x,y,z) = \left|(\delta(z) + s(\mathbf{r})) \otimes PSF(\mathbf{r})\right|^2 = \left|1 + s(\mathbf{r}) \otimes PSF(\mathbf{r})\right|^2 \approx 1 + 2\mathrm{Re}[s(\mathbf{r}) \otimes PSF(\mathbf{r})].$$

Therefore, the ADF-STEM and BF-SCEM intensities are both linear in the PSF, and thus the information transfer becomes identical between them as pointed out by several authors [12,14].

In the case of ADF-SCEM there is no unscattered wave at the observation plane, and thus the observed amplitude is simply given by a convolution between the scattering object and the PSF:

$$I(x,y,z) = \left|s(\mathbf{r}) \otimes PSF(\mathbf{r})\right|^2$$

The mathematical justification for this assumption is given below (Eq. (10)). Note that the intensity is not linear in PSF.

4. Shapes of PSF and CTF

A PSF of a single lens can be expressed as a stack of two-dimensional PSFs evaluated at each defocus z:

$$h(x,y,z) = \int A(\mathbf{K}_\parallel)\exp\{-i\chi(K_\parallel,z)\}\exp(i\mathbf{K}_\parallel\mathbf{R})d\mathbf{K}_\parallel \tag{3}$$

Here $\mathbf{K}_\parallel$ is a 2D reciprocal space vector, $\mathbf{R} = (x,y)$ is a 2D real-space vector and χ is the lens aberration function. When all aberrations are ignored as in the case of ideal (aberration free) lens, it can be written as

$$\chi(\mathbf{K}_\parallel,z) = \pi\lambda\left|\mathbf{K}_\parallel\right|^2 z$$

The corresponding CTF can be calculated numerically using Fourier transform. When all aberrations except defocusing are ignored a CTF for an individual lens becomes a section of the sphere (Ewald sphere) [20].

The PSF of SCEM is a product of the two PSFs for the objective and collector lenses:

$$PSF(x,y,z) = h^{obj}(-x,-y,-z)h^{col}(x,y,z) \tag{4}$$

Then, the CTF of SCEM is calculated by convoluting the CTFs for the objective and collector lenses:

$$CTF(\xi,\eta,\zeta) = H^{obj}(-\xi,-\eta,-\zeta) \otimes H^{col}(\xi,\eta,\zeta) \tag{5}$$

Then, the SCEM CTF is calculated by convoluting the two opposite spherical sections of the objective and collector lenses as illustrated in Fig. 2(a) for BF-SCEM case.

Fig. 3 shows the PSF and CTF of a rotationally symmetric aberration-free BF-SCEM calculated for the convergence and collection semiangles of 30 mrad. The FWHM of the PSF is 0.045 nm in the x–y plane, and 4.9 nm in the z direction. These values roughly correspond to the ranges of CTF of $4\alpha/\lambda$ for x–y and α^2/λ for the z direction [11,14,20] as shown in Fig. 2(b).

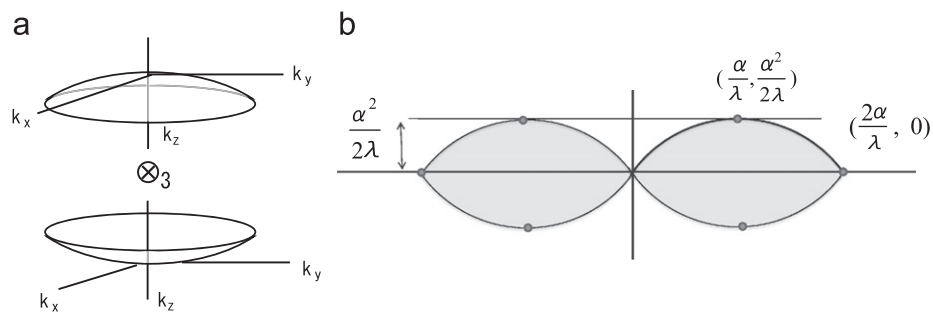

Fig. 2. (a) Schematics of the convolution of the CTFs for the objective and collector lenses that results in (a) BF-SCEM CTF. (b) The x–z section of BF-SCEM CTF. In the shaded area the CTF has non-zero value.

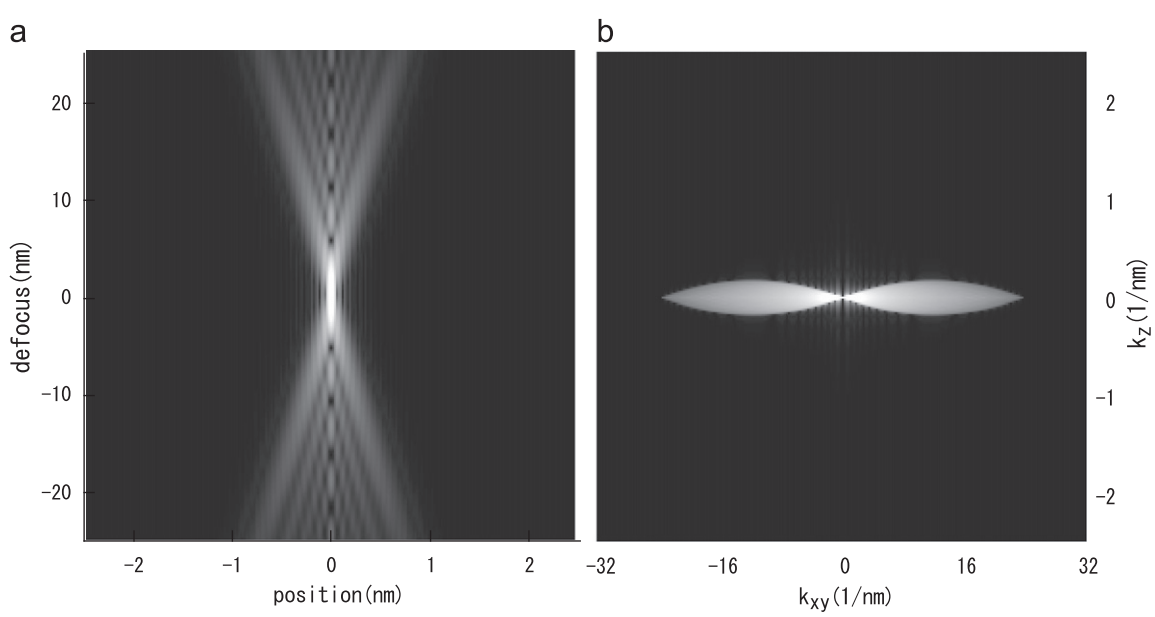

Fig. 3. (a) The x–z section of point-spread-function and (b) the k_x–k_z section of contrast transfer function of BF-SCEM calculated for 30 mrad convergence for both objective and collector apertures.

Here, the PSF shows an hourglass shape, or a head-to-head double cone, while the CTF resembles narrowed eyes' shape with so-called missing-cones near the origin [12,20]. A finite object perpendicular to the optical axis contributes to the BF-SCEM intensity for a wide defocus range, and thus yields an elongated image. This elongation effect of BF-SCEM has been explained by the missing cone of the CTF [10]. However, we note that contrary to SCOM the cone angle of BF-SCEM is almost 90°, and that the terminology of missing cones may be confusing. On the other hand, we could explain the elongation effect of BF-SCEM from simple geometrical considerations [13]. Below we will analyze the elongation of the BF-SCEM imaging in terms of the PSF.

The PSF and CTF of ADF-SCEM for a point detector can be calculated in the same way using different apertures for the objective and collector lenses. In this case the CTFs to be convoluted become a section and annular zone of Ewald spheres, respectively, defined by the objective and collector apertures, as shown in Fig. 4(a), where all aberrations except defocusing are ignored. Fig. 5 shows a PSF and CFT of aberration-free ADF-SCEM calculated for the convergence semiangle of 30 mrad and the collection semiangles between 30 mrad and 40 mrad. An overall feature of the PSF of ADF-SCEM is also characterized by a similar hourglass observed for the BF-SCEM. On the other hand, the CTF of ADF-SCEM shows distinctively different shapes from that of BF-SCEM [12,20]. The FWHM of the PSF is 0.035 nm in the x–y plane and 5.5 nm in the z direction. These values roughly correspond to the ranges of CTF of $2(\beta_{out}+\alpha)/\lambda$ for x–y and $\beta_{out}^2/2\lambda$ for the z direction as shown in Fig. 4(b), where $\alpha=\beta_{in}$. The limit of CTF in the x–y plane extends a little bit more due to the larger outer (40 mrad) collection semiangle, which results in the smaller FWHM of PSF in the x–y plane. On the other hand, the FWHM in the z direction becomes slightly worse since the range of the CTF along the z direction is narrower than that of BF-SCEM. It may be noted that the CTF has a missing-region close to the origin as in the case of BF-SCEM, although ADF-SCEM does not show an elongation effect as observed in BF-SCEM [13,16,17]. Thus, it is clear that a simple explanation of the elongation effect in BF-SCEM using only the shape of the CTF shape, namely a missing-cone is insufficient.

When all aberrations except defocusing are ignored, $h(x,y,-z)=h(x,y,z)^*$. Thus, the PSF of each rotationally symmetric lens has Hermitian symmetry, $h(-x,-y,-z)=h(x,y,-z)=h(x,y,z)^*$, and the value of BF-SCEM PSF becomes

$$PSF_{BF}(x,y,z)=h_{BF}^{obj}(-x,-y,-z)h_{BF}^{col}(x,y,z)=h_{BF}^{obj}(x,y,z)^*h_{BF}^{col}(x,y,z)=\left|h_{BF}^{obj}(x,y,z)\right|^2 \tag{6}$$

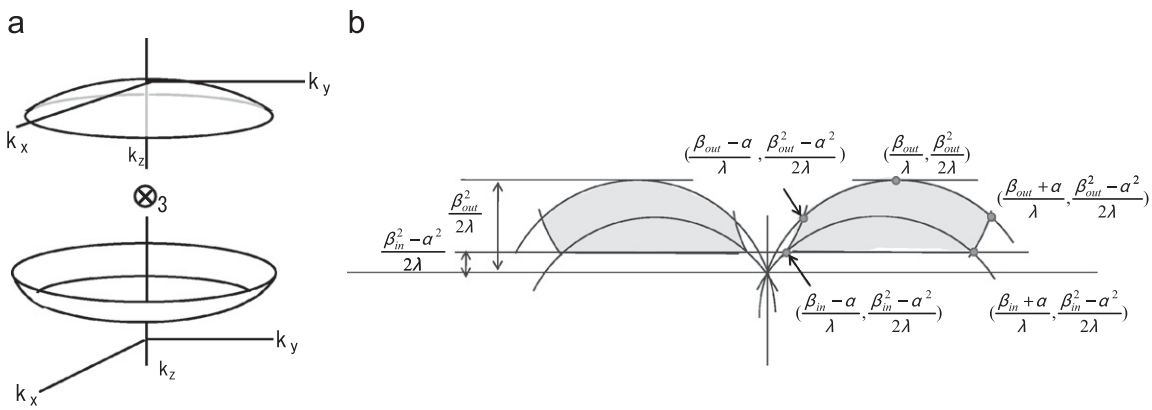

Fig. 4. (a) Schematics of the convolution of two CTFs of the objective and collector lenses that corresponds to ADF-SCEM CTF. (b) The x–z section of ADF-SCEM CTF. The shaded region is where the CTF has a non-zero value.

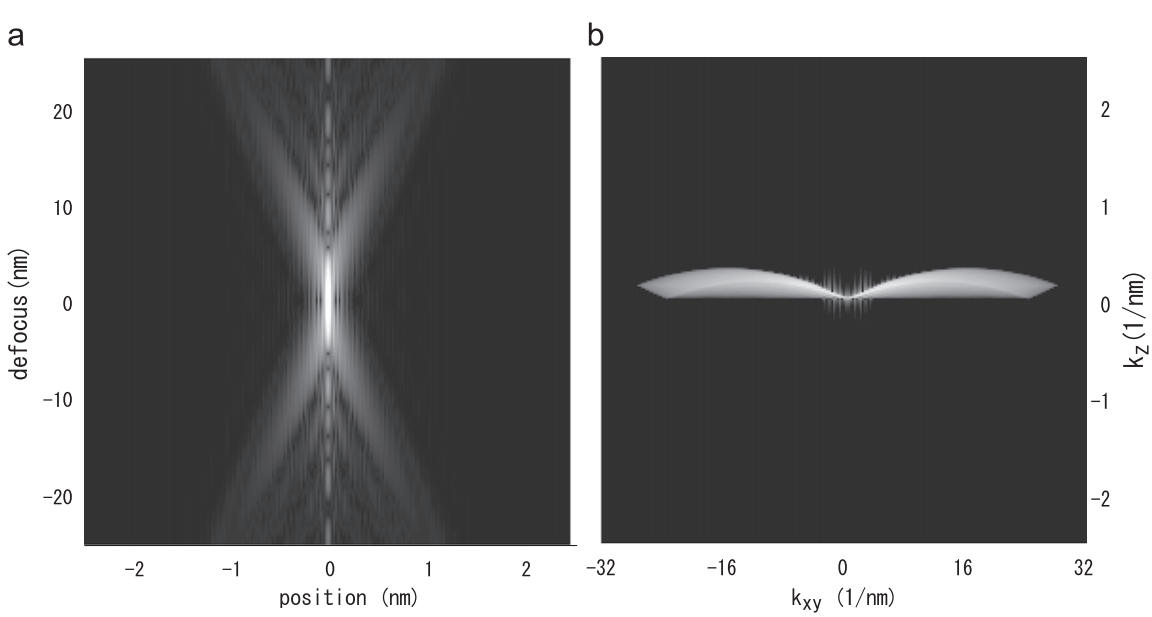

Fig. 5. (a) The x–z section of the PSF and (b) the k_x–k_z section of the CTF of ADF-SCEM. The objective aperture is 30 mrad and the collector aperture is 30–40 mrad.

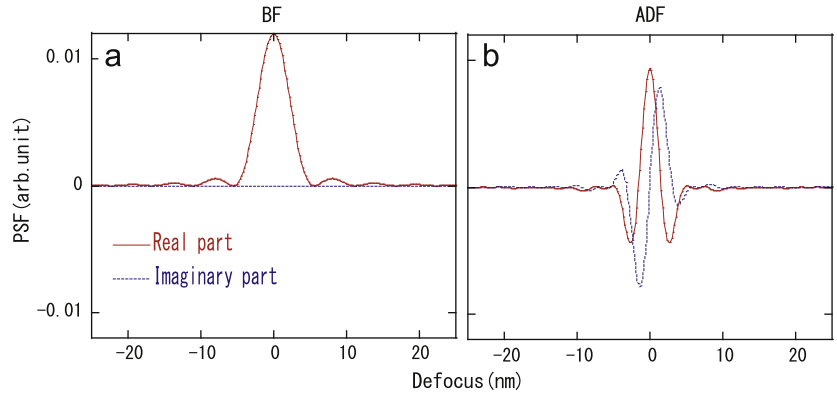

Fig. 6. The profiles of (a) BF –SCEM PSF and (b) ADF-SCEM PSF. The former is real while the latter has an imaginary part, which is asymmetric about $z=0$.

This function is real and positive, and its distribution is symmetric to reflection over the mid plane ($z=0$):

$$h_{BF}(x,y,z)=h_{BF}(x,y,-z)$$

It may be noted that the integral of the BF-SCEM PSF perpendicular to the optic axis (over the x–y plane) is unity for any defocus:

$$\int PSF_{BF}(x,y;z)dxdy=\int |h_{BF}^{obj}(x,y;z)|^2dxdy=\frac{1}{A}\int |H_{BF}^{obj}(\xi,\eta;z)|^2d\xi d\eta=1, \tag{7}$$

since $|H(\xi,\eta,z)|=1$.

On the other hand, in the case of ADF-SCEM even when all aberrations except defocusing are ignored, PSF is still complex:

$$PSF_{ADF}(x,y,z)=h_{ADF}^{obj}(-x,-y,-z)h_{ADF}^{col}(x,y,z)=h_{ADF}^{obj}(x,y,z)^*h_{ADF}^{col}(x,y,z), \tag{8}$$

and its distribution becomes a complex-conjugate after reflection over the plane $z=0$:

$$h_{ADF}(x,y,z)=h_{ADF}(x,y,-z)^* \tag{9}$$

Especially for the case with no overlap between objective and annular apertures, the integral of the ADF-SCEM PSF perpendicular to the optic axis is always zero:

$$\int PSF_{ADF}(x,y;z)dxdy=\int h_{ADF}^{obj}(x,y;z)^*h_{ADF}^{col}(x,y;z)dxdy$$
$$=\int H_{ADF}^{obj}(-\xi,-\eta;z)^*H_{ADF}^{col}(\xi,\eta;z)d\xi d\eta=0, \tag{10}$$

Here, we have used the property of Fourier transform that an integral of the product of two functions in one space is equal to an integral of the product of two functions in other space.

Although the PSF shows the similar shape of an hourglass both for BF and ADF PSF, their profiles are quite different when the real and imaginary parts of the PSFs are plotted in the z direction as shown in Fig. 6. Note that the imaginary part of the ADF-SCEM PSF is antisymmetric along the z-direction. In the following section, we use the PSF profiles to explain some features of BF- and ADF-SCEM images.

5. Imaging properties of BF-SCEM derived from PSF

Consider the intensity of BF-SCEM signal when a thin finite object is gradually shifted along the z-axis of the probe. For the case where defocus value is large so that the probe is much larger than the size of atoms, the atomic structure of the object can be neglected and the object can be treated as a homogeneous medium. For such case, the thin object larger than the section of the PSF produces a constant signal from Eq. 7. When object

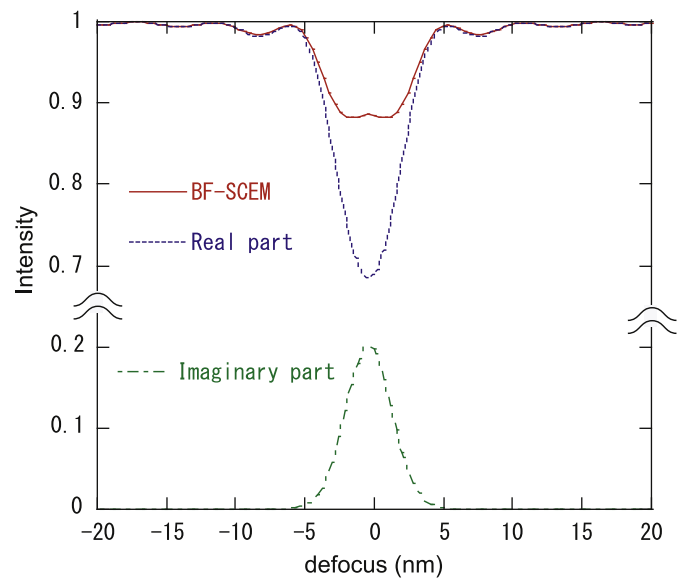

Fig. 7. BF-SCEM intensity profile of single atom calculated using the CTF, plotted together with the real and imaginary part contributions.

moves further from the confocal plane, the finite size of the object becomes smaller than the section of the PSF, and thus the signal starts to decrease from the constant value because the electron that passes through the sample reduces. This qualitatively describes the elongation effect in BF-SCEM image [13].

The fact that the BF-SCEM PSF is a real-valued function (Eq. 6) explains why a contrast of BF-SCEM for a phase object will be low. The first-order term of a phase grating expansion is imaginary, and thus its convolution with the real-valued PSF is also imaginary as discussed by Cosgriff et al. [21]. Thus, the lowest order in the BF image intensity of a phase object becomes a second order, and the contrast becomes low. This is contrary to the BF HRTEM image, where the first-order term of a phase grating expansion contributes to the image intensity at a Scherzer focus. At and near the confocal position, the probe is well focused to the atomic level. Then the atomic nature of the sample appears. Cosgriff et al.[21] showed that the contrast of a single atom as a function of z has a small rise at the position as shown in Fig. 7, and they explained this by atomic focusing.

This rise can be straightforwardly explained by a balance between contributions from the real and imaginary parts of the phase grating. Even if we include the higher-order terms in the exponential expansion of the phase object, the weak scattering approximation will hold provided all the terms included are small compared with the unscattered wave. When we include terms up

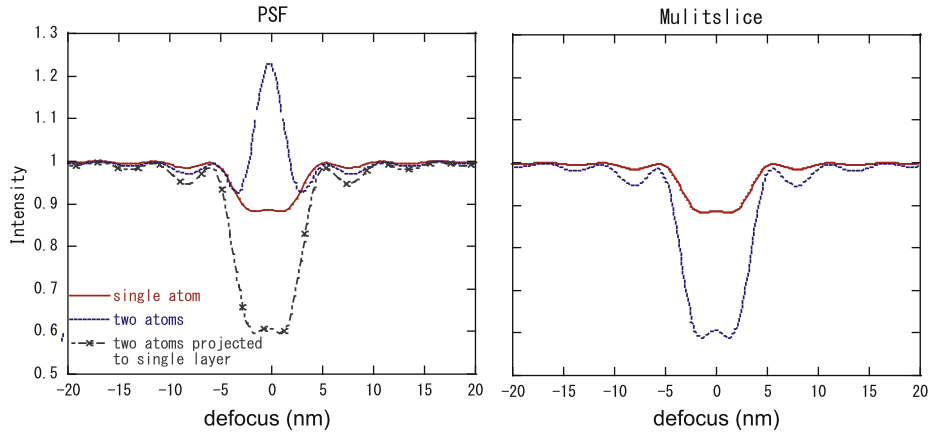

Fig. 8. BF-SCEM intensity profiles of one gold atom and two atoms of gold (separated by 0.4 nm along the beam direction) calculated using the PSF (a) and multislice method (b).

to the second order, the image intensity can be given by

$$I(\mathbf{r}) = \left|\exp\{i\sigma V(\mathbf{r})\} \otimes PSF(\mathbf{r})\right|^2$$
$$\approx \left|\left(1 + i\sigma V(\mathbf{r}) - \frac{1}{2}(\sigma V(\mathbf{r}))^2\right) \otimes PSF(\mathbf{r})\right|^2$$
$$\approx 1 - (\sigma V(\mathbf{r}))^2 PSF(\mathbf{r}) + (\sigma V(\mathbf{r}) \otimes PSF(\mathbf{r}))^2 \tag{11}$$

Note that the first-order term becomes imaginary after the convolution with the real-valued PSF. Thus, the lowest orders in the BF-SCEM image intensity from both the real and imaginary parts of the phase object are of the second order, within the weak scattering approximation. In Fig. 7 the image intensity of a single Au atom located at $z=0$ is plotted together with the real and imaginary contributions. The contrast from the real part is negative around the atom position, whereas it is positive for the imaginary part. Thus, the resultant intensity profile shows a small rise at the focus position. When the resolution increases, both contributions become sharper and thus the width between two minima decreases as found by Cosgriff et al. [21]. However, the atomic focusing model may not be able to explain quantitatively the change of shape as a function of resolution.

Next, we consider a two-atom case of aberration-free symmetric BF-SCEM imaging. In Fig. 8, we show the BF-SCEM intensity profiles of one gold atom and two atoms of gold (separated by 0.4 nm along the beam direction) calculated by the multislice method and by the PSF (the convolution is actually calculated using the CTF in reciprocal space). The PSF intensity profile of two atoms is calculated by two different projected potentials; one is projecting two atoms into a single layer, and the other is projecting two atoms into two different layers. Here the PSF result for projecting two atoms into a single layer is close to the one obtained by the multislice method. On the contrary, placing two atoms in two different layers gives an unphysical intensity. This discrepancy is because multiple scattering contributions between layers are neglected in the PSF treatment.

The unphysical intensity distribution can be understood by considering the object function consisting of two layers characterized by the same potential V. The image intensity can be expressed for the real-valued PSF as

$$I(\mathbf{r}) = \left|\left[\delta(\mathbf{r}) + s(\mathbf{r})\right] \otimes PSF(\mathbf{r})\right|^2$$
$$= \left|[1 + (\exp(i\sigma V(\mathbf{r})) - 1) + (\exp(i\sigma V(\mathbf{r})) - 1)] \otimes PSF(\mathbf{r})\right|^2$$
$$\approx \left|\left[1 + \left(i\sigma V(\mathbf{r}) - \frac{1}{2}(\sigma V(\mathbf{r}))^2\right) + \left(i\sigma V(\mathbf{r}) - \frac{1}{2}(\sigma V(\mathbf{r}))^2\right)\right] \otimes PSF(\mathbf{r})\right|^2$$
$$\approx 1 - 2\sigma^2[V(\mathbf{r})^2 \otimes PSF(\mathbf{r})] + (2\sigma)^2[V(\mathbf{r}) \otimes PSF(\mathbf{r})]^2 \tag{12}$$

where we assume that those two layers are close with each other so that the difference in PSF can be ignored. The lowest terms are of second order by potentials, as in the case of a single atom.

The second term increases linearly with number of layers while the third term quadratically. Therefore, the total intensity will exceed 1 regardless of how weak is the scattering. This unphysical intensity distribution occurs because the contribution from double scattering by the second layers is ignored in the image calculated using PSF. Thus, it is evident that at least double scattering should be taken into account in the case of phase object imaging for aberration-corrected symmetrical BF-SCEM. This will not happen if two layers can be projected into one as shown above. Nevertheless, a total (3D) sample may not be projected to a single layer, and the depth sectioning cannot be argued by the projected layers.

In the case where the system's aberration is not negligible, the PSF becomes complex. Then, it can be shown that the BF-SCEM image intensity is of the first order in terms of the potential as in the case of BF-HRTEM by explicitly writing the real and imaginary parts of the PSF as

$$I(\mathbf{r}) = \left|[1 + (\exp(i\sigma V_1(\mathbf{r})) - 1) + (\exp(i\sigma V_2(\mathbf{r})) - 1)]\right.$$
$$\left.\otimes (PSF_r(\mathbf{r}) + PSF_i(\mathbf{r}))\right|^2$$
$$\approx 1 - 2\sigma(V_1(\mathbf{r}) + V_2(\mathbf{r})) \otimes PSF_i(\mathbf{r}) - \sigma^2(V_1(\mathbf{r})^2 + V_2(\mathbf{r})^2) \otimes PSF_r(\mathbf{r})$$
$$+ \sigma^2[(V_1(\mathbf{r}) + V_2(\mathbf{r})) \otimes PSF_r(\mathbf{r})]^2 + \sigma^2[(V_1(\mathbf{r}) + V_2(\mathbf{r})) \otimes PSF_i(\mathbf{r})]^2 \tag{13}$$

Here, the first order term contributes mainly to the image intensity, and thus the PSF can be used to estimate the image intensity. This operation condition may be preferable in practice because the first-order term contributes to the image with a strong contrast. As we have seen in Eq. (8) the PSF of ADF-SCEM is complex so that the image can always be safely approximated by the square of a convolution of the PSF and the object function.

6. Imaging properties of ADF-SCEM derived from PSF

In contrast to the BF-SCEM case, when a thin object is larger than the section of the ADF-SCEM PSF, the signal becomes zero (Eq. 10) at any defocus value. As a consequence, ADF SCEM signal does not appear from a large object at any defocused position, when the object is wider than the PSF. This quantitatively explains why ADF SCEM does not show the elongation effect. When the object covers only a portion of PSF by moving further from the confocal plane, or when the object moves from the optic axis, this cancellation over the integration becomes partial, and may result in some intensity. Nevertheless, the convolution

integral of ADF SCEM may be destructive so that the resultant intensity may not be significant.

At and near the confocal position, the probe is well focused to the atomic level and again the atomic structure of the sample appears. In contrast to BF-SCEM, however, the PSF of ADF-SCEM is complex so that the potential of the first order dominates the image contrast so that the effect of double diffraction is unimportant. This can be seen in Fig. 9 where the image intensity profiles of one and two Au atoms are calculated with the PSF and multislice. Here, the two profiles are almost identical for both single and two atoms between PSF and multislice.

It may be noted that the integral of ADF-SCEM PSF over the x–y plane is zero even on the confocal plane. It means that when the object function does not change much for the range of the probe size, the ADF-SCEM signal will be small. Therefore, an ADF-SCEM signal is only generated by sharp features of the sample, but not generated by broad sample features. This result was also explained by a simple geometrical consideration that a sharp feature scatters electrons into the collector aperture [13]. It is therefore evident that the shape of the PSF does not explain the elongation effect. In the same way, the shape of the CTF, namely the missing-cone, does not simply explain the elongation effect. We need to evaluate the value of PSF or CTF.

As we noted in Section 4, the imaginary part of ADF-SCEM PSF is antisymmetric in the z direction, and the positive and negative parts of PSF will cancel out, when the probe is focused within the object. On the contrary, when the probe is located at an interface or surfaces this cancellation becomes imperfect. Therefore, the ADF-SCEM intensity should be sensitive for detecting interfaces as demonstrated in the following simulations.

Here, we calculated the same 30 nm thick ⟨110⟩ GaAs sample as used in Ref. [21]. The images in Fig. 10(a) and (b) are simulated

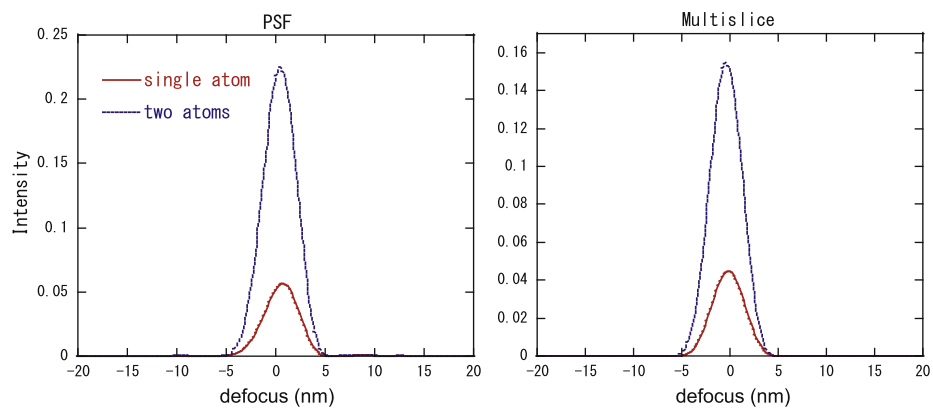

Fig. 9. The ADF-SCEM image intensity profiles of one and two Au atoms calculated with the PSF and multislice method.

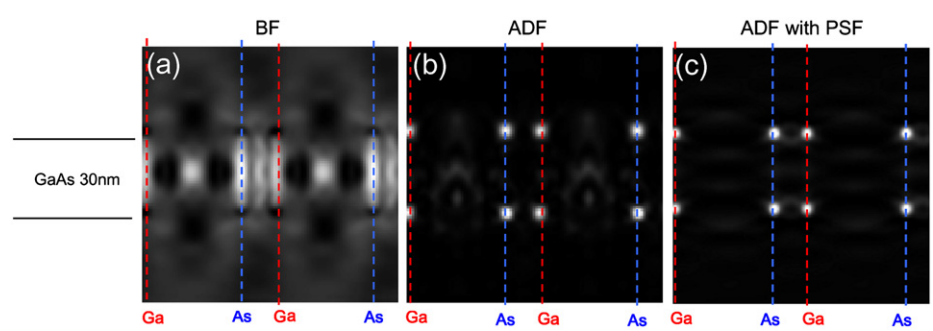

Fig. 10. Simulated x–z images of 30 nm thick ⟨110⟩ GaAs located at the center of the image calculated for 1.13 nm in the x direction and 90 nm in the z direction for (a) BF, (b) ADF and (c) ADF with the PSF. In ADF-SCEM, the atoms within the slab show almost no intensity, and strong peak observed only at the surfaces.

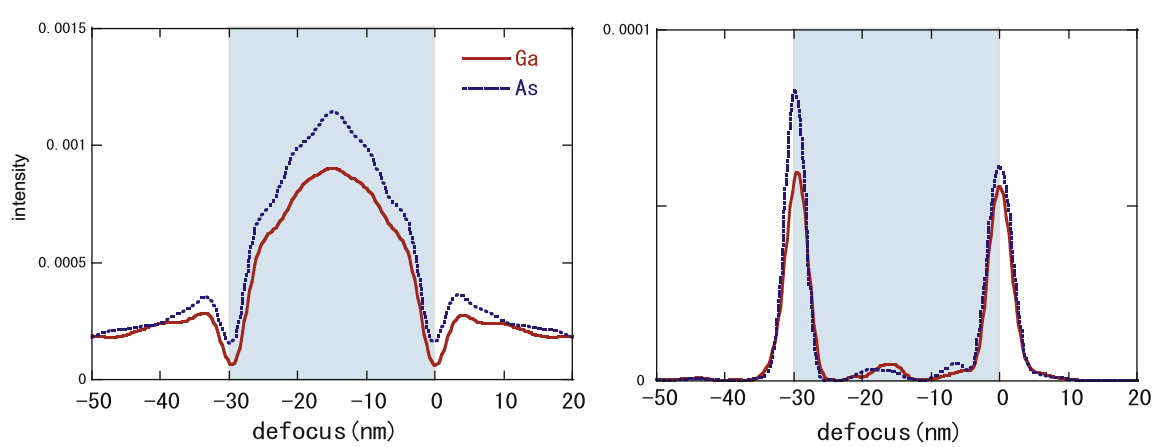

Fig. 11. The simulated (a) BF- and (b) ADF-SCEM intensity profiles of a 30 nm thick ⟨110⟩ GaAs sample for Ga and As columns together with two inter-atomic sites.

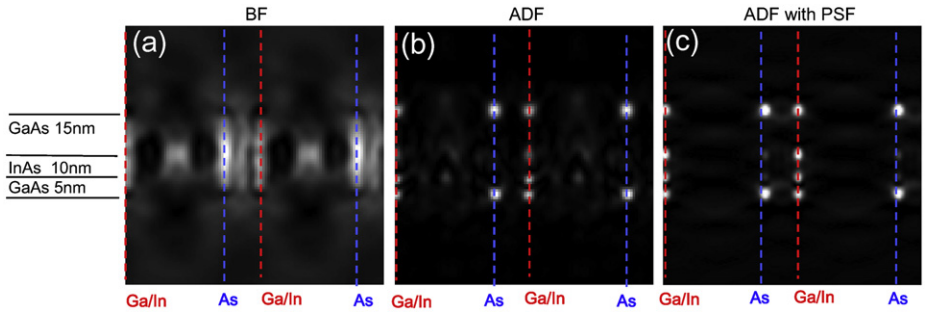

Fig. 12. The simulated *x*–*z* SCEM images of an InAs layer embedded in the 30 nm GaAs sample of Fig. 10 and located at 5 nm from the sample bottom, for (a) BF, (b) ADF and (c) ADF calculated with the PSF. The lattice constants are assumed to be the same for InAs and GaAs.

using the multislice method while the image in Fig. 10(c) is done by the PSF. The BF-SCEM image (Fig. 10a) is similar to the one given in Fig. 9 of Ref. [21], although the *z*-spread of the probe is three times larger here. It is striking that the atoms within the slab show almost no intensity in ADF-SCEM, while strong peaks were observed only at the surfaces (Fig. 10b). It may be noted that the PSF gives the ADF-SCEM image (Fig. 10c) similar to the one calculated with the multislice method.

Fig. 11 shows intensity profiles of (a) BF- and (b) ADF-SCEM images along the *z*-direction at the Ga and As columns. As already pointed by Cosgriff et al., BF-SCEM intensity at the atomic column drops at the top and bottom surfaces of the sample. On the contrary ADF-SCEM intensities have their peaks at the top and bottom surfaces for atomic column site.

Fig. 12 shows simulated images for a buried interface, where 10 nm of GaAs is replaced by InAs at 5 nm from the sample bottom as shown in the figure. Thus, the Ga/In columns have discontinuity, while the As atom columns are continuous. In the BF-SCEM image (Fig. 12a), the change from GaAs to InAs is faint, and it is difficult to identify the depth of the impurity layer as pointed by Cosgriff et al. [21]. On the other hand, a clear peak appears at the Ga/In interface in the ADF-SCEM image while the As column intensity does not show any contrast between the top and bottom interfaces (Fig. 12b). This unique edge enhancement effect of ADF-SCEM should be useful for depth sectioning. It may be noted again that the PSF gives the ADF-SCEM image (Fig. 12c) similar to the one calculated with the multislice method.

7. Conclusions

We have discussed that the imaging properties of BF- and ADF-SCEM are discussed based on their PSFs. The PSFs of both BF-SCEM and ADF-SCEM show the similar hourglass shapes, and the corresponding CTFs have comparable missing cones. Therefore, the difference in the imaging properties of BF and ADF-SCEM cannot be explained by the shape of the PSF or CTF. It is shown that the ADF-SCEM PSF is complex and has a Hermitian symmetry, while the symmetric BF-SCEM PSF is always positive and possesses a center of symmetry. The positive valued PSF explains the large elongation effect of BF-SCEM for a laterally extended object, and the complex-valued PSF accounts for the absence of the elongation effect in ADF-SCEM. This means that it is essential to consider the numerical distributions of PSF as well as its overall shape to understand the imaging characteristics.

The Hermitian symmetry of the ADF-SCEM PSF results in the interesting "edge enhancement effect" at the interface. Simulation using the PSF and multislice method verified this effect at the surfaces of a GaAs and at the InAs impurity interfaces embedded in GaAs. This unique feature of ADF-SCEM can potentially be useful for depth sectioning. It is also pointed out that the approach of PSF is not applicable for BF-SCEM of a phase object, if the lens system is symmetric and aberration free.

Acknowledgment

This research was partially supported by a Grant-in-Aid for Scientific Research (C) (21560036) and a Grant-in-Aid for Young Scientists (B) (20760027) from the Japan Society for the Promotion of Science, Japan.

References

[1] N.J. Zaluzec, Microscopy Microanalysis 13 (2007) 1560.
[2] S.P. Frigo, Z.H. Levine, N.J. Zaluzec, Applied Physics Letters 81 (2002) 2112.
[3] M. Minsky, Scanning 10 (1988) 128.
[4] M. Laurent, G. Johannin, H. Le Guyader, A. Fleury, Biology of the Cell 76 (1996) 113.
[5] M. Takeguchi, A. Hashimoto, M. Shimojo, K. Mitsuishi, K. Furuya, Journal of Electron Microscopy 57 (2008) 123.
[6] A. Hashimoto, M. Takeguchi, M. Shimojo, K. Mitsuishi, M. Tanaka, K. Furuya, e-Journal of Surface Science and Nanotechnology 6 (2008) 111.
[7] J.L. Hutchinson, J.M. Titchmasrsh, D.J.H. Cockayne, R.C. Doole, C.J.D. Hetherington, A.I. Kirkland, H. Sawada, Ultramicroscopy 103 (2005) 7.
[8] P.D. Nellist, G. Behan, A.I. Kirkland, C.J.D. Hetherington, Applied Physics Letters 89 (2006) 124105.
[9] H. Sawada, et al., Journal of Electron Microscopy 58 (2009) 341.
[10] H.L. Xin, D.A. Muller, Journal of Electron Microscopy (2009) 1–9.
[11] V. Intaraprasonk, H.L. Xin, D.A. Muller, Ultramicroscopy 108 (2008) 1454.
[12] H.L. Xin, D.A. Muller, Microscopy Microanalysis 16 (2010) 445.
[13] K. Mitsuishi, A. Hashimoto, M. Takeguchi, M. Shimojo, K. Ishizuka, Ultramicroscopy 111 (2010) 20–26.
[14] P.D. Nellist, E.C. Cosgriff, G. Behan, A.I. Kirkland, Microscopy Microanalysis 14 (2008) 82.
[15] A.J. D'Alfonso, E.C. Cosgriff, S.D. Findlay, G. Behan, A.I. Kirkland, P.D. Nellist, L.J. Allen, Ultramicroscopy 108 (2008) 1567.
[16] A. Hashimoto, M. Shimojo, K. Mitsuishi, M. Takeguchi, Journal of Applied Physics 106 (2009) 086101.
[17] A. Hashimoto, M. Shimojo, K. Mitsuishi, M. Takeguchi, Microscopy Microanalysis 16 (2010) 233.
[18] K. Ishizuka, N. Uyeda, Acta Crystallographica A 33 (1977) 740.
[19] P.A. Stadelmann, Ultramicroscopy 21 (1987) 131.
[20] M. Gu, Principles of Three-Dimensional Imaging in Confocal Microscopes, World Scientific, Singapore, 1996.
[21] E.C. Cosgriff, A.J. D'Alfonso, L.J. Allen, S.D. Findlay, A.I. Kirkland, P.D. Nellist, Ultramicroscopy 108 (2008) 1558.

nature COMMUNICATIONS

OPEN

ARTICLE

Received 19 Jan 2011 | Accepted 8 Jun 2011 | Published 5 Jul 2011

DOI: 10.1038/ncomms1378

Optical switching of nuclear spin–spin couplings in semiconductors

Atsushi Goto[1,2], Shinobu Ohki[1], Kenjiro Hashi[1] & Tadashi Shimizu[1]

Two-qubit operation is an essential part of quantum computation. However, solid-state nuclear magnetic resonance quantum computing has not been able to fully implement this functionality, because it requires a switchable inter-qubit coupling that controls the time evolutions of entanglements. Nuclear dipolar coupling is beneficial in that it is present whenever nuclear–spin qubits are close to each other, while it complicates two-qubit operation because the qubits must remain decoupled to prevent unwanted couplings. Here we introduce optically controllable internuclear coupling in semiconductors. The coupling strength can be adjusted externally through light power and even allows on/off switching. This feature provides a simple way of switching inter-qubit couplings in semiconductor-based quantum computers. In addition, its long reach compared with nuclear dipolar couplings allows a variety of options for arranging qubits, as they need not be next to each other to secure couplings.

[1] National Institute for Materials Science, 3-13 Sakura, Tsukuba, Ibaraki 305-0003, Japan. [2] PRESTO, Japan Science and Technology Agency, 4-1-8 Honcho, Kawaguchi, Saitama 332-0012, Japan. Correspondence and requests for materials should be addressed to A.G. (email: goto.atsushi@nims.go.jp).

Nuclear magnetic resonance (NMR) quantum computing has attracted broad interest because it is one of the most advanced testbeds for quantum computation. Although the interest began with solution NMR[1–3], it is now believed that scalable NMR quantum computers in the future will be built on semiconductors based on highly developed semiconductor technology[4–6]. The main challenges include the initialization and the creation of spin entanglement, which are essential features of quantum computation[7]. Semiconductor-based NMR quantum computers are advantageous as they can be achieved optically; that is, the initialization (nuclear–spin polarization) is provided by optical pumping[8,9], and the entanglement is created via internuclear (nuclear spin–spin) couplings between polarized nuclei[10,11]. In optically pumped semiconductors, the latter manifests itself as dipolar order[12,13] and double-quantum coherence[14].

Switchability is another essential functionality required for internuclear couplings, which should be 'on' during operations and 'off' otherwise. In this respect, nuclear dipolar coupling (D-coupling, hereafter) is not the best choice for the above-mentioned reasons. In addition, the time required for operations increases rapidly with increasing qubit number because of decoupling operations[15]. Other possible candidates include indirect couplings mediated by donor electrons[4] and magnons[15]. Their implementations are fairly challenging, however, given the complicated switching mechanisms. By contrast, the scheme presented in this paper is rather simple; the coupling strength can be controlled externally through light power, and on/off switching can be easily implemented.

In this study, we have preformed cross-polarization (CP) experiments with GaAs under light illumination, and demonstrated that a nuclear spin–spin coupling grows in strength, and extends its reach to farther nuclei as light power is increased. These futures bring about a unique transition of the CP process from oscillatory behaviour in the 'dark' towards exponential relaxation with increasing light power. The experiments provide us with information on the essential features of the optically induced nuclear spin–spin couplings; in particular, we find that the coupling strength is roughly proportional to light power, which is essential for the switching of the couplings.

Results

CP process in GaAs in the dark. The present mechanism is manifested in a CP process from ^{75}As (I-spin) to ^{71}Ga (S-spin) in GaAs under infrared light irradiation. Before detailing this process, we first describe it in the dark (without light irradiation) as a reference. This is an ordinary CP process, for which we expect a contact time (τ_{cp}) dependence of S-magnetization (M_S^{eq}) of the form

$$M_S^{eq}(\tau_{cp}) = M_0^{eq}[1-\exp(-\tau_{cp}/T_{IS})], \quad (1)$$

where T_{IS} is the cross-relaxation time. A relaxation process in the rotation frame ($T_{1\rho}$) need not be considered here, as it is sufficiently long because of high crystal symmetry[16,17]. The reality, however, is more complicated than equation (1). Figure 1 shows $M_S^{eq}(\tau_{cp})$ obtained in the dark, which exhibits a clear transient oscillation.

Transient oscillations have been reported in some molecular crystals, and attributed to discrete S–I coupling spectra of isolated S–I pairs[18–20]. The magnetization is transferred back and forth inside the pair with a frequency corresponding to half the flip-flop term of the D-coupling. The present sample, however, is not a molecular crystal, so isolated pairs are expected to be rare. Here an essential factor is the existence of two Ga isotopes, that is, ^{69}Ga and ^{71}Ga with natural abundances of $^{69}N_A = 0.604$ and $^{71}N_A = 0.396$, respectively. A local ^{75}As -^{71}Ga pair appears when only one of the four nearest-neighbour sites of ^{75}As is occupied by ^{71}Ga and the others are occupied by ^{69}Ga. The probability of finding such pairs is ${}_4C_1 \cdot {}^{71}N_A \cdot ({}^{69}N_A)^3 = 0.35$; that is, about 35% of ^{75}As have a single ^{71}Ga in the vicinity and contribute to the oscillation. The pairs are coupled through indirect scalar coupling J_{IS}, where D-couplings are absent because the Ga sites are situated at magic angle positions in the (100) crystal orientation[16,17,21]. The process is described by a damping oscillation[18],

$$M_S^{eq}(\tau_{cp}) = M_0^{eq}\left[1-\frac{1}{2}\exp(-R\tau_{cp})-\frac{1}{2}\exp(-3R\tau_{cp}/2)\cos(2\pi\Omega\tau_{cp})\right], \quad (2)$$

where Ω is the oscillation frequency ($\Omega = J_{IS}/2$) and R is the damping factor. We fit the data using equation (2) with Ω and R as free parameters. The best result is obtained with $\Omega = 0.74$ kHz, which yields $J_{IS} = 2\Omega = 1.48$ kHz. This value is comparable with that in the InP case ($J_{IS} = 2.3$ kHz)[17]. The fitting curve is shown by a solid line in Figure 1. The fit is not very good at the beginning of the oscillation; this may be due to the presence of ^{75}As sites with more than one ^{71}Ga nucleus in the four nearest-neighbour sites.

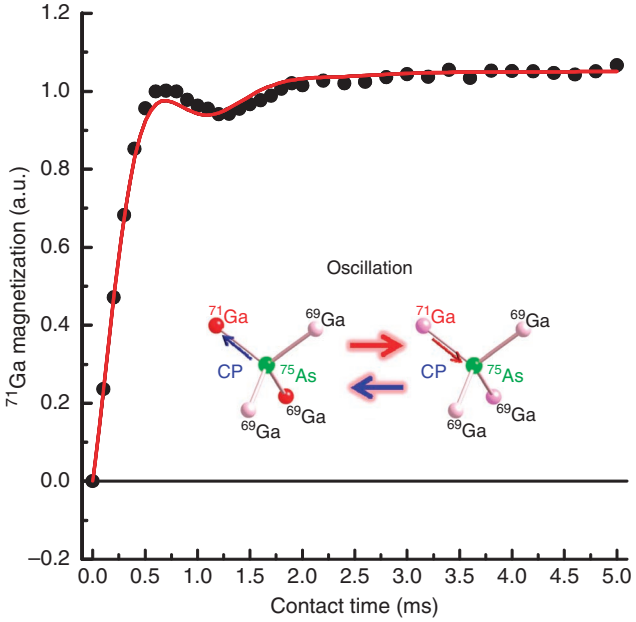

Figure 1 | CP experiment in GaAs in the dark. Contact time (τ_{cp}) dependence of ^{71}Ga magnetization (M_S^{eq}) in a cross polarization experiment in the dark at 10 K, normalized at $\tau_{cp} = 0.7$ ms. The pulse sequence is shown in Figure 5, where the light is turned off, that is, $P_{IR} = 0$ mW. The magnetization is transferred back and forth between ^{75}As and ^{71}Ga at a nearest neighbour site. This process gives rise to a transient oscillation. The solid red line represents the best-fit curve using equation (2).

CP process under light irradiation. Figure 2a shows the τ_{cp} dependence of S-polarization, $M_S(\tau_{cp})$ under various levels of light power, P_{IR}, which exhibits new local maxima (peaks) that are not observed in the dark. The maxima form a number of series (α, β, γ…), and the maximal position in each series shifts towards smaller values of τ_{cp} as the light power is increased. For example, the series 'β' shown by the red arrows starts with a broad maximum around $\tau_{cp} = 3.1$ ms at $P_{IR} = 100$ mW, which shifts towards smaller values of τ_{cp} as P_{IR} is increased and eventually merges into a peak at $\tau_{cp} = 0.8$ ms at 166 mW. These maxima represent new polarization transfer processes that appear under light irradiation. Figure 3 shows a three-dimensional representation of Figure 2a obtained by interpolating the data in between. The continuous shift of the maximum in each series can be readily confirmed.

This phenomenon can be explained by discrete increments in the number of S-nuclei (^{71}Ga) involved: in the dark ($P_{IR} = 0$ mW), the number of nuclei participating in the process is small and oscillatory behaviour is observed, as shown in Figure 1. Light illumina-

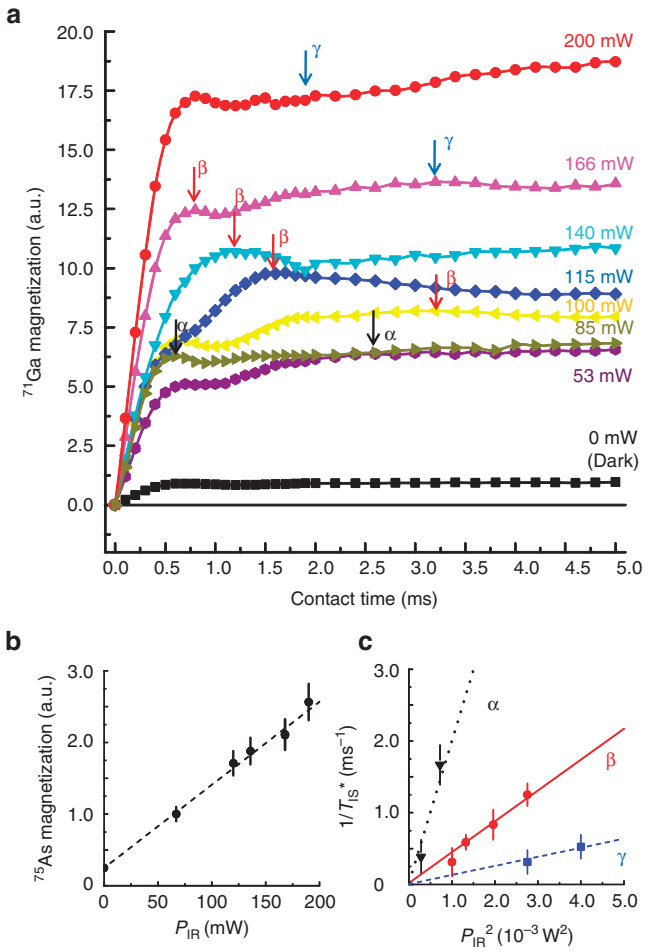

Figure 2 | CP experiments in GaAs under light irradiation. (**a**) Contact time (τ_{cp}) dependence of ^{71}Ga magnetization (M_s) in CP experiments at 10 K measured under light irradiation with power P_{IR} ranging from 0 to 200 mW. The pulse sequence is shown in Figure 5. The data at P_{IR} = 0 mW are the same as those in Figure 1. Black, red and blue arrows represent the three series of maxima. (**b**) The light power (P_{IR}) dependence of ^{75}As magnetization (M_I), which represents the enhancement of the nuclear spin polarization due to the optical pumping effect. The magnetization exhibits a linear dependence with P_{IR}. The error bars represent the data scatterings in a few experiments performed under the same conditions. (**c**) The values of $1/T_{IS}^*$ for the three series (α, β and γ) marked by the arrows in (**a**) plotted against P_{IR}^2. The error bars represent the breadth around each peak. The lines are visual guides.

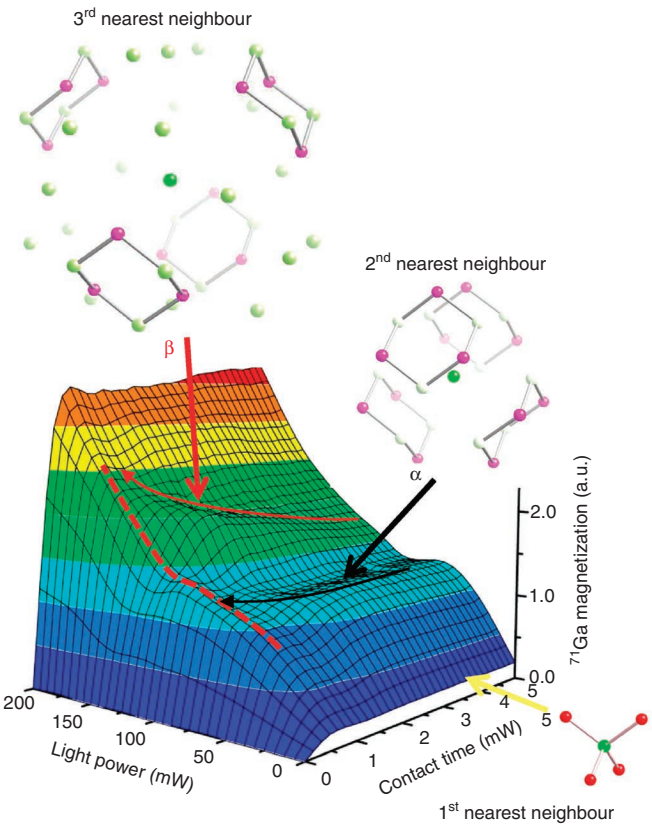

Figure 3 | Light power dependence of the CP process in GaAs. Three-dimensional representation of Figure 2a obtained by interpolating the data in between. The data shown by the yellow arrow represents those in the dark (P_{IR} = 0 mW), which corresponds to the polarization transfer to the nearest-neighbour ^{71}Ga through the conventional J_{IS}. The black (α) and red (β) arrows indicate the series of maxima corresponding, presumably, to the polarization transfers to the second and third nearest neighbour sites, respectively. The dotted red line represents the ^{71}Ga magnetization at τ_{cp} = 0.7 ms, which exhibits a plateau-like feature (that is, less steeper slope) around 80 mW.

tion causes a series of *S*-nuclei batches (α, β, γ…) to participate in sequence. Their contributions are successively added to the signal intensity one after another, whereas the speed of transfer from *I*- to *S*-nuclei in each series increases with the light power (that is, the maximal position shifts towards smaller values of τ_{cp}). As the number of nuclei involved is further increased, the cross relaxation is expected to approach the exponential relaxation behaviour given by equation (1)[20]. That is, we see here the transition from oscillatory behaviour in the 'dark' towards exponential relaxation with increasing light power. This is a unique case in that such a transition can hardly be observed in ordinary NMR measurements.

Another factor responsible for the phenomenon is the optical pumping effect[8,9]. It contributes to the *S*-magnetization (^{71}Ga) through the enhancement of the *I*-magnetization (^{75}As) caused by the polarization transfer from the optically oriented electrons for the duration of light irradiation τ_L = 60 s. Figure 2b shows the light-power dependence of the *I*-magnetization (^{75}As), which increases linearly with light power. This enhancement is partly responsible for the increase of the *S*-magnetization with increasing light power, as seen in Figures 2a and 3.

The τ_{cp} dependence of M_s is expressed as,

$$M_S(\tau_{cp}) = M_I^{dark}(\tau_L) m_{I\to S}^{eq}(\tau_{cp}) + M_I^{op}(P_{IR},\tau_L) \times \left[m_{I\to S}^{eq}(\tau_{cp}) + \sum_{i=\alpha} m_{I\to S}^{op,i}(P_{IR},\tau_{cp}) \right], \quad (3)$$

where $M_I^{dark}(\tau_L)$ in the first term on the right-hand side represents the *I*-magnetization in the dark portion of the sample recovered during τ_L = 60 s and $m_{I\to S}^{eq}$ represents the polarization transfer process to *S*-spins in the first nearest neighbour sites through J_{IS}. This process is essentially the same as that in Figure 1. On the other hand, $M_I^{op}(P_{IR},\tau_L)$ in the second term is the *I*-magnetization in the illuminated area generated by the optical pumping effect during τ_L = 60 s, whose P_{IR} dependence is shown in Figure 2b. This magnetization is transferred to *S*-spins through the two processes shown in the brackets: the same process as that in the dark, $m_{I\to S}^{eq}$, and additional ones induced by light irradiation, $\Sigma_i\, m_{I\to S}^{op,i}(P_{IR},\tau_{cp})$ (i = α, β, γ…). The latter are caused by the optically induced heteronuclear indirect coupling, J_{IS}^{opt}. We will discuss characteristics of this coupling in the next section.

NATURE COMMUNICATIONS | DOI: 10.1038/ncomms1378

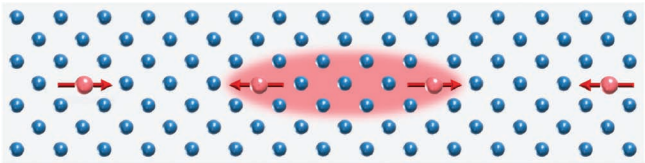

Figure 4 | Optical switching of a nuclear spin–spin coupling. A conceptual (ideal) model of optical switching of a nuclear spin–spin coupling between nuclear-spin qubits (red arrows) spaced a few lattice points apart from each other. Blue balls represent 'inert' (for example, spin-zero) nuclei. The nuclear dipolar couplings between the qubits are out of reach. Once the light is illuminated, a coupling emerges between the qubits. The strength of the coupling can be controlled externally through light power.

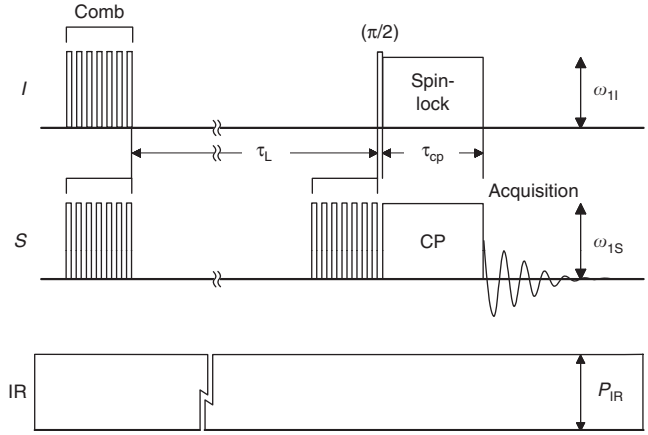

Figure 5 | Pulse sequence. Pulse sequence for optical pumping CP experiments. $I = {}^{75}$As, $S = {}^{71}$Ga and IR = infrared light (1.50 eV, σ^-). 'Comb': comb pulse consisting of a number of $\pi/2$ pulses. τ_L: duration of light irradiation (= 60 s). τ_{cp}: contact time for CP. $\omega_{1I}/2\pi$, $\omega_{1S}/2\pi$: rf-pulse strengths in terms of Rabi frequency (= 35 kHz). P_{IR}: infrared light power. The horizontal axis is not to scale.

Discussion

The new coupling J_{IS}^{opt} is presumably mediated by photo-excited electrons. It is known that electrons in metals can mediate indirect nuclear spin–spin couplings, a process referred to as the RKKY interaction[22]. In the present case, however, J_{IS}^{opt} is observed in semiconductors where no intrinsic Fermi surfaces exist. Moreover, the lifetimes and spin relaxation times of the photo-excited electrons usually fall in the range between pico- and nanoseconds, which is more than six orders of magnitude smaller than that of the CP process, that is, milliseconds. It is intriguing that two phenomena with such different time scales are coupled with each other.

The strength of J_{IS}^{opt} in each batch (α, β, γ…) can be evaluated by the cross-relaxation time T_{IS}^{opt} in $m_{I\to S}^{op,i}(P_{IR},\tau_{cp})$ (i = α, β, γ…). According to Demco *et al.*[17,20,23], the cross-relaxation time is expressed as

$$1/T_{IS}^{opt} \approx \frac{\sqrt{\pi}}{4} M_2^{IS} \tau_c, \tag{4}$$

where τ_c is the correlation time of the CP and,

$$M_2^{IS} = \frac{1}{3} I(I+1) \sum (2\pi J_{IS}^{opt})^2 \tag{5}$$

is the second moment of the I–S heteronuclear spectrum due to J_{IS}^{opt}. Equation (5) indicates that M_2^{IS} is proportional to $(J_{IS}^{opt})^2$. Provided that J_{IS}^{opt} is proportional to P_{IR} and that τ_c is independent of J_{IS}^{opt}, equations (4) and (5) lead to the conclusion that $1/T_{IS}^{opt}$ is proportional to P_{IR}^2. The actual value of T_{IS}^{opt} in each batch is determined from the analysis of the functional form of $m_{I\to S}^{op,i}(P_{IR},\tau_{cp})$ (i = α, β, γ…). Here we evaluate it from the maximal position; T_{IS}^* is defined as the contact time at which the maximum is formed. Figure 2c shows $1/T_{IS}^*$ for the three series of maxima (α, β and γ) plotted against P_{IR}^2. The graph suggests that $1/T_{IS}^*$ is roughly proportional to P_{IR}^2, implying that J_{IS}^{opt} is proportional to P_{IR}.

This result provides a clue to the nature of the series of S-nuclei batches (α, β, γ…). Equation (5) indicates that the condition $M_2^{IS} \propto (J_{IS}^{opt})^2$ is fulfilled only when all I–S pairs participating in the summation of the right-hand side share the same J_{IS}^{opt}, such that J_{IS}^{opt} can be taken out of the summation Σ. Therefore, each series may be assigned to the polarization transfers to a batch of S-spins at the same distance from the I-spin at the origin. Figure 3 illustrates this situation. For example, the α-maxima may be assigned to the second nearest-neighbour S-spins, the β-maxima to the third, and so forth. It is reasonable that equivalent S-spins in the same order situated at the same distance from the I-spin share the same scalar coupling with it. Moreover, the contributions from nuclei in the same order to the correlation time are partially cancelled out[17,20,23]. Therefore, the assumption that τ_c is independent of J_{IS}^{opt} may be a reasonable approximation.

The result also provides us with information about the reach of J_{IS}^{opt}. The dotted red line in Figure 3 shows the P_{IR} dependence of $M_s(\tau_{cp})$ at a constant τ_{cp}. One finds a plateau-like feature around 80 mW, which indicates that the S-spins at the third nearest-neighbour sites participate in the process only when $P_{IR} > 80$ mW; that is, J_{IS}^{opt} can reach farther than D- and J_{IS}-couplings, as the latter two may not substantially reach the third-nearest neighbours.

Features such as the external switchability and the long reach may add variety to the qubit arrangement in semiconductor-based NMR quantum computers. Figure 4 shows an example. In an array of nuclear–spin qubits, a few lattice points apart from each other, the D-couplings are out of reach, so that the qubits are decoupled. Then, the present mechanism provides the external control of inter-nuclear couplings. As the light power is increased, the reach of couplings is extended. This would further enhance the flexibility of qubit arrangements.

This mechanism is compatible with most schemes proposed for semiconductor-based NMR quantum computing. The implantation of nuclear spin arrays in semiconductors has been studied using various techniques such as scanning probe microscopes, ion beams, and isotope engineerings[24–26]. These techniques will provide promising technologies to implement the schemes shown in Figure 4.

In conclusion, we have discovered an optically switchable indirect nuclear spin–spin coupling, which is manifested in CP experiments with GaAs under light illumination. As the strength of this coupling is externally controllable through light power, we expect it to have an essential role in the quantum gate operations of solid-state NMR quantum computers in the future.

Methods

Optical pumping double resonance NMR system and the sample. The CP experiments were performed at 10 K using an optical-pumping double-resonance NMR system developed for this study. The system consists of an NMR spectrometer, a laser system and a cryostat loaded in a 6.34-T superconducting magnet. A custom-built double-resonance probe is installed inside the cryostat. The sample used in this study is an undoped semi-insulating GaAs single-crystal wafer with a thickness of 600 μm and a crystal orientation of (100) (Mitsubishi Chemical). It is mounted on a sample stage made of sapphire located at the probe head and set with the surface normal to the magnetic field. The sample stage is cooled through thermal contact with the cold head of the cryostat. Infrared light emitted from a Ti:Sapphire laser is delivered to the cryostat through a polarization-maintaining fibre[27]. It is converted to circularly polarized light by a quarter-wave plate at the probe head, and applied to the sample in parallel to the magnetic field. The spot size at the sample surface is about ϕ5 mm.

Pulse sequence. The pulse sequence used is shown in Figure 5. The magnetization of I-spins, saturated by the first comb pulse, is regenerated during the time interval

τ_L and transferred to *S*-spins through the CP immediately thereafter. The infrared light is irradiated at a constant strength P_{IR} throughout the sequence. The photon energy of 1.50 eV (near the band gap) and the helicity σ^- were selected so that the optical pumping NMR signal enhancements for both ^{71}Ga and ^{75}As were nearly maximal. The experiment in the dark (Fig. 1) was obtained with the same pulse sequence as that in Figure 5, with the exception that $P_{IR} = 0$ mW.

References

1. Chuang, I. L., Gershenfeld, N. & Kubinec, M. Experimental implementation of fast quantum searching. *Phys. Rev. Lett.* **80,** 3408–3411 (1998).
2. Jones, J. A. & Mosca, M. Implementation of a quantum algorithm on a nuclear magnetic resonance quantum computer. *J. Chem. Phys.* **109,** 1648–1653 (1998).
3. Vandersypen, L. M. K., Steffen, M., Breyta, G., Yannoni, C. S., Sherwood, M. H. & Chuang, I. L. Experimental realization of Shor's quantum factoring algorithm using nuclear magnetic resonance. *Nature* **414,** 883–887 (2001).
4. Kane, B. E. A silicon-based nuclear spin quantum computer. *Nature* **393,** 133–137 (1998).
5. Shimizu, T., Goto, A., Hashi, K. & Ohki, S. An NMR quantum computer of the semiconductor CdTe. *Superlattice Microst.* **32,** 313–316 (2002).
6. Ladd, T. D., Goldman, J. R., Yamaguchi, F., Yamamoto, Y., Abe, E. & Itoh, K. M. All-silicon quantum computer. *Phys. Rev. Lett.* **89,** 017901 (2002).
7. DiVincenzo, D. P. Two-qubit gates are universal for quantum computation. *Phys. Rev. A* **51,** 1015–1022 (1995).
8. Tycko, R. & Reimer, J. A. Optical pumping in solid state nuclear magnetic resonance. *J. Phys. Chem.* **100,** 13240–13250 (1996).
9. Hayes, S. E., Mui, S. & Ramaswamy, K. Optically pumped nuclear magnetic resonance of semiconductors. *J. Chem. Phys.* **128,** 052203 (2008).
10. Doronin, S. I. Multiple quantum spin dynamics of entanglement. *Phys. Rev. A* **68,** 052306 (2003).
11. Rufeil-Fiori, E., Sanchez, C. M., Oliva, F. Y., Pastawski, H. M. & Levstein, P. R. Effective one-body dynamics in multiple-quantum NMR experiments. *Phys. Rev. A* **79,** 032324 (2009).
12. Michal, C. A. & Tycko, R. Nuclear spin polarization transfer with a single radio-frequency field in optically pumped indium phosphide. *Phys. Rev. Lett.* **81,** 3988–3991 (1998).
13. Tycko, R. Optical pumping of dipolar order in a coupled nuclear spin system. *Mol. Phys.* **95,** 1169–1176 (1998).
14. Patel, A. & Bowers, C. R. Two-dimensional nuclear magnetic resonance spectroscopy in optically pumped semiconductors. *Chem. Phys. Lett.* **397,** 96–100 (2004).
15. Goto, A., Shimizu, T., Hashi, K., Kitazawa, H. & Ohki, S. Decoupling-free NMR quantum computer on a quantum spin chain. *Phys. Rev. A* **67,** 022312 (2003).
16. Tomaselli, M., deGraw, D., Yarger, J. L., Augustine, M. P. & Pines, A. Scalar and anisotropic *J* interactions in undoped InP: a triple-resonance NMR study. *Phys. Rev. B* **58,** 8627–8633 (1998).
17. Goto, A., Hashi, K., Shimizu, T. & Ohki, S. Dynamics of electron-nuclear and heteronuclear polarization transfers in optically oriented semi-insulating InP: Fe. *Phys. Rev. B* **77,** 115203 (2008).
18. Muller, L., Kumar, A., Baumann, T. & Ernst, R. R. Transient oscillations in NMR cross-polarization experiments in solids. *Phys. Rev. Lett.* **32,** 1402–1406 (1974).
19. Hester, R. K., Ackerman, J. L., Cross, V. R. & Waugh, J. S. Resolved dipolar coupling spectra of dilute nuclear spins in solids. *Phys. Rev. Lett.* **34,** 993–995 (1975).
20. Mehring, M. *Principles of High Resolution NMR in Solids* (Springer, 1983).
21. Iijima, T., Hashi, K., Goto, A., Shimizu, T. & Ohki, S. Homonuclear and heteronuclear indirect spin-spin couplings in InP studied using ^{31}P cross polarization NMR spectra under magic-angle spinning. *Jpn. J. Appl. Phys. Part 2* **42,** L1411–L1413 (2003).
22. Ruderman, M. A. & Kittel, C. Indirect exchange coupling of nuclear magnetic moments by conduction electrons. *Phys. Rev.* **96,** 99–102 (1954).
23. Demco, D. E., Tegenfeldt, J. & Waugh, J. S. Dynamics of cross relaxation in nuclear magnetic double resonance. *Phys. Rev. B* **11,** 4133–4151 (1975).
24. Schenkel, T. Semiconductor physics: reliable performance. *Nature Mater.* **4,** 799–800 (2005).
25. Ruess, F. J. *et al.* Toward atomic-scale device fabrication in silicon using scanning probe microscope. *Nano Lett.* **4,** 1969–1973 (2004).
26. Itoh, K. M. An all-silicon linear chain NMR quantum computer. *Solid State Commun.* **133,** 747–752 (2005).
27. Goto, A., Ohki, S., Hashi, K. & Shimizu, T. Optical-pumping double-resonance NMR system for semiconductors. *Rev. Sci. Instrum.* **77,** 093904 (2006).

Acknowledgements

We acknowledge C. Takizawa for technical assistance. We also acknowledge High Magnetic Field Station (Tsukuba Magnet Laboratory), NIMS, and Niki Glass for their support. This work was partially supported by JST PRESTO program. K.H. was supported by a Grant-in-Aid for Scientific Research (No. 20540323) from the Japan Society for the Promotion of Science.

Author contributions

A.G. conceived and designed the experiments. All the authors jointly designed the system for the experiments, and A.G. and S.O. constructed it. A.G. carried out the main experiments. All the authors were involved in the analyses. A.G. wrote the paper, with the help of the co-authors.

Additional information

Competing financial interests: The authors declare no competing financial interests.

Reprints and permission information is available online at http://npg.nature.com/reprintsandpermissions/

How to cite this article: Goto, A. *et al.* Optical switching of nuclear spin–spin couplings in semiconductors. *Nat. Commun.* 2:378 doi: 10.1038/ncomms1378 (2011).

SCIENTIFIC REPORTS

OPEN

SUBJECT AREAS:
APPLIED PHYSICS
NANOTECHNOLOGY
NANOPARTICLES
NANOBIOTECHNOLOGY

Received
8 July 2011

Accepted
28 October 2011

Published
15 November 2011

Correspondence and requests for materials should be addressed to H.M. (MAMIYA.Hiroaki@nims.go.jp)

Hyperthermic effects of dissipative structures of magnetic nanoparticles in large alternating magnetic fields

Hiroaki Mamiya[1] & Balachandran Jeyadevan[2]

[1]National Institute for Materials Science, Tsukuba 305-0047, Japan, [2]The University of Shiga Prefecture, Hikone 522-8533 Japan.

Targeted hyperthermia treatment using magnetic nanoparticles is a promising cancer therapy. However, the mechanisms of heat dissipation in the large alternating magnetic field used during such treatment have not been clarified. In this study, we numerically compared the magnetic loss in rotatable nanoparticles in aqueous media with that of non-rotatable nanoparticles anchored to localised structures. In the former, the relaxation loss in superparamagnetic nanoparticles has a secondary maximum because of slow rotation of the magnetic easy axis of each nanoparticle in the large field in addition to the known primary maximum caused by rapid Néel relaxation. Irradiation of rotatable ferromagnetic nanoparticles with a high-frequency axial field generates structures oriented in a longitudinal or planar direction irrespective of the free energy. Consequently, these dissipative structures significantly affect the conditions for maximum hysteresis loss. These findings shed new light on the design of targeted magnetic hyperthermia treatments.

Tumour-targeted magnetic hyperthermia has recently attracted much attention[1]. Preferential accumulation of magnetic nanoparticles in tumour tissue is achieved by conjugating nanoparticles with tumour-homing peptides[2] or antibodies[3]. When the accumulated nanoparticles are exposed to a large alternating magnetic field, $H = H_{ac}\sin(2\pi f \cdot t)$, where H_{ac} is the amplitude of the field, f is the frequency, and t is time, they begin to rotate because of magnetic torque. Simultaneously, the direction of the magnetic moment, $\boldsymbol{\mu}$, in each nanoparticle reverses with a certain probability. Consequently, heat equivalent to the magnetic loss dissipates locally in the tumour tissue. If the properties of the irradiated field are limited (*i.e.*, $H_{ac} \cdot f <$ constant)[1] to ensure biomedical safety, then nanoparticles that maximise the *in vivo* efficiency of heat dissipation, $P_H/(H_{ac} \cdot f)$, are required, where P_H is the specific energy dissipation rate (specific loss power) per unit mass of nanoparticles. The actual rotations of the nanoparticles are disordered because the microviscosity of the local environment in cancer cells is not constant[4,5], and effective elasticity depends on the binding conditions between nanoparticles and membranes. To minimise the effect of irregular rotations in magnetic hyperthermia, two guiding principles have been proposed on the basis of simple models that consider a linear response of thermodynamic equilibrium states or magnetic field-driven reversals.

The first guiding principle[6] is to use the relaxation loss in superparamagnetic iron oxide nanoparticles (SPIONs) with a sufficiently low energy barrier ΔU for reversal. If a linear response of their thermodynamic equilibrium state is considered at low H_{ac}, the out-of-phase component of AC susceptibility χ'' can be expressed as follows:

$$\chi'' = \chi_0 \cdot (2\pi f \cdot \tau) / \left[1 + (2\pi f \cdot \tau)^2\right], \tag{1}$$

where χ_0 is the initial susceptibility per unit mass of SPIONs. When reversal and rotation occur in a nanoparticle in parallel, the characteristic time τ is given by the following equation:

$$\tau^{-1} = \tau_N^{-1} + \tau_B^{-1}, \tag{2}$$

where τ_N is the Néel relaxation time for reversal, and τ_B is the Brownian relaxation time for rotation. Consequently, the heating efficiency $P_H/(H_{ac} \cdot f) = \pi\mu_0\chi'' \cdot H_{ac}$ for individual monodisperse nanoparticles has a single maximum at the peak frequency $2\pi f_p = \tau^{-1}$. For a sufficiently small SPION, τ is determined only by τ_N because τ_N is much shorter than τ_B. In this case, it has been assumed that the conditions for maximising the efficiency are unaffected by uncontrolled rotation of the nanoparticles.

However, in some experiments, dual peaks have been observed for the frequency dependence of $\chi'' \propto P_H/(H_{ac} \cdot f)$[7,8] despite the prediction of a single peak at a $2\pi f_p$ value of τ^{-1} ($= \tau_N^{-1} + \tau_B^{-1}$). For this reason, size

distribution[7] or aggregation[8] of the nanoparticles was considered based on the linear response theory. In an earlier study[7], the low-frequency peak observed for the susceptibility was attributed to Brownian relaxation of larger nanoparticles, while the high-frequency peak was attributed to Néel relaxation of smaller nanoparticles. In another study[8], the low- and high-frequency peaks were attributed to individual and agglomerated nanoparticles, respectively. Thus the observed dual peaks have been theoretically explained by the coexistence of two kinds of nanoparticles. In other words, these explanations are based on the assumption that a single kind of nanoparticle will produce only a single peak at τ^{-1} ($=\tau_N^{-1} + \tau_B^{-1}$). However, this assumption has never been theoretically verified under a large AC magnetic field, where the linear response theory does not hold.

The second guiding principle is to use hysteresis loss in ferromagnetic nanoparticles[9]. In mechanical models such as the Stoner–Wohlfarth model for single domain particles, $\boldsymbol{\mu}$ is reversed in the time scale of Larmor precession (picoseconds) when ΔU disappears at the switching field H_{sw}, because thermal fluctuations are not considered. Such fast reversals are considered to dominate the response to high frequency AC magnetic field because the Brownian relaxations of large ferromagnetic nanoparticles are generally slow compared with the oscillation of the field. In this case, the work done in one cycle is given by the area inside the hysteresis loop, $\zeta \cdot M_s \cdot H_{sw}$, where M_s is the spontaneous magnetisation and ζ is a coefficient related to the rectangularity of the loop. In the simple case of rectangular hysteresis loops, ζ is 0 for $H_{ac} < H_{sw}$ and 4 for $H_{ac} \geq H_{sw}$. Consequently, the maximum efficiency, $P_H/(H_{ac} \cdot f) = \zeta \cdot M_s \cdot (H_{sw}/H_{ac})/\rho$, where ρ is the density of magnetite, is achieved when H_{ac} is adjusted to H_{sw}. Because H_{sw} depends on the magnetic anisotropy field H_K specific to each nanoparticle, it has been assumed that, in cases where reversal is much faster than rotation, the amount of hysteresis loss is unaffected by the inhomogeneous rotations of nanoparticles in cancer cells.

In recent experimental studies[10,11], the observed P_H of immobilised ferromagnetic nanoparticles was lower than that of the same nanoparticles dispersed in a fluid. Kim *et al.*[10] attributed the difference to variation in the rates of convective heat transfer. Müller *et al.*[11] suggested that the orientation or agglomeration of the nanoparticles, or interaction effects, may be responsible for the observed difference. The orientation of nanoparticles is important because it is related to the magnetic torque intrinsic in rotatable ferromagnetic nanoparticles. However, there has been no theoretical study on magnetic field-driven reversals of $\boldsymbol{\mu}$ in ferromagnetic nanoparticles with easy axes that simultaneously rotate under the magnetic torque.

There are many reported inconsistencies between experimental results and predictions based on the above two guiding principles for optimising hyperthermia treatment. These guiding principles are based on the simple models established at the two limits: in zero magnetic field or at zero temperature. Under the conditions for hyperthermia ($H_{ac} \neq 0$, $T \neq 0$), where T is temperature, the validity of the guiding principles has not been theoretically verified even for an ideal system of non-interacting monodisperse nanoparticles. Consequently, we attempted to simulate the thermally assisted magnetic response of individual superparamagnetic/ferromagnetic iron oxide nanoparticles exposed to a large AC magnetic field like that used in hyperthermia treatment. The simulation was performed in the following two extreme cases: non-rotatable nanoparticles strongly anchored to structures resembling organelles, and rotatable nanoparticles in an aqueous phase mimicking cytoplasm. In the simulations, the thermally activated reversals of $\boldsymbol{\mu}$ were calculated between the meta-stable directions. Simultaneously, the rotations of the spheroidal nanoparticles were computed in the inertialess limit (Brownian dynamics simulation), where the frictional torque always balances with magnetic torque and with Brownian torque (details are reported in the Methods section). The results allow examination of whether the relaxation loss for $\tau_N \ll \tau_B$ and the hysteresis loss at $H_{ac} \approx H_{sw}$ are independent of the ability of the nanoparticles to rotate under the conditions for hyperthermia treatment.

Results

The magnetic response to an AC magnetic field $H_{ac}\sin(2\pi f \cdot t)$ at T = 310 K was simulated for individual monodisperse spheroidal magnetite nanoparticles with non-magnetic surfactant layers in non-rotatable and rotatable situations (see the Methods section for details). Results are presented for the following representative nanoparticles: nearly spherical nanoparticles with an aspect ratio, $\boldsymbol{\kappa}$, of 1.1 and an equatorial diameter, $2R_M$, of 18 nm, and elongated spheroidal particles with $\boldsymbol{\kappa} =$ 1.4 and $2R_M$ = 24 nm. The parameters of these nanoparticles are summarised in Table 1. The former nanoparticles with τ_N (H_{ac}=0) of 20 ns can be considered as typical SPIONs, while the latter with τ_N ($H_{ac} = 0$) of 2×10^7 s (1 year) can be regarded as typical ferromagnetic nanoparticles in the frequency range of hyperthermia treatment ($(2\pi f)^{-1}$ of approximately 1 μs). Results for nanoparticles with other sizes and shapes are shown in the Supplementary Information.

The magnetisation curves of the non-rotatable nearly spherical nanoparticles at low H_{ac} (1 kA/m) are shown in Fig. 1. A linear response without hysteresis was observed at f = 100 kHz. Such superparamagnetic behaviour is reasonable because the estimated $\tau_N(H_{ac} = 0)$ for the nanoparticles is 20 ns. Hysteresis appeared in the curves at f = 1,000 kHz. As f increased further, the area inside the hysteresis loop grew. This area corresponds to the work done in one cycle. Therefore, $P_H/(H_{ac} \cdot f)$ also increased with f, and a single maximum was observed at a peak frequency, f_p, of 10,000 kHz (Fig. 1 (b)). Figure 2(a) shows the H_{ac} dependence using a contour plot of $P_H/(H_{ac} \cdot f)$. As H_{ac} increased, f_p shifted towards higher frequencies. As indicated by the dashed line in Fig. 2(a), this shift can be explained by the values of $\tau_N(H_{ac})$ calculated using the conventional Brown's equation as follows[12]:

$$[\tau_N(H_{ac})]^{-1} = f_0 \cdot (1-h^2)\left\{(1+h)\exp\left[(-K_d V/k_B T)(1+h)^2\right] + (1-h)\exp\left[(-K_d V/k_B T)(1-h)^2\right]\right\}, \quad (3)$$

where h is $\mu H/(2\ K_d V)$, K_d is the shape anisotropy constant, V is the volume of the magnetic core, and k_B is the Boltzmann constant. Therefore, the emergence of a single peak in $P_H/(H_{ac} \cdot f)$ can be attributed to Néel relaxation loss, as expected for SPIONs.

For the nearly spherical nanoparticles with a low H_{ac} (1 kA/m), the magnetisation curves in the rotatable case were the same as those in the non-rotatable case (see Fig. 1). An equivalent maximum appeared in the f-dependence of $P_H/(H_{ac} \cdot f)$ in the linear response

Table 1 | Parameters of the simulated nanoparticles: including the aspect ratio κ, equatorial diameter $2R_M$, thickness of the surfactant layer δR, density of magnetite ρ, spontaneous magnetisation M_s, anisotropy field H_K, viscosity η, Néel relaxation time $\tau_N(H = 0)$, and Brownian relaxation time τ_B. The value of $\tau_N(H = 0)$ was estimated using equation (3), while the value of τ_B was estimated using equation (4).

	κ	$2R_M$ (nm)	δR (nm)	ρ (kg/m^3)	M_s (kA/m)	H_K (kA/m)	η (mPa s)	$\tau_N(H = 0)$ (sec)	τ_B (sec)
Nearly spherical nanoparticle	1.1	18	4.5	5200	450	17	1.0 / ∞	2×10^{-8}	8×10^{-6}
Elongated spheroidal nanoparticle	1.4	24	6.0	5200	450	57	1.0 / ∞	2×10^{7}	2×10^{-5}

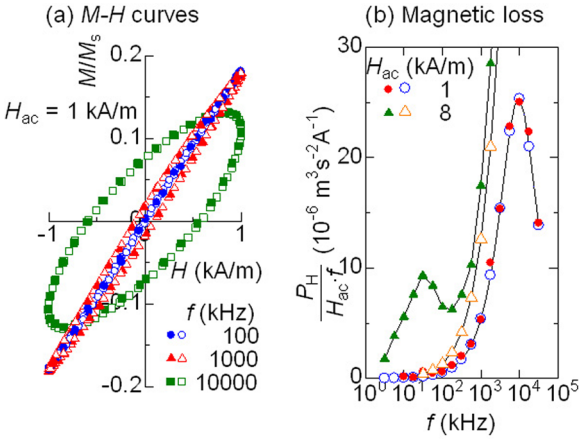

Figure 1 | Magnetic response of nearly spherical nanoparticles (typical SPIONs). The open and solid symbols show the values of non-rotatable and rotatable nanoparticles, respectively. (a) Steady magnetisation curves with low H_{ac} (1 kA/m) at various frequencies, (b) frequency dependence of the efficiency of heat dissipation with low and intermediate values of H_{ac}.

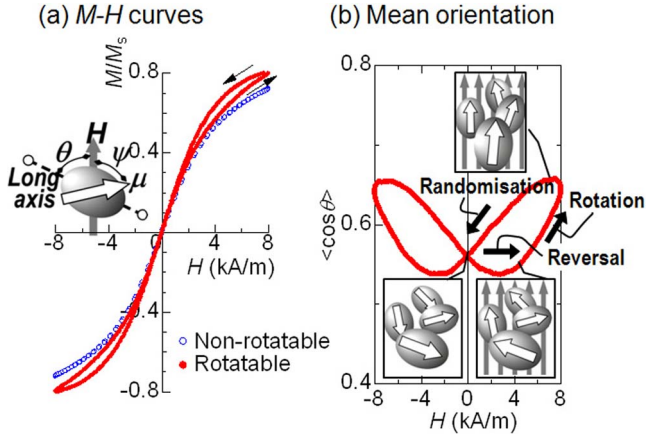

Figure 3 | Magnetic response of nearly spherical nanoparticles (typical SPIONs) with an applied AC field with H_{ac} = 8 kA/m and f = 30 kHz. (a) Steady magnetisation curves, (b) mean orientation of the long (easy) axis of the nanoparticles, <cosθ>. Orientations are indicated in the inset images.

range (H_{ac} = 1 kA/m) (Fig. 1(b)). This behaviour is consistent with the above assumption because the estimated τ_N (H_{ac} = 0) of 20 ns is much shorter than τ_B = 8 μs (Table 1). The shift of this peak with increasing H_{ac} is analogous to that in the non-rotatable case (Fig. 2(b)). However, another maximum of $P_H/(H_{ac}\cdot f)$ was observed at H_{ac} = 8−16 kA/m and f = 30 kHz in the contour plot shown in Fig. 2(b). A secondary maximum like this has not previously been theoretically predicted for individual monodisperse nanoparticles. Figure 3(a) shows the magnetisation curves calculated under these conditions. Unlike the non-rotatable case, an S-shaped hysteresis loop without remanence existed. At the same time, the mean orientation of the long (easy) axes of the nanoparticles showed butterfly-shaped hysteresis, as shown Fig. 3(b). Because such behaviour cannot be explained using the present linear response theory, its origin is discussed in the next section from the viewpoint of the rotation of the long axis of SPION.

The magnetisation curves at f = 10,000 kHz for the elongated spheroidal nanoparticles, which are typical ferromagnetic nanoparticles, in the non-rotatable case are shown in Fig. 4(a). The curve was reversible at H_{ac} = 20 kA/m, and hysteresis appeared in the curve at H_{ac} = 26 kA/m. As H_{ac} increased further, the area inside the hysteresis loop grew. When H_{ac} became larger than 32 kA/m, the expansion of the area was saturated and the shape of the magnetisation curve approached that predicted by the Stoner–Wohlfarth model. $P_H/(H_{ac}\cdot f)$ was almost zero at low H_{ac}, then at approximately 30 kA/m it began increasing rapidly with H_{ac}, followed by a gradual decreases with increases in H_{ac} (Fig. 4(b)). This behaviour depends weakly on the frequency (Fig. 5(a)). In mechanical models that do not consider thermal fluctuation, a hysteresis loop appeared when H_{ac} was higher than H_{sw}. Because H_{sw} of ferromagnetic nanoparticles with randomly oriented easy axes ranges from $H_K/2$ = 29 kA/m to H_K = 57 kA/m, and is often close to 0.5 H_K, that $P_H/(H_{ac}\cdot f)$ is almost independent of frequency at H_{ac} > 30 kA/m in the non-rotatable

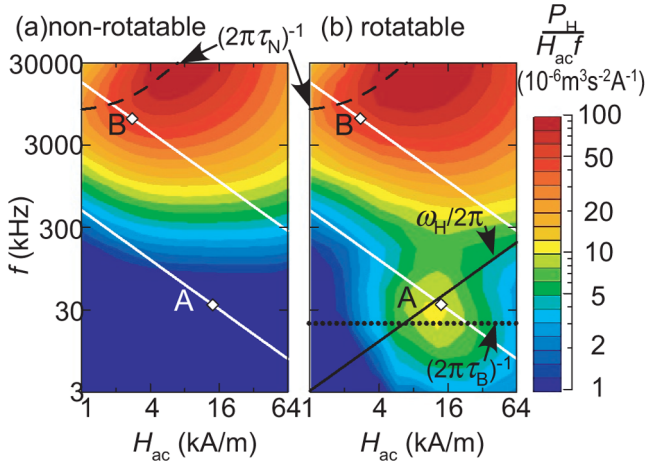

Figure 2 | Efficiency of heat dissipation in the nearly spherical nanoparticles (typical SPIONs) that are (a) non-rotatable and (b) rotatable, where P_H is the specific energy dissipation rate. Dashed lines represent the Néel relaxation time $(2\pi\tau_N)^{-1}$, dotted lines show the Brownian relaxation time $(2\pi\tau_B)^{-1}$, and solid lines indicate typical angular velocity, $\omega_H(H = H_{ac}, \psi = \pi/4)/2\pi$, of the rotation caused by magnetic torque. White lines show the thresholds for biomedical safety. Diamonds A and B on the white lines denote the conditions for maximum $P_H/(H_{ac}\cdot f)$ in the rotatable nanoparticles.

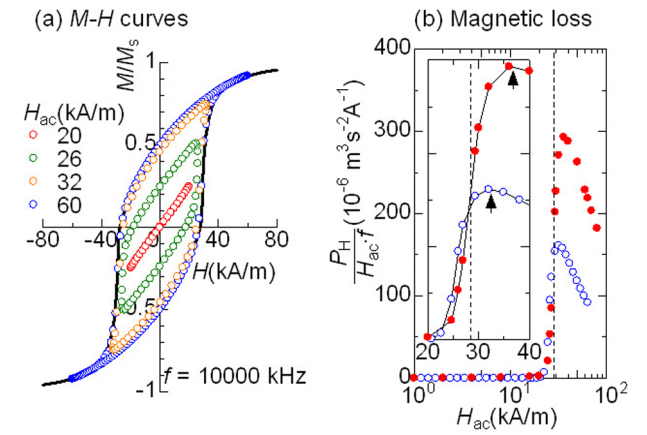

Figure 4 | Magnetic response of elongated spheroidal nanoparticles (typical ferromagnetic nanoparticles) in high-frequency AC fields with f = 10 000 kHz and various values of H_{ac}. (a) Steady magnetisation curves in the non-rotatable case; the corresponding curves for rotatable nanoparticles are presented in Fig. 6(a) and (b). Solid lines indicate Stoner–Wohlfarth model curves. (b) H_{ac}−dependence of the efficiency of heat dissipation. The open and solid symbols show the values of the non-rotatable and rotatable nanoparticles, respectively. The arrows indicate the peak maxima of $P_H/(H_{ac}\cdot f)$ in both cases, and the broken line shows half of the anisotropic field, $H_K/2$. The inset shows an enlarged view.

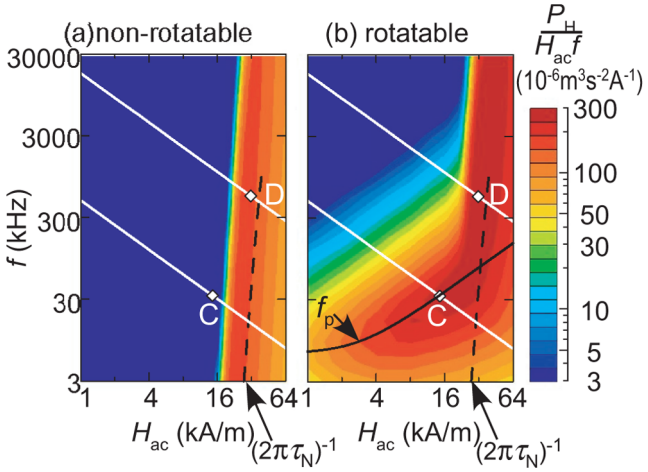

Figure 5 | Efficiency of heat dissipation of elongated spheroidal nanoparticles (typical ferromagnetic nanoparticles) that are (a) non-rotatable and (b) rotatable. Dashed lines represent the Néel relaxation time $(2\pi\tau_N)^{-1}$ and the solid line indicates f_p, which was calculated using equation (5). White lines show the thresholds for biomedical safety. Diamonds C and D on the white lines denote the conditions for maximum $P_H/(H_{ac}\cdot f)$ in the rotatable nanoparticles.

ferromagnetic nanoparticles is consistent with the properties expected for the hysteresis loss.

Figure 6 shows the magnetisation curves for rotatable elongated spheroidal nanoparticles at f = 10,000 kHz. Because the magnetic response slowly changed after the AC magnetic field was applied at t = 0, transient variations of the hysteresis loops are observed. The shape of the major hysteresis loop at H_{ac} = 60 kA/m was initially consistent with that predicted by the Stoner–Wohlfarth model with randomly oriented easy axes. However, the remanence of the major loop gradually increased from 0.5 M_s to M_s. In other words, the major loop became squarer, and the area inside the loop increased with time. In comparison, the remanence of the minor loop at H_{ac} = 26 kA/m gradually decreased and the area became smaller over time. As shown in Fig. 6(c) and (d), the long (easy) axes of the nanoparticles gradually turned when the variations of the loops proceeded (see the next section for details). Consequently, the increased area of the major hysteresis loops and decreased area of the minor loops caused the maximum of $P_H/(H_{ac}\cdot f)$ to shift towards higher H_{ac} compared with the non-rotatable case (see arrows in Fig. 4(b)). Note that reversals occurred every hundred nanoseconds ($\sim 1/f$), while rotations took several microseconds (Fig. 6(c)). Thus, the assumption that the amount of hysteresis loss is unaffected by the rotation of nanoparticles when reversal is significantly faster is invalid for ferromagnetic nanoparticles in large AC magnetic fields at high frequencies.

Before discussing this novel phenomenon observed at high frequencies, the other important variation in the contour plot of $P_H/(H_{ac}\cdot f)$ (Fig. 5) that occurred because of the ability of the ferromagnetic nanoparticles to rotate at lower frequencies shall be examined. The maximum of $P_H/(H_{ac}\cdot f)$ shifted toward lower H_{ac} below 100 kHz for the rotatable elongated spheroidal nanoparticles, while it stayed between $H_K/2$ and H_K in the non-rotatable case. Figure 7(a) shows the magnetisation curve obtained when H_{ac} = 16 kA/m and f = 30 kHz. The curve in the rotatable case had an obvious hysteresis loop with a large remanence in the steady state, but there was no hysteresis observed for the non-rotatable situation. Because H_{ac} = 16 kA/m is much smaller than $H_K/2$, no reversals of $\boldsymbol{\mu}$ occur at any orientation of the easy axis so hysteresis is not observed for the latter case. Figure 7(b) shows the variation of $<\cos\theta>$ in the rotatable case, where $<\cos\theta>$ $(0 < \theta < \pi/2)$ is the mean angle between

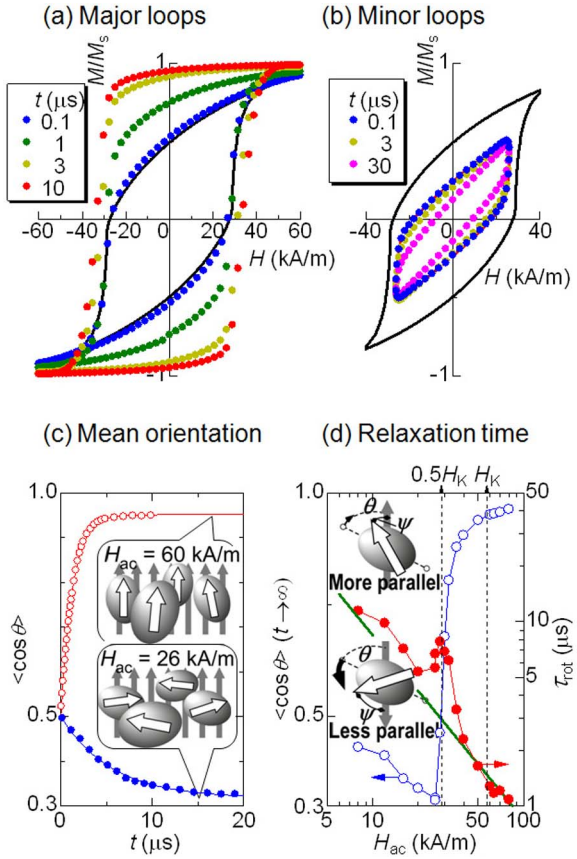

Figure 6 | Magnetic response of elongated spheroidal nanoparticles (typical ferromagnetic nanoparticles) in high-frequency AC fields with f = 10 000 kHz and various values of H_{ac}. (a) Transient major hysteresis loops of the rotatable nanoparticles after application of a field with H_{ac} = 60 kA/m at t = 0. (b) Transient minor loops of the rotatable nanoparticles after application of a field with H_{ac} = 26 kA/m at t = 0. Solid lines indicate Stoner–Wohlfarth model curves. (c) Relaxation of the mean orientation of the long axis, $<\cos\theta>$, (d) steady values of $<\cos\theta>$ and relaxation time τ_{rot}. Dashed lines in (d) show $H_K/2$ and H_K; and the solid line in (d) indicates the reciprocal, $[\omega_H(H=H_{ac}\sin\psi=0.43)]^{-1}$, of the typical angular velocity of rotation caused by magnetic torque. Orientations are indicated in the inset images.

the magnetic field and the long axes of the spheroidal nanoparticles. Note that $<\cos\theta>$ is synchronised with $|M/M_s| = |\cos\psi|$, where ψ is the angle between $\boldsymbol{\mu}$ and $\boldsymbol{H}$. This fact indicates that the hysteresis in the rotatable case (Fig 7(a)) is mainly caused by the rotation of the easy axis where the direction of $\boldsymbol{\mu}$ is fixed. Consequently, heat equivalent to the hysteresis loss dissipates even at $H_{ac} < H_K/2$.

For Brownian relaxation, τ_B can be expressed as follows:

$$\tau_B = (3\eta V_H\cdot(0.8+0.2\kappa)/(k_B T)), \tag{4}$$

where η is the viscosity of the surrounding medium, and V_H is the hydrodynamic volume. In equation (4), the frictional torque for spheroids, described in the Methods section, is considered. For the elongated spheroidal nanoparticle, $(2\pi\tau_B)^{-1}$ is calculated to be 8 kHz. This value is too low to cause the nanoparticle to rotate at 30 kHz. Therefore, Yoshida *et al.*[13] also took into account the rotation caused by magnetic torque, $\boldsymbol{\mu}(t)\times\boldsymbol{H}(t)$. They concluded that the area of the hysteresis loop was maximised as follows:

$$2\pi f_p = \tau_B^{-1}\left[1+0.07(\mu H_{ac}/k_B T)^2\right]^{0.5}. \tag{5}$$

The location of the peak in $P_H/(H_{ac}\cdot f)$ below 100 kHz can be explained by this equation, as shown in Fig. 5(b). An expression that describes all of the variation in the position of the primary peak of

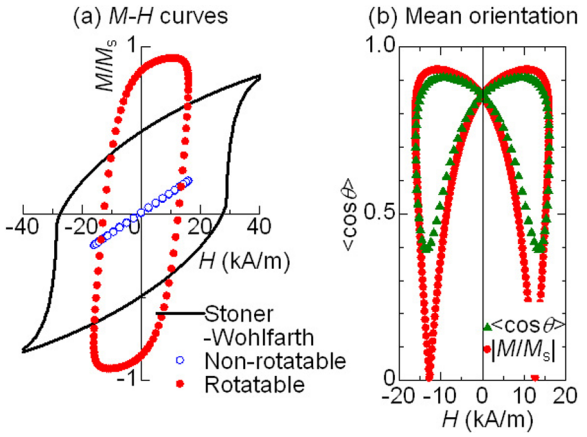

Figure 7 | Magnetic response of elongated spheroidal nanoparticles (typical ferromagnetic nanoparticles) in a low-frequency AC field with $f = 30$ kHz and $H_{ac} = 16$ kA/m. (a) Steady magnetisation curves, where the open and solid symbols show the values of the non-rotatable and rotatable nanoparticles, respectively. Solid lines are Stoner–Wohlfarth model curves. (b) Mean orientation of the long (easy) axis of nanoparticles, $<\cos\theta>$.

$P_H/(H_{ac}\cdot f)$ is desirable, and equation (5) can be rewritten as follows:

$$2\pi f_p \sim [\tau_N(H_{ac})]^{-1} + \tau_B^{-1}\left[1+0.07(\mu H_{ac}/k_B T)^2\right]^{0.5}. \quad (6)$$

This equation is an extended relationship of $\tau^{-1} = \tau_N^{-1} + \tau_B^{-1}$ for a large AC magnetic field. This expression is for the primary maximum; the secondary maximum is discussed later. The second term of equation (6) can be approximated to $0.1\mu H_{ac}/(\eta V_H)$ for $\mu H_{ac}/k_B T \gg (0.07)^{-0.5}$ and $\kappa \sim 1$. On the other hand, $\tau_N(H_{ac})$ of ferromagnetic nanoparticles becomes extremely short only when the energy barrier disappears between $H_K/2$ and H_K. Therefore, the changeover between the two terms in the equation (6) generally occurs at $H_{ac} \approx H_K/2$ and $2\pi f \approx 0.1\mu H_K/(2\eta V_H) = 0.1\ K_d V/(\eta V_H)$. For the elongated spheroidal particles ($\kappa = 1.4$, $K_d = 16$ kJ/m^3, and $V/V_H = 0.3$) in a liquid phase with $\eta = 1$ mPa·s, the values of H_{ac} and f are 29 kA/m and 76 kHz. Such a changeover around 100 kHz occurs for ferromagnetic nanoparticles of any size, as long as the conditions, K_d, V/V_H, and η, are constant. We must keep in mind that, even when ferromagnetic nanoparticles are large enough for their Brownian relaxation to be negligible, the magnetic torque caused by the large AC magnetic field can easily rotate such nanoparticles in the liquid phase at a time scale of microseconds. This knowledge is helpful when considering the frequency for hyperthermia treatment, even if it is obtained for a simplified system.

In summary, most of the simulated results, including significant variations for ferromagnetic nanoparticles exposed to a low-frequency AC magnetic field, can be explained using the existing models. The two essential exceptions are as follows:
(a) a secondary maximum in the relaxation loss for SPIONs exposed to a low-frequency AC magnetic field, and
(b) a shift of the maximum hysteresis loss caused by the ability of typical ferromagnetic nanoparticles exposed to a high-frequency AC magnetic field to rotate.
These novel phenomena are discussed in detail in the following section.

Discussion

The two novel phenomena of rotatable nanoparticles in a large AC magnetic field described above cannot be explained by simple models that consider a linear response of thermodynamic equilibrium states or magnetic field-driven reversals. In this section, we shall further discuss these atypical responses from the viewpoint of the orientation of the long (easy) axis. First, we begin with the appearance of a secondary maximum of $P_H/(H_{ac}\cdot f)$ near $H_{ac} = 8$ kA/m and $f = 30$ kHz for the nearly spherical nanoparticles (typical SPIONs) where an S-shaped hysteresis loop without remanence was obtained (Fig. 3). We must recall that the variation in $<\cos\theta>$ showed butterfly-shaped hysteresis under these conditions. This behaviour explains the atypical magnetic response in the period f^{-1} (33 μs) (Fig. 3(b)). Initially (at $t = 0$), no magnetisation exists because the occupation probabilities of $\boldsymbol{\mu}$ in the two stable directions parallel to the long (easy) axis are equalised in a zero magnetic field. As H increases, the occupation probability in the more stabilised direction immediately increases because of reversals on a time scale of τ_N (≤ 20 ns). The reversed $\boldsymbol{\mu}$ in the stabilised direction is not completely parallel to $\boldsymbol{H}$, $\psi \neq 0$, and the magnetic torque $\mu H \sin\psi$ turns the long (easy) axis towards the direction of the field. If we neglect Brownian torque $\boldsymbol{\lambda}(t)$ (see equation (11) in the Methods section), the angular velocity of the rotation due to magnetic torque can be expressed as

$$\omega_H(H(t), \psi(t)) = [\mu H(t)\sin\psi(t)]/[6\eta V_H\cdot(0.8+0.2\kappa)]. \quad (7)$$

Hence, $\omega_H(H(t), \psi(t))$ increases in proportion to the field amplitude $H = H_{ac}\sin(2\pi f\cdot t)$. For example, $\omega_H(H, \psi = \pi/4)$ is 0.15×10^6 rad/s when H ($t = 1/4f \approx 8$ μs) is 8 kA/m. Therefore, rotation is not negligible in the peak period of the oscillations of H. Subsequently, H decreases to zero at $t = 1/2f \approx 17$ μs, and the occupation probabilities are again equalised because reversal is rapid, so the magnetic torque disappears. Alternatively, the Brownian torque randomises the orientation of the long axis on a time scale of τ_B (= 8 μs). Therefore, competition between the magnetic and Brownian torques can cause the butterfly-shaped hysteresis of $<\cos\theta>$. Because the equilibrium magnetisation of SPIONs with easy axes parallel to $\boldsymbol{H}$ is higher than that of randomly oriented SPIONs[14], the magnetisation curve shows hysteresis without remanence. Consequently, a secondary maximum appears for the rotatable SPIONs even though $\tau_N \ll \tau_B$.

Next, we investigate the influence of the ability of elongated spheroidal nanoparticles to rotate under a high-frequency AC magnetic field on the shift of the maximum $P_H/(H_{ac}\cdot f)$. As shown in Fig. 6(a) and (b), the magnetisation curves varied after an AC magnetic field was applied at $t = 0$. At the same time, transient variations also occurred in $<\cos\theta>$, as shown in Fig. 6(c). In the case of the major loop at $H_{ac} = 60$ kA/m, $<\cos\theta>$ gradually increased from 0.5 to 0.95. In other words, the long (easy) axis became oriented towards the direction parallel to $\boldsymbol{H}$. The characteristic time, τ_{rot}, was estimated to be 1.3 μs using the approximation of exponential decay. Note that the direction of $\boldsymbol{\mu}$ is not completely parallel to $\boldsymbol{H}$ even for $H \geq H_K$, even though $\boldsymbol{\mu}$ is already reversed for all of the nanoparticles. Because $\sin\psi$ is 0.43 when $\cos\psi$ is 0.9, a large magnetic torque can turn the long axis even if the magnetisation is almost saturated after reversals at $H \sim H_K$. Indeed, τ_{rot} at $H_{ac} \geq H_K$ is comparable to the reciprocal of typical values of $\omega_H(H = H_{ac}, \sin\psi = 0.43)$ (Fig. 6(d)). Therefore, these transient variations can be attributed to the longitudinal orientation being adopted preferentially because of the magnetic torque.

In the minor loops at $H_{ac} = 26$ kA/m, the remanence of the rotatable nanoparticles decreased gradually with time (Fig. 6(b)) and $<\cos\theta>$ simultaneously decreased from 0.5 (Fig. 6(c)). The long axis was oriented perpendicular to $\boldsymbol{H}$ during this period, although the longitudinal orientation is preferred when the Zeeman energy is considered. It should be noted that the angle ψ for $\boldsymbol{\mu}$ in a stable direction more parallel to $\boldsymbol{H}$ is smaller than that in a metastable direction less parallel to $\boldsymbol{H}$ (Fig. 6(d)). In other words, the magnitude of the magnetic torque toward the longitudinal orientation in the former is weaker than that toward the perpendicular orientation in the latter. This difference makes the orientation of the long axis planar on average, because the stable and metastable states alternate every half period when the reversal of $\boldsymbol{\mu}$ is blocked in the minor loop. These arguments suggest that the slowing of the rotation for

$0.5\ H_K \leq H_{ac} \leq H_K$ (Fig. 6(d)) can be attributed to compensation between two magnetic torques in the intermediate range. Briefly, in ferromagnetic nanoparticles in the aqueous phase, longitudinal or planar orientations are adopted, irrespective of the free energy, as dissipative structures under a high-frequency AC magnetic field. Consequently, $P_H/(H_{ac}\cdot f)$ increases gradually in major hysteresis loops and decreases in minor loops. These variations cause the maximum of $P_H/(H_{ac}\cdot f)$ to shift towards higher H_{ac}.

Finally, we return to the contour plots of $P_H/(H_{ac}\cdot f)$ in Figs. 2 and 5, and discuss the effect of rotation on the design for maximising $P_H/(H_{ac}\cdot f)$. If a safety limit of $H_{ac}\cdot f < 4.85\times10^8\ \mathrm{Am^{-1}s^{-1}}$ is applied[9], then maximum values of $P_H/(H_{ac}\cdot f)$ for rotatable SPIONs and ferromagnetic nanoparticles are obtained at the conditions shown by diamonds A and C in Figs. 2(b) and 5(b), respectively. However, no heat dissipation occurs under the same conditions (A and C) if the rotation of these nanoparticles is blocked (Figs. 2(a) and 5(a)). If a highly amplified AC magnetic field $H_{ac}\cdot f$ of $1.74\times10^{10}\ \mathrm{Am^{-1}s^{-1}}$ is allowed[15], a maximum $P_H/(H_{ac}\cdot f)$ of $3.0\times10^{-4}\ \mathrm{m^{-3}s^{-2}A^{-1}}$ (5.2 MW/kg) for the rotatable ferromagnetic nanoparticles can be obtained (diamond D in Fig. 5(b)). However, $P_H/(H_{ac}\cdot f)$ halves when the rotation of these nanoparticles is blocked (Fig. 5(a)) because oriented structures are not formed. In contrast, condition B for the primary maximum of $P_H/(H_{ac}\cdot f)$ in the rotatable SPIONs remains the optimum condition when these nanoparticles cannot rotate (Fig. 2(a) and (b)). This is because the long (easy) axes of SPIONs are randomly oriented in rotatable SPIONs as Brownian torque has more effect than magnetic torque in a weak magnetic field. As demonstrated here, rotation generated by the magnetic torque caused by a large alternating magnetic field greatly affects the conditions for maximising heat dissipation in magnetic nanoparticles.

In this study, we simulated the magnetic responses of superparamagnetic and ferromagnetic magnetite nanoparticles in a large alternating magnetic field. The results show that both the relaxation loss for $\tau_N \ll \tau_B$ and the hysteresis loss at $H_{ac} \approx H_{sw}$ are affected by the formation of dissipative structures because of the ability of nanoparticles to rotate. Consequently, the conditions for maximising heat dissipation depend strongly on the inhomogeneous microviscosity of the surrounding medium.

Compared with the simplified model used for our simulation, actual magnetic nanoparticles used for targeted magnetic hyperthermia treatment are not ideal. For this reason, the factors affecting more realistic situations need to be evaluated. First, the effects of crystalline and surface anisotropy energy are considered. In this case, the potential energy with respect to the direction of $\boldsymbol{\mu}$ is complicated. Even if multiple valleys appear in the energy surface, the easy axes are not parallel to $\boldsymbol{H}$, because the orientations of the nanoparticles are randomised by Brownian torque in the liquid phase. For this reason, slow rotations inevitably occur after fast reversals because of the magnetic torque in an AC magnetic field. These rotations lead to secondary relaxation loss in SPIONs in a low frequency AC magnetic field and shift the hysteresis loss in ferromagnetic nanoparticles in a high frequency AC magnetic field. Next, the variation in the size and shape of actual nanomagnets must be considered. In this case, Néel relaxation times, τ_N, differ significantly because they depend exponentially on the volume of each nanoparticle and the shape anisotropy constant. In contrast, the dependence of frictional torque on the size and shape of nanoparticles is weak. Because the S-shaped hysteresis loop of SPIONs appears in the frequency range of rotation, the secondary loss peak becomes less diffuse compared with the primary relaxation loss peak. For ferromagnetic nanoparticles, the shift of the hysteresis loss at high frequencies should still be significant even if the size of nanoparticles is not uniform, because the anisotropy field is independent of nanoparticle size. Finally, the effect of dipole–dipole interactions is considered, because the density of nanoparticles accumulated in cancer cells might be inhomogeneous if they are trapped at specific sites. In such a case, chain structures of longitudinally aligned nanoparticles have been conventionally discussed in a magnetic field, although their details are still controversial[16]. Our findings illuminate this conventional view, because, in some cases, formation of structures with a planar orientation is predicted even for individual ferromagnetic nanoparticles. In future studies, we will clarify a variety of dissipative structures, which are different from ordinary chains, for interacting nanoparticles. As discussed here, knowledge of the heat dissipation in the non-equilibrium steady states of rotatable nanoparticles is essential for the design of targeted magnetic hyperthermia treatments using large AC magnetic fields.

Methods

Model for the simulation. The magnetic response to an AC magnetic field $H_{ac}\sin(2\pi f\cdot t)$ was simulated for individual superparamagnetic/ferromagnetic magnetite nanoparticles in two extreme cases: non-rotatable nanoparticles strongly anchored to structures resembling organelles and rotatable nanoparticles in an aqueous phase resembling the cytoplasm. We considered the nanoparticles to be monodisperse prolate spheroids with equatorial diameters, $2R_M$, from 12 to 24 nm, and aspect ratios, κ, between 1.1 and 1.4. Because these dimensions are smaller than the typical exchange length of magnetite, 27 nm,[17] all of the spins are parallel to one another in each nanoparticle. In other words, we can assume that each nanoparticle has a single magnetic moment $\boldsymbol{\mu} = \boldsymbol{M}_s V$ (coherent rotation/ macro-spin approximations[14]), where V is the volume of each nanoparticle, $[(4/3)\pi\cdot\kappa R_M^3]$. The magnitude of spontaneous magnetisation $M_s = |\boldsymbol{M}_s|$ was set to the value of bulk magnetite[6], 450 kA/m, because the dependence of M_s on particle size has not been well established[18].

The magnitude of $\boldsymbol{\mu}$ is important; for example, μ of a nanoparticle with $2R_M = 24$ nm and $\boldsymbol{\kappa} = 1.4$ is $1.5\times10^5\ \mu_B$. Hence, such nanoparticles aggregate because of the large dipole–dipole interactions between $\boldsymbol{\mu}$ unless a sufficient non-magnetic surfactant layer exists. The required thickness of this layer is approximately 6 nm for nanoparticles with $2R_M = 24$ nm[19]. Therefore, in our model, we used non-magnetic layers with a thickness δR of 0.5 R_M. Consequently, we can assume that the nanoparticles are uniformly dispersed and do not aggregate. In this case, the typical distance between nanoparticles is $n^{-1/3}$, where n is the number density of nanoparticles. Because the actual mass fraction of nanoparticles accumulated in cancer cells does not exceed 1% (approximately 10 mg/mL), the magnitude of the interaction between nanoparticles with $2R_M = 24$ nm, $n\cdot\mu^2/k_B$, is estimated to be less than 1×10^2 K. Consequently, we did not consider minor effects caused by dipole–dipole interactions in our simulations.

In such an individual nanoparticle, the potential energy with respect to the direction of $\boldsymbol{\mu}$, $U(\Omega)$, is given by the following equation:

$$U(\Omega) = U_d(\Omega) + U_c(\Omega) + U_s(\Omega) - \boldsymbol{\mu}\cdot\boldsymbol{H} \tag{8}$$

where $U_d(\Omega)$, $U_c(\Omega)$, $U_s(\Omega)$ and $-\boldsymbol{\mu}\cdot\boldsymbol{H}$ are the shape, crystalline, and surface anisotropy energies, and Zeeman energy, respectively, and Ω is the solid angle of $\boldsymbol{\mu}$. For spheroidal particles, the first term, $U_d(\Omega)$, can be described as $K_d V\sin^2\phi$ and has two minima separated by the energy barrier $\Delta U = K_d V$, where K_d is the shape anisotropy constant and ϕ is the angle between the long (easy) axis and $\boldsymbol{\mu}$. The magnitudes of K_d, given by $(N_{easy}-N_{hard})\mu_0\cdot M_s^2$, are 5 and 16 kJ/m^3 for spheroidal particles with κ of 1.1 and 1.4, respectively. N_{easy} and N_{hard} are the demagnetising factors for the long and short axes, respectively. In comparison, magnetite has cubic crystalline anisotropy[20] and an anisotropy constant $K_1 = -11$ kJ/m^3. The energy landscape of cubic anisotropy ($K_1 < 0$) is gentle and ΔU is $(1/12)K_1 V \approx (1\ \mathrm{kJ/m^3})\cdot V$[19]. Additionally, the effects of surface anisotropy are generally insignificant if the particles are larger than 10 nm[18], although the rationale for this is still unknown. For these reasons, we assumed that the uniaxial shape anisotropy dominated. Consequently, equation (8) can be simplified as follows:

$$U(\varphi,\psi) \sim K_d V \sin^2\varphi - \mu H_{ac}\sin(2\pi f\cdot t)\cos\psi, \tag{9}$$

where ψ is the angle between $\boldsymbol{\mu}$ and $\boldsymbol{H}$ (see Fig. 3).

Little is known about the local environments of magnetic nanoparticles accumulated in tumour tissue. For example, nanoparticles coated with dextran are completely immobilised in tissues[21], whereas dextran nanoparticles appear to be mobile in cells[5]. For this reason, we simulated the magnetic response of the monodisperse spheroidal nanoparticles in the following two extreme cases: non-rotatable nanoparticles with randomly oriented easy axes, and rotatable nanoparticles in a Newtonian fluid with a viscosity η of 1 mPa·s.[4]

Simulation of the reversal. The detailed trajectories of $\boldsymbol{\mu}$ in a magnetic field applied at an oblique angle θ to the long easy axis of a spheroidal particle can be precisely simulated by solving the stochastic Landau–Lifshitz–Gilbert equations. However, we are only interested in the reversal of $\boldsymbol{\mu}$ once every microsecond because the frequency used for hyperthermia is limited. Therefore, we can use a well-known coarse-grained approach, or "two-level approximation"[14], that considers thermally activated reversals between the meta-stable directions, (ϕ_1, ψ_1) and (ϕ_2, ψ_2), *via* the midway saddle point at (ϕ_3, ψ_3) in $U_\theta(\phi,\psi)$. The reversal probability from (ϕ_1, ψ_1) to (ϕ_2, ψ_2), υ_{12}, is given by $f_0^{-1}\cdot\exp[(U_\theta(\phi_3, \psi_3) - U_\theta(\phi_1, \psi_1))/k_B T]$, while the backward reversal

probability υ_{21} is $f_0^{-1}\cdot\exp[(U_\theta(\phi_3, \psi_3) - U_\theta(\phi_2, \psi_2))/k_BT]$, where f_0 is the attempt frequency of 10^9 s^{-1}.

In the simulation, the time evolution of the occupation probabilities, $p_1(\theta)$, $p_2(\theta) = 1 - p_1(\theta)$, at the two stable directions of a nanoparticle tilted at θ was computed using the following relationship:

$$\partial p_1/\partial t = \upsilon_{21}p_2(\theta) - \upsilon_{12}p_1(\theta). \quad (10)$$

$p_1(\theta)$ was simply set to either zero or one when there was only one minimum in $U_\theta(\phi,\psi)$. This calculation was continued until the transient factors depending on the initial conditions disappeared. The time step Δt was typically $10^{-4}/f$ s but was shorter when $\upsilon_{12}\Delta t$ (or $\upsilon_{21}\Delta t$) became large compared with one. At each step, magnetisation was obtained as $\int(p_1(\theta)\mu\cos\psi_1 + p_2(\theta)\mu\cos\psi_2)\sin\theta d\theta$. Test simulations were performed to check the validity of this method using the same parameters as in an earlier study[14] to calculate the reversals of magnetic nanoparticles in large AC magnetic fields. As detailed in the Supplementary Information, our results agree with the reported behaviour[14].

Simulation of reversal and rotation. The rotation of spheroidal nanoparticles was simulated in synchronisation with the reversal of $\boldsymbol{\mu}$. In Newtonian fluids, the frictional torque for rotation can be expressed as $6\eta V_H\cdot(0.8 + 0.2\kappa)\cdot\boldsymbol{\omega}(t)$,[22] where $V_H = [(4/3)\pi\cdot\kappa(R_M + \delta R)^3]$ is the hydrodynamic volume and $\boldsymbol{\omega}(t)$ is the angular velocity of rotation; $d\boldsymbol{e}/dt = \boldsymbol{\omega}(t) \times \boldsymbol{e}(t)$, where $\boldsymbol{e}(t)$ is the unit vector along the long axis of the spheroid; and $\boldsymbol{\mu}(t)\cdot\boldsymbol{e}(t) = \mu\cos\phi$. Under typical conditions, where $\eta = 1$ mPa·s, $V_H \approx 10^3$ nm^3, and $\omega(t) \approx 1\times10^5$ rad/s, the inertia of the nanoparticle can be neglected (Brownian dynamics simulation). In this inertia-less limit[23], the frictional torque balances with magnetic torque $\boldsymbol{\mu}(t)\times\boldsymbol{H}(t)$ and Brownian torque $\boldsymbol{\lambda}(t)$ as follows:

$$6\eta V_H\cdot(0.8+0.2\kappa)\cdot\omega(t) = \mu(t)\times H(t) + \lambda(t) \quad (11)$$

$$<\lambda_i(t)> = 0, \quad (12)$$

$$<\lambda_i(t_1)\lambda_i(t_2)> = 2k_BT\cdot(6\eta V_H\cdot(0.8+0.2\kappa))\cdot\delta(t_1 - t_2), \quad (13)$$

where δ(t1−t2) is the Dirac delta function.

At the beginning of the simulation for the rotatable nanoparticles, an assembly of randomly oriented nanoparticles was generated, where their number ensures an optimal compromise between calculation time and precision. Then, the time evolution of the direction of $\boldsymbol{\mu}$ and the orientation of the long easy axis were computed by the following steps. (i) Using equation (9), reversible variations of the meta-stable directions $(\phi_i(t), \psi_i(t))$ caused by the latest changes in the field strength and direction of the easy axis were calculated, (ii) $\boldsymbol{\mu}(t)$ at $(\phi_1(t), \psi_1(t))$ was reversed if $x < \upsilon_{12}\Delta t$, but otherwise not. In this case, $x \in [0, 1]$ is a pseudorandom number generated by the Xorshift algorithm[24]. The backward reversal was computed in a similar manner. (iii) Substituting the reversed (or held) $\boldsymbol{\mu}(t)$ into equation (11), $\boldsymbol{\omega}(t)$ was calculated. (iv) $\boldsymbol{e}(t)$ was finally computed using the relationship $d\boldsymbol{e}/dt = \boldsymbol{\omega}(t)\times\boldsymbol{e}(t)$. This calculation was continued until transient factors depending on the initial conditions disappeared. In this simulation, Δt was typically $10^{-4}/f$ s but was shorter unless $\upsilon_{12}\Delta t$, or the changes in $\boldsymbol{e}(t)$ were sufficiently small compared to one. Magnetisation was obtained as $\Sigma(n_i\mu\cos\psi_i)$ at each step. Test simulations were performed to check the validity of this method. There have been no prior theoretical studies on systems where both reversal and rotation occur simultaneously in a large AC magnetic field. Consequently, comparisons with prior studies were performed under two extreme conditions. In the first case, high viscosities were assumed. Because reversal dominates rotation under these conditions, the results were compared with those reported by Carrey *et al.*[14]. In the second case, a high anisotropic field was assumed. Because rotation dominates reversal in this situation, the results were compared with the numerical simulations of Yoshida *et al.*, where nonlinear Brownian rotational relaxation of magnetic fluids with a large excitation field was studied using the Fokker–Planck equation[13]. The results obtained from our simulation of reversal and rotation were consistent with those of earlier studies (Supplementary Figs. S1–S4). Therefore, we can now take a first step toward understanding the roles that rotation of a nanoparticle and reversal of its magnetic moment play together in large AC magnetic fields.

1. Pankhurst, Q. A., Thanh, N. K. T., Jones, S. K. & Dobson, J. Progress in applications of magnetic nanoparticles in biomedicine. *J. Phys.* **D42** 224001 (2009).
2. Sugahara, K. N., *et al.* Coadministration of a tumor-penetrating peptide enhances the efficacy of cancer drugs. *Science* **328**, 1031–1035 (2010).
3. DeNardo, S. J., *et al.* Development of Tumor Targeting Bioprobes (^{111}In-Chimeric L6 Monoclonal Antibody Nanoparticles) for alternating magnetic field cancer therapy. *Clin. Cancer Res.* **11**, 7087s–7092s (2005).
4. Kuimova, M. K., *et al.* Imaging intracellular viscosity of a single cell during photoinduced cell death. *Nature Chem.* **1**, 69−73 (2009).
5. Kalwarczyk, T., *et al.* Comparative analysis of viscosity of complex liquids and cytoplasm of mammalian cells at the nanoscale. *Nano Lett.* **11**, 2157–2163 (2011).
6. Rosensweig, R. E. Heating magnetic fluid with alternating magnetic field. *J. Magn. Magn. Mater.* **252**, 370–374 (2002).
7. Chung, S. -H., *et al.* Biological sensing with magnetic nanoparticles using Brownian relaxation. *J. Appl. Phys.* **97**, 10R101 (2005).
8. Kalele, S., Narain, R. & Krishnan, K. M. Probing temperature-sensitive behaviour of pNIPAAm-coated iron oxide nanoparticles using frequency-dependent magnetic measurements. *J. Magn. Magn. Mater.* **321**, 1377–1380 (2009).
9. Hergt, R., Dutz, S. & Röder, M. Effects of size distribution on hysteresis losses of magnetic nanoparticles for hyperthermia. *J. Phys.: Condens. Matter* **20,** 385214 (2008).
10. Kim, D.-H., Nikles, D. E., Johnson, D. T. & Brazel, C. S. Heat generation of aqueously dispersed $CoFe_2O_4$ nanoparticles as heating agents for magnetically activated drug delivery and hyperthermia. *J. Magn. Magn. Mater.* **320**, 2390–2396 (2008).
11. Müller, R., *et al.* Hysteresis losses in iron oxide nanoparticles prepared by glass crystallization or wet chemical precipitation. *J. Magn. Magn. Mater.* **310**, 2399–2404 (2007).
12. Brown, Jr. W. F. Thermal Fluctuations of a Single-Domain Particle. *Phys. Rev.* **130**, 1677–1686 (1963).
13. Yoshida, T., & Enpuku, K. Simulation and Quantitative Clarification of AC Susceptibility of Magnetic Fluid in Nonlinear Brownian Relaxation Region, *Jpn. J. Appl. Phys.* **48**, 127002 (2009).
14. Carrey, J., Mehdaoui, B., & Respaud, M. Simple models for dynamic hysteresis loop calculations of magnetic single-domain nanoparticles: Application to magnetic hyperthermia optimization, *J. Appl. Phys.* **109**, 083921 (2011).
15. Fortin, J. P., *et al.* Size-sorted anionic iron oxide nanomagnets as colloidal mediators for magnetic hyperthermia, *J. Am. Chem. Soc.* **129,** 2628−2635 (2007).
16. Mamiya, H., Nakatani, I., & Furubayashi, T. Phase transitions of iron nitride magnetic fluids, *Phys. Rev. Lett.* **84**, 6106−6109 (2000).
17. Li, Z., Kawashita, M., Araki, N., Mitsumori, M., Hiraoka, M. & Doi, M. Magnetite nanoparticles with high heating efficiencies for application in the hyperthermia of cancer. *Mater. Sci. Engineering,* **C 30**, 990–996 (2010).
18. Demortière, P., *et al.* Size-dependent properties of magnetic iron oxide nanocrystals. *Nanoscale* **3**, 225−232 (2011).
19. Mamiya, H., & Jeyadevan, B. Optimal design of nanomagnets for targeted hyperthermia *J. Magn. Magn. Mater.* **323**, 1417–1422 (2011).
20. Hellwege, K. H. *Magnetic and Other Properties of Oxides and Related Compounds*, (Landolt-Börnstein New Series **III 4b**, Springer-Verlag, New York, 1970).
21. Dutz, S., Kettering, M., Hilger, I., Müller, R., & Zeisberger, M. Magnetic multicore nanoparticles for hyperthermia—influence of particle immobilization in tumour tissue on magnetic properties, *Nanotechnology* **22**, 265102 (2011)
22. Ilg, P. & Kröger, M. Magnetisation dynamics, rheology and an effective description of ferromagnetic units in dilute suspension. *Phys. Rev.* **E66**, 021501 (2002).
23. Coffey, W. T. On the contribution of multiplicative noise terms to the Langevin equation for rotational relaxation. *J. Chem. Phys.* **99**, 3014–3020 (1993).
24. Marsaglia, G. Xorshift RNGs, *J. Stat. Soft.* **8**, 1–6 (2003).

Acknowledgements

This study was partly supported by a Grant-in-Aid for Scientific Research (21241023 and 21681014).

Author contributions

H. M. performed the simulation. H. M. and B. J. wrote the manuscript.

Additional information

Supplementary information accompanies this paper at http://www.nature.com/scientificreports

Competing financial interests: The authors declare that they have no competing financial interests.

How to cite this article: Mamiya, H. & Jeyadevan, B. Hyperthermic effects of dissipative structures of magnetic nanoparticles in large alternating magnetic fields. *Sci. Rep.* **1**, 157; DOI:10.1038/srep00157 (2011).